JAERI-M
84-065

EVALUATION OF ADVANCED TWO-PHASE FLOW INSTRUMENTATION IN SCTF CORE-I

March 1984

Takamichi IWAMURA, Makoto SOBAJIMA,
Masahiro OSAKABE, Akira OHNUKI, Yutaka ABE,
Yukio SUDO and Hiromichi ADACHI

日本原子力研究所
Japan Atomic Energy Research Institute

JAERI-M レポートは，日本原子力研究所が不定期に公刊している研究報告書です。
入手の問合わせは，日本原子力研究所技術情報部情報資料課（〒319－11 茨城県那珂郡東海村）あて，お申しこしください。なお，このほかに財団法人原子力弘済会資料センター（〒319-11 茨城県那珂郡東海村日本原子力研究所内）で複写による実費頒布をおこなっております。

JAERI-M reports are issued irregularly.
Inquiries about availability of the reports should be addressed to Information Section, Division of Technical Information, Japan Atomic Energy Research Institute, Tokai-mura, Naka-gun, Ibaraki-ken 319-11, Japan.

編集兼発行　日本原子力研究所
印　　刷　山田軽印刷所

JAERI-M 84-065

EVALUATION OF ADVANCED TWO-PHASE FLOW INSTRUMENTATION IN SCTF CORE-I

Takamichi IWAMURA, Makoto SOBAJIMA, Masahiro OSAKABE,
Akira OHNUKI, Yutaka ABE, Yukio SUDO and Hiromichi ADACHI

Department of Nuclear Safety Research,
Tokai Research Establishment, JAERI

(Received February 16, 1984)

In the Slab Core Test Facility (SCTF) Core-I, advanced two-phase flow instruments have been provided by the USNRC to measure the thermohydraulic behavior in the primary system including pressure vessel during the end of blowdown, refill and reflood phases of a postulated loss-of-coolant accident in a pressurized water reactor.

The advanced instruments are turbine meters, drag disks, γ-densitometers, spool pieces, liquid level detectors (LLD), fluid distribution grids (FDG), impedance probes (flag, prong and string probes), film probes, and video optical probes.

This report presents evaluated results of the data from these instruments. Some instruments are quantitatively evaluated by comparing with the data from the conventional instruments or the other advanced instruments. Main conclusions are as follows:

(1) The spool pieces and the γ-densitometers work well and provide satisfactory results;

(2) Some of the turbine meters, the impedance probes and the film probes give partially reasonable results, but still more improvements are required;

(3) Most of the LLDs, the FDGs, the impedance probes, and the film probes do not work well due to a hard cable corrosion, and

(4) The video optical probes give clear image of the flow pattern.

Keywords : Two-phase Flow Instrumentation, Reflood, Turbine Meter, Drag Disk, Gamma Densitometer, Spool Piece, Liquid Level Detector, Fluid Distribution Detector, Impedance Probe, Film Probe, Video Optical Probe, SCTF, LOCA, PWR, Blowdown

---

The work was performed under contract with the Atomic Energy Bureau of Science and Technology Agency of Japan.

平板炉心試験装置第1次炉心における新型二相流計測器の評価

日本原子力研究所東海研究所安全工学部
岩村　公道・傍島　　真・刑部　真弘
大貫　　晃・阿部　　豊・数土　幸夫
安達　公道

（1984年2月16日受理）

平板炉心試験装置（SCTF）第1次炉心には，加圧水型原子炉で想定される冷却材喪失事故時のブローダウン終期，再浸水および再冠水期間中における原子炉圧力容器内の熱水力学的挙動を測定するため，米国原子炉規制委員会から新型二相流計測器が提供されている。

これらの新型計測器とは，タービンメータ，ドラッグディスク，ガンマ線密度計，スプールピース，液位計（LLD），液体分布グリッド（FDG），インピーダンスプローブ（フラグ，プロングおよびストリングプローブ），フィルムプローブおよびビデオオプティカルプローブである。

本報は，これら計測器から得られたデータの評価結果について報告する。計測器のいくつかについては，従来型計測器又は他の新型計測器からのデータと比較して評価した。

主要な結論は以下の通りである。(1) スプールピースとガンマ線密度計は正常に作動し，満足すべき結果が得られた。(2) タービンメータ，インピーダンスプローブおよびフィルムプローブの一部からは，部分的に正しいとみなせる結果が得られた。(3) LLD，FDG，インピーダンスプローブおよびフィルムプローブの大部分は，ハードケーブル故障のため正常に作動しなかった。(4) ビデオオプティカルプローブからは，流動パターンの良好な画像が得られた。

本報告書は，電源開発促進対策特別会計法に基づき，科学技術庁からの受託によって行った研究の成果である。

Contents

目　　次

List of Tables

List of Figures

1. Introduction

The multi-dimensional thermo-hydrodynamic behavior during the reflood phase of a postulated loss of coolant accident (LOCA) in a pressurized water reactor (PWR) is being investigated by using the Slab Core Test Facility (SCTF) which has a full height, full radial width and single bundle depth electrically heated core. The SCTF program is a part of the large scale reflood test program under contract with the Atomic Bureau of Science and Technology Agency of Japan along with the Cylindrical Core Test Facility (CCTF) program.

The Large Scale Reflood Test Program is one of the research activities based on the agreement (2D/3D agreement) among Japan Atomic Energy Research Institute (JAERI), the Federal Ministry for Research and Technology (BMFT) of the Federal Republic of Germany (FRG) and the United States Nuclear Regulatory Commission (USNRC). According to the agreement, the USNRC has provided various kinds of advanced two-phase flow instruments in addition to the conventional instruments provided by JAERI.

The advanced instruments provided by the USNRC are the turbine flow meters, drag disks, γ-densitometers, spool pieces, liquid level detectors (LLDs) and fluid distribution grids (FDGs) manufactured by the Idaho National Engineering Laboratory (INEL); the flag probes, prong probes, string probes, film probes and reference conductivity probe manufactured by the Oak Ridge National Laboratory (ORNL); and the video optical probes manufactured by the Los Alamos National Laboratory (LANL).

In this report, the status of the USNRC-provided instrumentation is presented. At present, some USNRC-provided instruments work well and the outputs can be compared quantitatively with the data obtained from the JAERI-provided instruments. Outputs from some other USNRC-provided instruments seem qualitatively good but quantitatively unrealistic or cannot be verified because of no suitable data to be compared. Most of the outputs from the LLDs, the FDGs, the flag probes, the prong probes, and the film probes are not available due to the stress corrosion of hard cables.

2. Description of USNRC-Provided Advanced Two-Phase Flow Instrumentation

2.1 Brief Description of Slab Core Test Facility (SCTF)

The schematic diagram of SCTF and the comparison of dimensions between the SCTF and a 1,100 MWe PWR are shown in Fig. 2-1 and Table 2-1, respectively.

The primary coolant loops consist of a hot leg equivalent to the four actual hot legs, a steam/water separator corresponding to the four actual steam generators, an intact cold leg equivalent to the three actual intact cold legs, a broken cold leg on the pressure vessel side, and a broken cold leg on the steam/water separator side.

The flow area scaling ratio is 1/21 to a 1,100 MWe PWR, whereas the height of each component simulates the actual PWR. The emergency core cooling system (ECCS) consists of an accumulator (Acc) and a low pressure coolant injection (LPCI) system. Fig. 2-2 shows the vertical cross section of the pressure vessel. The pressure vessel includes a simulated core, an upper plenum with internals, a lower plenum, a core baffle and a downcomer.

The simulated core consists of 8 bundles arranged in a row with full radial width. Each bundle consists of 234 heater rods and 22 non-heated rods arranged in 16×16 array. The outer diameter and the heated length of the heater rod are 10.7 mm and 3660 mm, respectively. The dimensions of rod bundle such as the rod pitch, the spacers, the end box the plate etc., are based on those for a 15×15 fuel rod bundle of a PWR.

The core and the upper plenum are enveloped by honeycomb thermal insulators to minimize the wall effects.

More detailed information on the SCTF is available in reference (1).

2.2 Measurement Items

The USNRC-provided instrumentation has been developed and manufactured at three laboratories in the USA. INEL has supplied 4 sets of LLDs (4×20 measurement points), 2 sets of FDGs (8×8 and 2×3×7 measurement points), 16 turbine meters, 3 drag disks, 19 γ-densitometers

and 3 spool pieces. ORNL has supplied 26 film probes, 8 flag probes, 8 prong probes, 3 string probes and one reference probe. LANL has supplied 2 video optical probes.

The measurement items and quantities of the USNRC-provided instruments are given in Table 2-2 for each location.

The measurement locations, quantities, channels and computed physical values are listed in Tables 2-3 and 2-4 for the INEL-manufactured instruments and the ORNL-manufactured instruments, respectively.

2.3 Measurement Locations

Schematic arrangement of the USNRC-provided instruments in the pressure vessel and in the primary coolant loops are shown in Figs. 2-3 and 2-4, respectively. Figure 2-5 shows the relative elevations of the in-core and downcomer instruments provided by JAERI and USNRC. The horizontal arrangement of heater rods and non-heated rods with instrumentation is shown in Fig. 2-6. The relative elevations of the USNRC-provided instruments in the upper plenum and in the vicinity of the upper core support plate (UCSP) are shown in Fig. 2-7.

The detailed measurement locations for each instrument are described in Appendix A. The measurement locations for the JAERI-provided instruments are described in the design report[1].

2.4 Description of Instruments

2.4.1 Hot Leg Spool Piece

The hot leg spool piece consists of four single-beam γ densitometers, four drag disks, four fluid temperature thermocouples, one metal temperature thermocouple and one absolute pressure transducer. The fluid densities, void fractions, fluid velocities and mass flow rates are obtained by the use of data reduction software as described in Appendix B-2.

The configuration of the hot leg spool piece is shown in Fig. 2-8 and the cross sections are shown in Figs. 2-9 and 2-10. Since the cross section of the hot leg is long circular, the hot leg spool piece has four sets of instruments corresponding to four subsections. Fig. 2-10 shows the boundary of each region. Region 1 comprises the upper 31 % of the pipe cross-sectional area, Region 2 comprises the next lower

27 %, Region 3 comprises the next lower 26 %, and Region 4 comprises the bottom 16 %.

Each region has a drag transducer, a thermocouple and a single-beam γ densitometer detectors. Two detectors are received γ rays from a common source and two γ sources are installed as shown in Fig. 2-9. An absolute pressure transducer and a metal temperature thermocouple are common to all regions.

2.4.2 Cold Leg Spool Piece

The cold leg spool piece consists of a three-beam γ densitometer, a full-flow turbine flowmeter, three drag transducers attached on a drag screen, a fluid and a metal temperature thermocouples, an absolute pressure transducer and a differential pressure transducer across the drag screen. The densities, velocities and mass flow rates for water, steam and two-phase mixture are separately obtained as well as the void fraction by the use of data reduction software as described in Appendix B-3.

A schematic of the cold leg spool piece is shown in Fig. 2-11. The cross section of the three-beam γ densitometer is shown in Fig. 2-12. The densitometer has three γ sources and one detector. The sources are Gd^{153}, Cd^{109} and Am^{241} from the top to bottom. The beams can be identified by the different energy for each source.

The drag screen is a perforated screen which is supported by three rakes and each rake is connected to drag transducer. The configuration of the drag screen is shown in Fig. 2-13.

The installed configurations of the thermocouples, pressure taps and turbine meter are shown in Figs. 2-12 and 2-13.

2.4.3 Vent Pipe Spool Piece

The vent pipe spool piece has not been used in the SCTF Core-I tests. It will be used in the vent valve simulation test planned in the SCTF Core-III.

The vent pipe spool piece consists of a full-flow turbine flowmeter, three drag screen transducers, a fluid and a metal temperature thermocouples, an absolute pressure transducer and a differential pressure transducer across the drag screen. The fluid velocity and mass flow rate are obtained by the use of the data

reduction software.

Instrumentation for the vent pipe spool piece assembly is the same as the cold leg spool piece assembly except that the vent pipe spool piece has a gas turbine instead of liquid and has no densitometer.

The configuration of the vent pipe spool piece is the same as the cold leg spool piece except the densitometer as shown in Figs. 2-11, 2-12 and 2-13

2.4.4 Pressure Vessel γ-Densitometer

Nineteen single-beam γ-densitometers are used in the SCTF pressure vessel to measure two-phase fluid density. Ten γ-densitometers are installed between the core bundles at three elevations, five are below the end box tie plate and four are at the upper plenum.

The γ densitometer system consists of a γ source, detector and electronics.

There are two types of densitometer: ten type A densitometers in the core and nine type B densitometers in the upper plenum and below the end box tie plate. The schematic drawings of the type A and B densitometers are shown in Figs. 2-14 and 2-15, respectively.

The γ source assembly uses A_m^{241} with an effective photopeak of 60 KeV for the both types. The activity is 1.8 Ci for the type A source and 0.75 Ci for the type B cource assembly. The detector assembly consists of a sodium-iodide (thallium-activated) crystal, photomultiplier tube, and preamplifier.

The output of the single-beam γ-denstitometer is a pulse count over a selected unit of time for each measurement location, with each count total being an inverse function of local average fluid density at that location. The selected frequency of measurement is 3.3 Hz for all densitometers.

2.4.5 Liquid Level Detector (LLD) and Fluid Distribution Grid (FDG)

A total of 4 conductivity-type Liquid Level Detector (LLD) assemblies are installed in the bundles 2, 4, 6 and 8 of the simulated core. Each LLD assembly has 20 electrodes to measure liquid level and detect local voids or water pockets along the length of the assembly.

Two sets of Fluid Distribution Grid (FDG) systems are installed in the upper plenum and downcomer to measure liquid level and detect

gross local voids and water distribution within a two or three-dimensional volume. The upper plenum FDG consists of 8 × 8 two-dimensional grids and the downcomer FDG of 2 × 3 × 7 three dimensional grids.

The locations of each electrode of the LLDs and FDGs are shown in Fig. A-4.

The configurations of LLD assembly and each sensor are shown in Figs. 2-16 and 2-17, respectively. The LLD assembly is located inside a sleeve as shown in Fig. 2-18.

The multi-rod assemblies of the upper plenum and downcomer FDGs are shown in Figs. 2-19 and 2-20, respectively. The configuration of the FDG sensor is shown in Fig. 2-21.

Based on the impedance changes between the electrodes of each discrete measurement point for the LLDs and FDGs, the fluid state is determined whether it is wet or dry. The wet/dry data for the LLDs and FDGs are simultaneously displayed on a cathode ray tube (CRT) screen. The display format is shown in Fig. 2-22.

2.4.6 Turbine Flowmeter

A total of sixteen turbine flowmeters are installed in the pressure vessel to measure local fluid velocity. Four of them are located in the lower plenum, eight just above the UCSP holes and four in the upper plenum.

The turbine meters in the lower plenum are used to measure the water velocities at the inlet of core. However, the applicable measurement range is too high in comparison to the required measurement range. The turbine meters just above the UCSP holes and in the upper plenum are used to measure steam velocities. Because the steam contains many droplets during a test, the measured velosity may not represent the real steam velocity. As shown in Fig. A-3, two turbines out of four in the upper plenum are horizontally oriented to measure the horizontal steam velocity from the upper plenum to the hot leg.

The configurations of the turbine meters in the upper and lower plenum and of those just above the UCSP holes are shown in Figs. 2-23 and 2-24, respectively.

2.4.7 Downcomer Drag Disk

Three drag disks are installed in the downcomer to measure the

velocity of a single-phase liquid flow.

In order to obtain the two-phase mass flow rate, the measured momentum fluxes from the drag disks are combined with the densities from adjacent string probes.

Fig. 2-25 shows the downcomer drag disk assembly. The drag disk assembly has a drag disk and a thermocouple. The thermocouple is used to determine the saturated water density which is necessary to calculate fluid velocity.

2.4.8 Impedance Probe

Three types of impedance probes; flag, prong and string probes, are installed in the pressure vessel to measure the void fraction and velocity of a steam-water mixture. Eight flag probes are located in the core, eight prong probes in the upper plenum and three string probes in the downcomer.

The configurations of the flag, prong and string probes are shown in Figs. 2-26, 2-27 and 2-28, respectively. The pair electrodes on the flag or prong probes are insulated from the assemblies by a cermet. When there is air or steam between the probe electrodes, the electrical impedance is very high; when there is water, the impedance is much lower. In this way, the probes detect the nature of the two-phase mixture in their vicinity.

The two wires of the string probe are routed in such a way as to cover a large area. The wires are insulated from the frame of the probe by cermet insulators. The impedance measured by the string probe is the total of all the impedance between the two wires over their entire path. Therefore, the string probe makes an average measurement of the two-phase mixture over a large area. This is in contrast with the flag and prong probes which measure impedance in a much smaller region.

The in-core flag probe cnsists of two flag-type electrode pairs which are placed a short distance vertically apart. Therefore, the velocity of void or droplet can be obtained by a cross correlation analysis of the two impedance signals.

The prong and string probes which consist of one set of electrode cannot measure the velocity of void or droplet.

2.4.9 Film Probe

Three types of film probes are installed in the pressure vessel to measure the film thickness and film velocity. Those are fourteen wall film probes located on the core and upper plenum side walls and six upper plenum film probes located on the surface of the upper plenum structure and six in-core film probes located on the surface of non-heated rods in core. The configurations of the wall, upper plenum and in-core film probes are shown in Figs. 2-29, 2-30 and 2-31.

The wall film probe consists of three dual electrode film thickness sensors, an electrolysis potential (E.P.) sensor and a thermocouple. One of the three film thickness sensors is used as the liquid conductivity sensor by measuring the impedance magnitude and phase.

The upper plenum film probe consists of two dual electrode film thickness sensors, an E.P. sensor and a thermocouple. Conductivity sensor is not involved.

The in-core film probe consists of two single electrode film thickness sensors, an E.P. sensor and a thermocouple.

2.4.10 Reference Conductivity Probe

The reference conductivity probe is installed at the bottom of pressure vessel to measure the liquid conductivity. The measured conductivity is used for the data reduction of the film and impedance probes. Only the wall film probe module contains a conductivity probe so that it is not necessary to use the measured conductivity with the reference probe.

The configuration of the reference conductivity probe is the same as that of the dual-electrode film thickness sensors those are installed on the side walls and upper plenum structure.

The configuration is shown in Fig. 2-32.

2.4.11 Video Optical Probe

Two video optical probes are used for viewing the space in the upper plenum near the hot-leg nozzle and below the end box tie plate.

The video optical probe consists of a miniature TV camera and lens system surrounded by a water cooling jacket that is necessary because of the temperature limitation of lens material.

Fig. 2-33 shows a schematic of the probe pressure boundary, the

internal components of the probe and the arrangement of windows. Around the water jacket is a gold-plate annulus, filled with xenon gas, to minimize heat conduction and radiation to the video components. This feature also minimizes the disturbance to the facility by the probe. An electrical heater coil prevents fogging of the camera view window. There are six D.C. lights and two pulsed strobe lights for illumination.

2.5 Data Reduction Procedure

The flow diagram of the data reduction procedure is shown in Fig. 2-34 for both the JAERI-provided and the USNRC-provided instrumentation.

The data from the ORNL instruments (201 ch) and the INEL instruments (74 ch) except LLDs and FDGs are recorded on the analog tape of a PCM recorder and transferred to six digital magnetic tapes, five for ORNL data (MT01 ∿ 5) and one for INEL data (MTI1). These raw data are converted to physical values by using a data processing software which includes the ORNL and INEL supplied subroutines.

The computed algorithms for the INEL instruments and for the ORNL instruments are described in Appendix B and Appendix C, respectively.

The raw data from the LLDs and FDGs are recorded on an analog tape of the FM recorder and impedance plots for every sensor are obtained by using a mini-computer (LSI-11). Threshold values between wet and dry are determined from these plots and the raw data are converted to the wet and dry data. The results are displayed on a CRT color display.

Table 2-1 Comparison between SCTF and a 1,100 MWe PWR

Item	SCTF	PWR	Ratio (SCTF/PWR)
Quantity of Bundle	8	193	1/24.1
Number of Heater Rod	1872	39372	1/21.0
Number of Rods	2048	43425	1/21.2
Effective Length of Heater Rod (mm)	3660	3660	1/1
Rod Pitch (mm)	14.30	14.30	1/1
Diameter of Heater Rod (mm)	10.70	10.72	1/1
Diameter of Unheated Rod (mm)	13.80	13.87	1/1
Flow Area of Core (m^2)	0.259	4.76	1/17.7
Effective Core Flow Area Based on the Measured Level-Volume Relationship(m^2)	0.35	4.76	1/13.6
Fluid Volume of Core Enveloped by Honeycomb Insulators*	0.92	17.95	1/19.5
Fluid Volume of Lower Plenum (m^3)	1.305	29.62	1/22.7
Fluid Volume of Upper Head (m^3)	0.86	19.8	1/23.0
Baffle Region Flow Area (m^2)	0.10	1.76	1/17.6
Upper Plenum Fluid Volume (m^3)	1.16	23.8	1/20.5
Downcomer Flow Area (m^2)	0.121	2.47	1/20.4
UCSP Thickness (m)	76	76	1/1
Steam Generator Inlet Plenum Simulator Volume (m^3)	0.931	4.25×4	1/18.3
Height of Steam Generator Inlet Plenum Simulator (m)	1.595	1.595	1/1
Flow Area at the Top Plate of Steam Generator Inlet Plenum Simulator (m^2)	0.19	4.0	1/21.2
Major Axis Length of Hot Leg Cross Section	737	736.6	1/1
Flow Area of Hot Leg (4 Loops)	0.0826	1.704	1/20.6
Flow Area of Intact Loop (3 Loops)	0.0696	1.149	1/16.5
Flow Area of Broken Cold Leg (m^2)	0.0179	0.383	1/21.4
* Fluid Volume of Core Including Gaps between Core Barrel and Pressure Vessel Wall	1.74		

Table 2-2 Measurement items of USNRC-provided instruments

LOCATION	MEASUREMENT	INSTRUMENT	QUANTITY
1. CORE			
non-heated rods	liquid level	LLD	20×4 = 80
non-heated rods	film thickness and velocity	film probe	6
non-heated rods	void fraction and droplet velocity	flag probe	8
side walls	film thickness and velocity	film probe	8
sub-channel	fluid density	γ-densitometer	10
end box	fluid density	γ-densitometer	5
end box	flow pattern	video optical probe	1
2. UPPER PLENUM			
full height	liquid level	FDG	8×8 = 64
structure surface	film thickness and velocity	film probe	6
side walls	film thickness and velocity	film probe	6
inter structure	void fraction	prong probe	8
above UCSP hole	velocity	turbine	8
inter structure	velocity	turbine	4
inter structure	fluid density	γ-densitometer	4
hot leg inlet	flow pattern	video optical probe	1
3. LOWER PLENUM			
core inlet	velocity	turbine	4
bottom	reference conductivity	reference probe	1
4.DOWNCOMER			
full height	liquid level	FDG	2×3×7 = 42
two levels	velocity	drag disk	3
two levels	void fraction	string probe	3

Table 2 – 2 (continue)

LOCATION	MEASUREMENT	INSTRUMENT	QUANTITY
5. HOT LEG	mass flow rate	spool piece	1
	fluid density	drag disk	4
	void fraction	γ-densitometer	4
		thermocouple	5
		absolute pressure	1
6. BROKEN COLD LEG-PV SIDE	mass flow rate	spool piece	1
	fluid density	3beam γ-densitometer	1
	void fraction	turbine	1
		drag transducer	3
		thermocouple	2
		differential pressure	1
		absolute pressure	1
7. VENT LINE	mass flow rate	spool piece	1
	void fraction	turbine	1
		drag transducer	3
		thermocouple	2
		differential pressure	1
		absolute pressure	1

Table 2-3 INEL-manufactured instruments

Instrument Name	Location	Quantity	Channels/Instrument	Total Channels	Computed physical value
Turbine meter	UCSP hole	8	1	8	Fluid velocity
	Upper plenum	4	1	4	
	Lower plenum	4	1	4	
Drag disk	Downcomer	3	drag disk 1 temperature 1	6	Fluid velocity
Gamma-densitometer	Core	10	1	10	Fluid density
	Below end box	5	1	5	
	Upper plenum	4	1	4	
Spool piece	Hot leg	1	densitometer 4 drag disk 4 temperature 5 pressure 1	14	Fluid density Void fraction Fluid velocity Mass flow rate } × 4 region
	Cold leg	1	densitometer 3 drag transducer 3 temperature 2 pressure 1 diff. pressure 1 turbine 1	11	Void fraction Velocity Density Mass flow rate } of { Water / Steam / Fluid
	Vent pipe	1	drag transducer 3 temperature 2 pressure 1 diff. pressure 1 turbine 1	8	Steam and water densities Fluid velocity Mass flow rate
Total		41 instruments		74 channels	

Table 2-4 ORNL-manufactured instruments

Sensor Type	Probe Name	Location	Quantity	ch/probe	Total channels	Computed physical values
Type 1	Reference conductivity probe	Lower plenum	1	4	4	Liquid conductivity
2	Dual impedance probe (core flag probe)	Non heated rods in core	8(2/4 rods)	4	32	Void fraction velocity
3	Single impedance probe (Upper plenum prong probe)	Upper plenum	8(2/4 rods)	3	24	Void fraction
4	Dual electrode film probe (with E.P. and conductivity sensor)	Core side wall Upper plenum side wall	8 6 } 14	6	84	Film thickness Film velocity
5	Dual electrode film probe (with E.P. probe only)	Upper plenum structures	6	4	24	Film thickness Film velocity
6	Single electrode film probe (with E.P. probe only)	Non-heated Rods in core	6	4	24	Film thickness Film velocity
7	Singel impedance probe (string probe)	Downcomer	3	3	9	Void fraction
Total			46 instruments		201 channels	

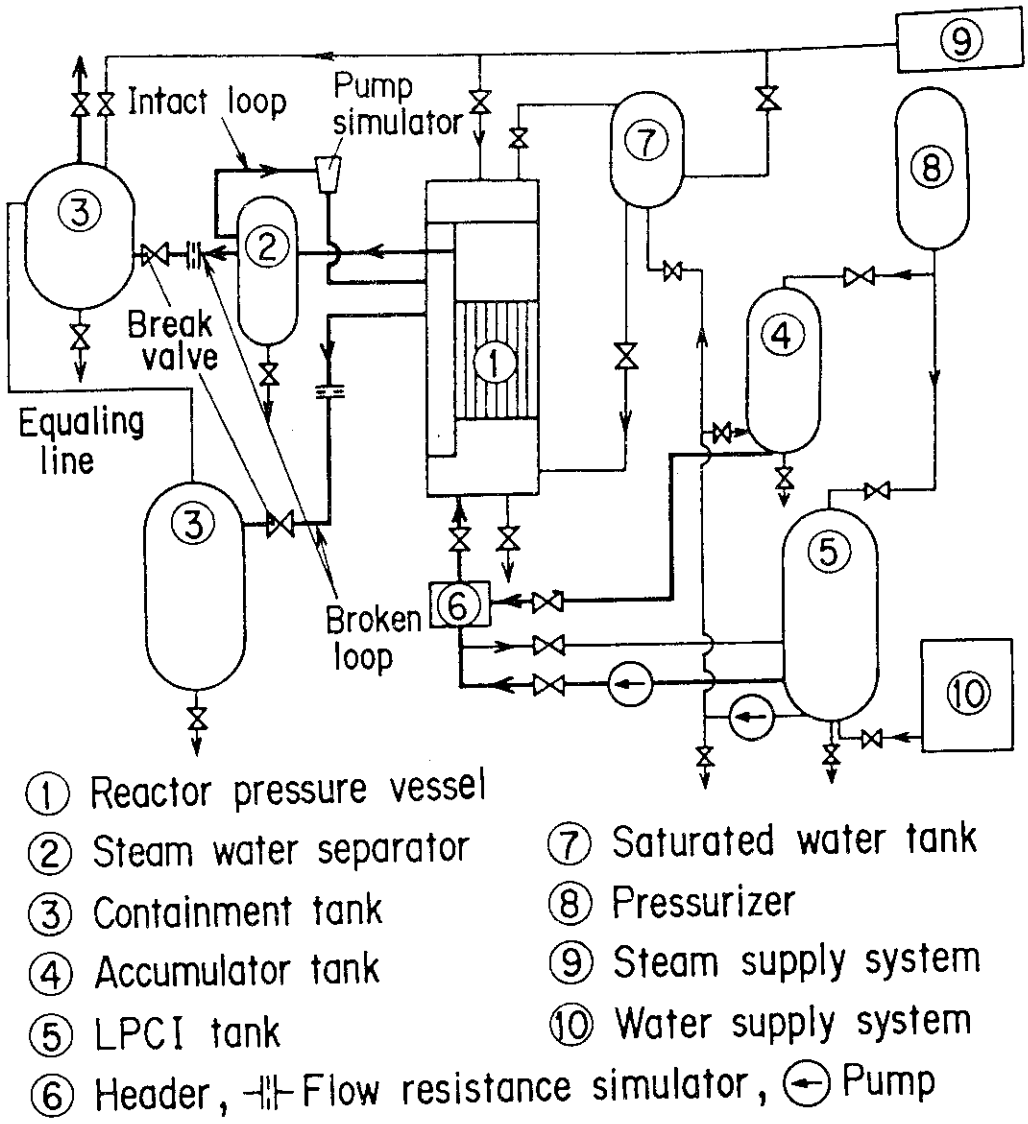

Fig. 2-1 Schematic diagram of Slab Core Test Facility

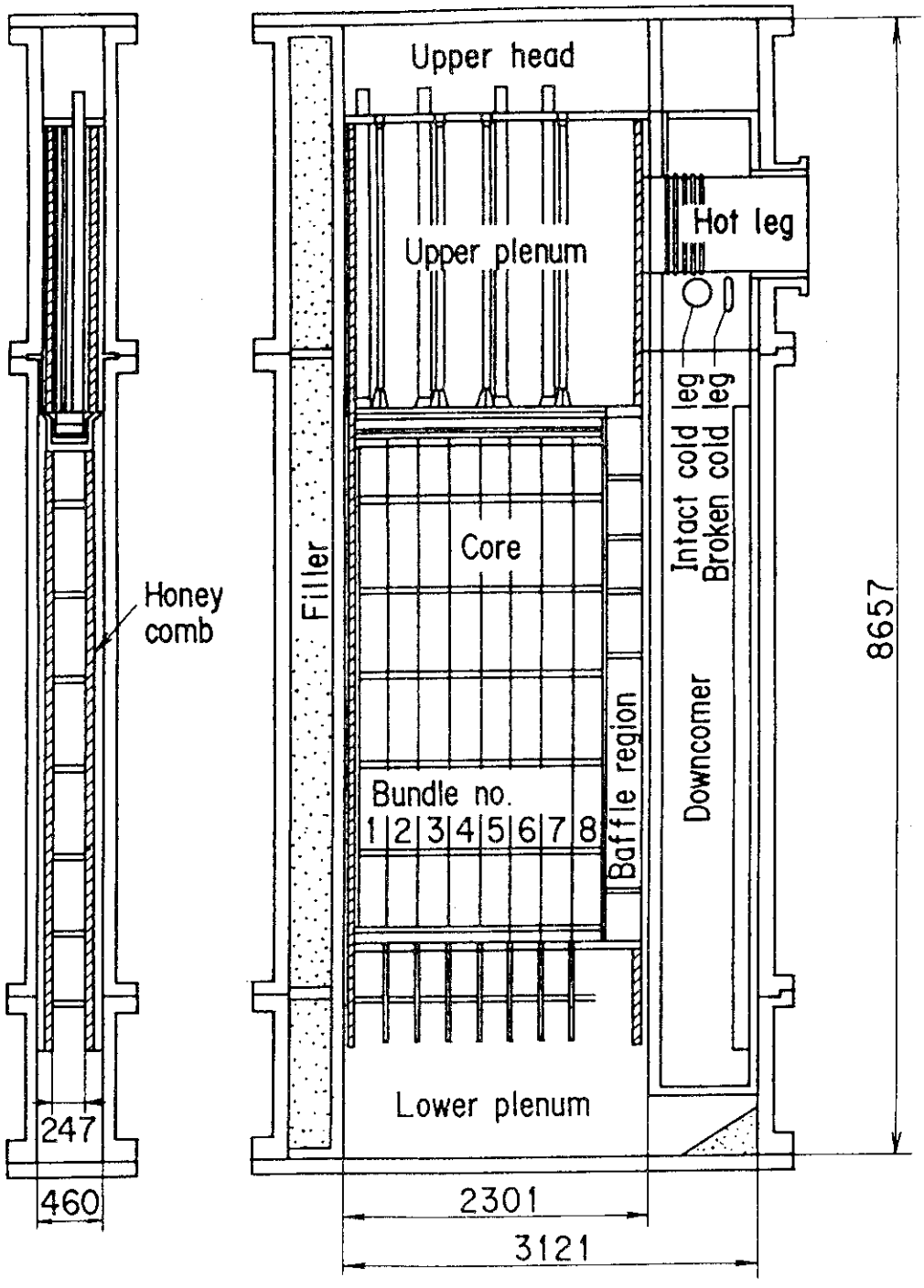

Fig. 2-2 Pressure vessel of Slab Core Test Facility

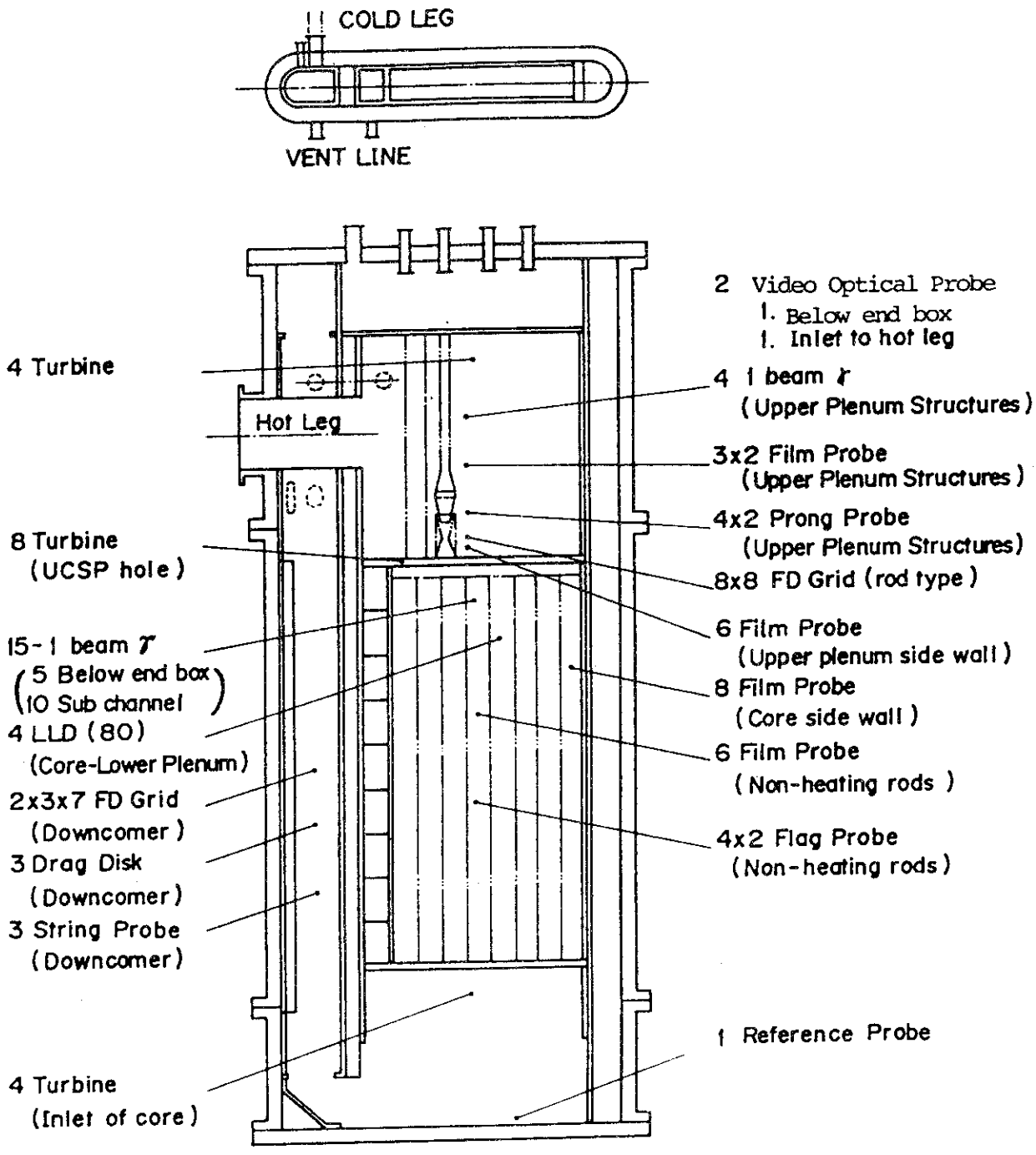

Fig. 2-3 Schematic Arrangement of USNRC-Provided Instruments

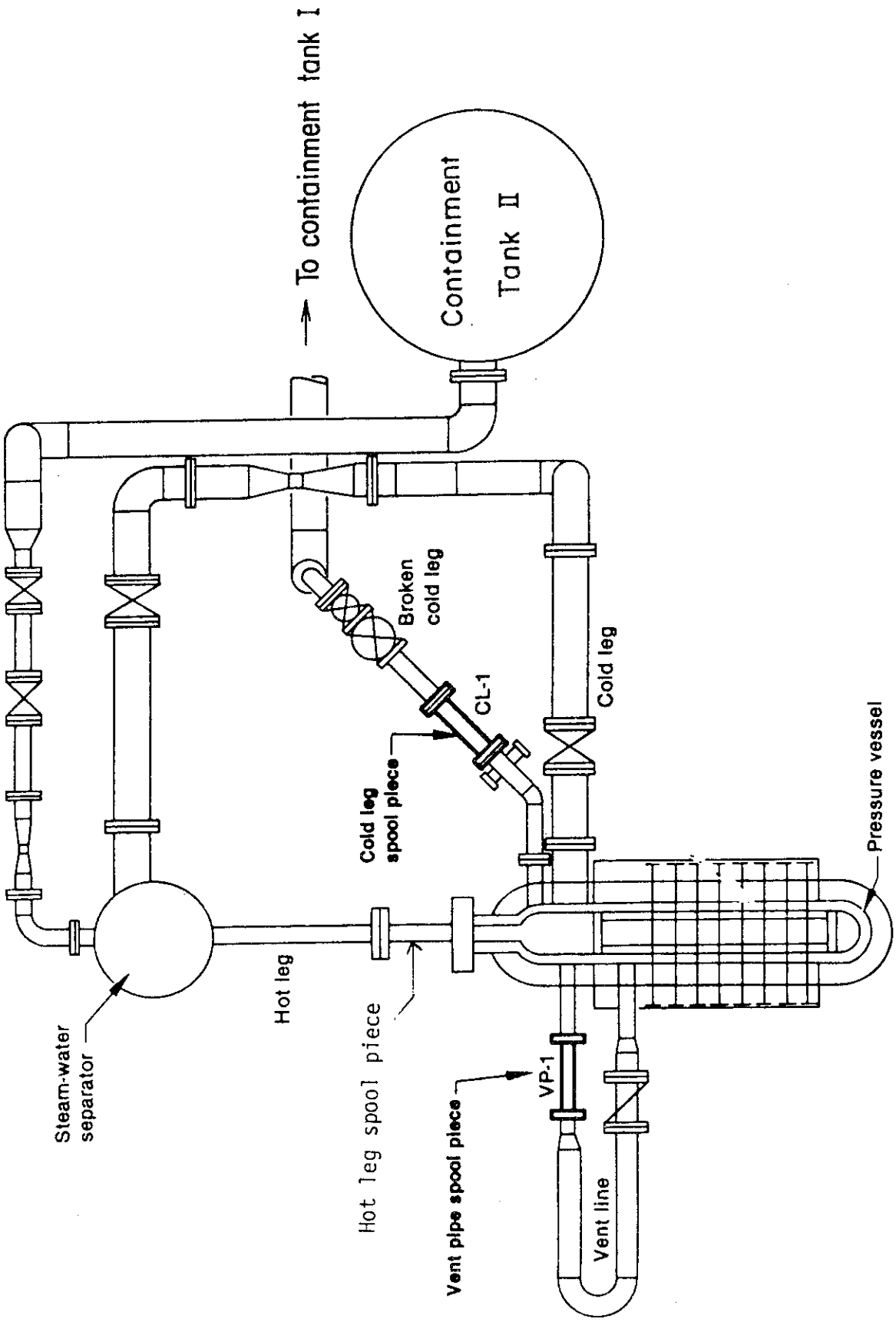

Fig. 2-4 Spool Piece Locations

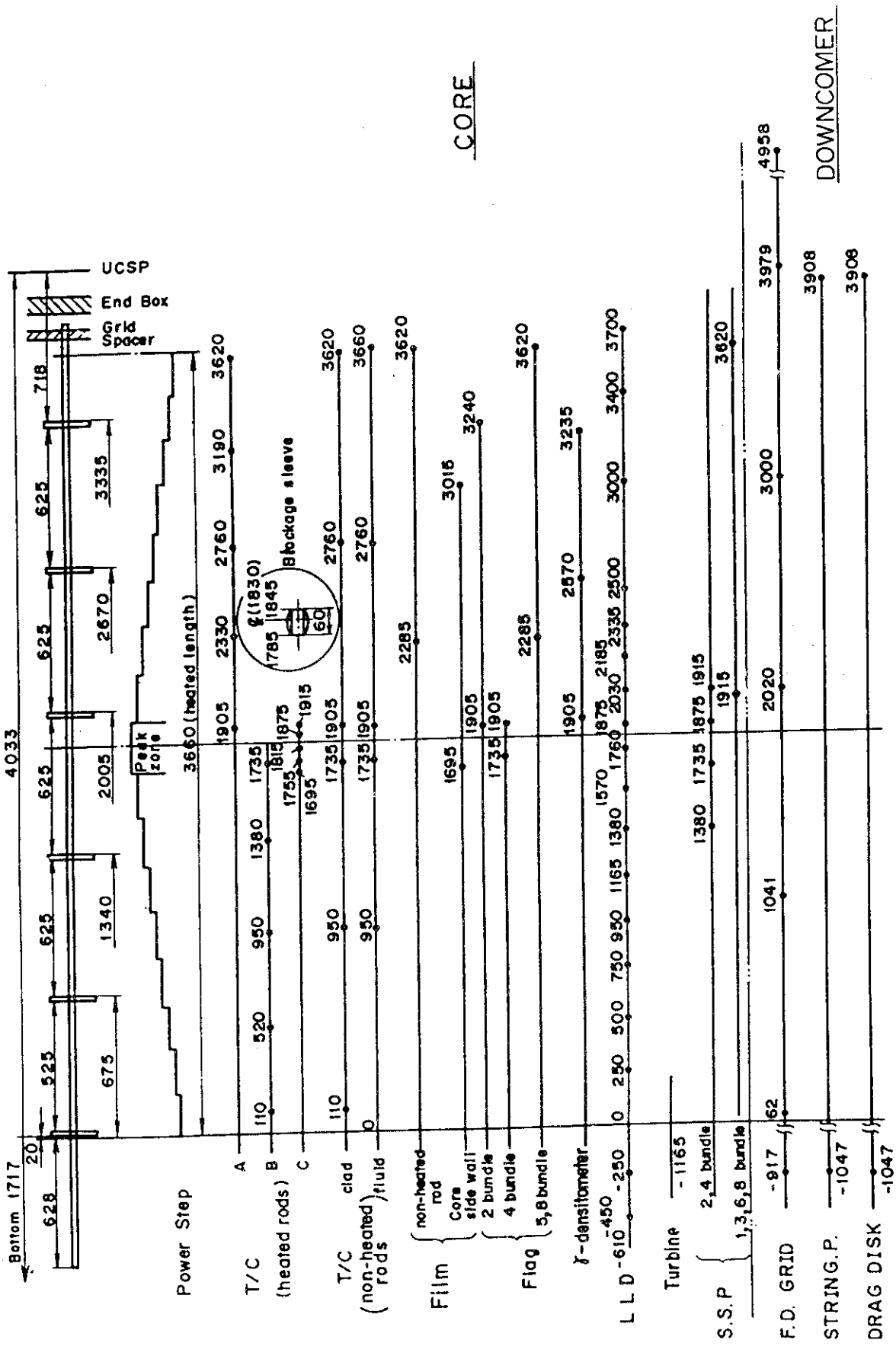

Fig. 2-5 Relative Elevations of In-Core and Downcomer Instruments

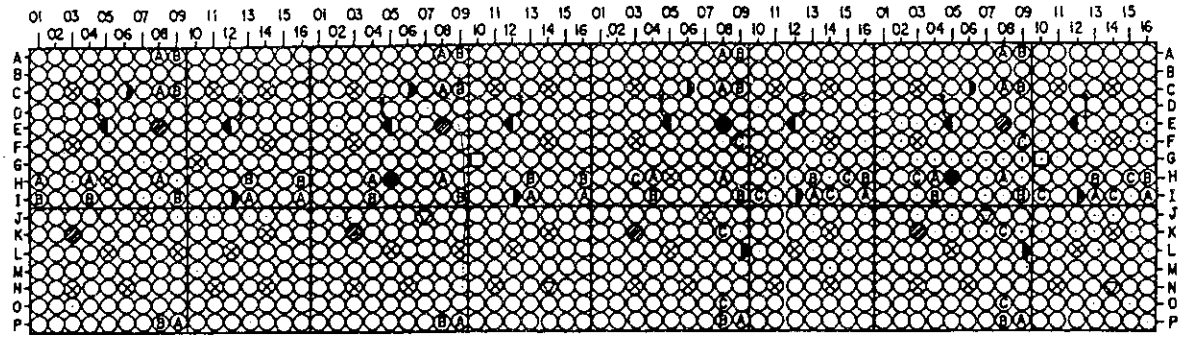

Bundle 1 Bundle 2 Bundle 3 Bundle 4

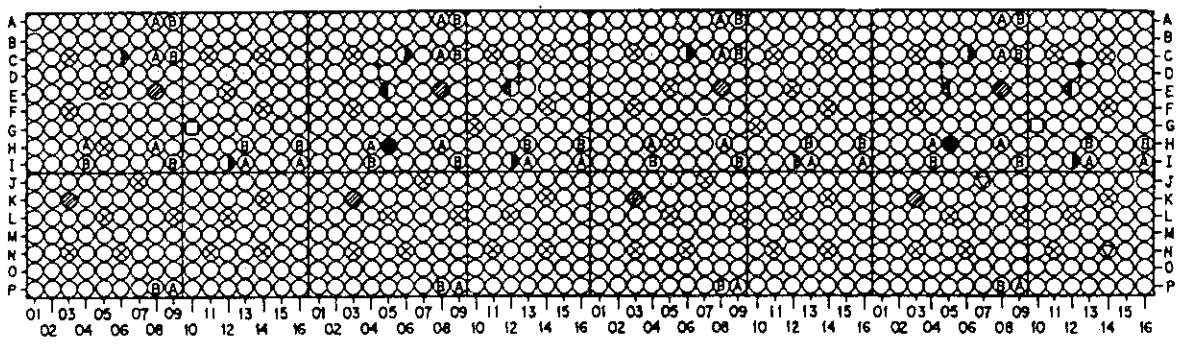

Bundle 5 Bundle 6 Bundle 7 Bundle 8

Bundle No.		1	2	3	4	5	6	7	8	Total	Symbol
Heater Rod Surface Temp.		16	14	21	21	14	14	14	14	128	Ⓐ Ⓑ Ⓒ
Heater Rod with No Instrument		218	220	213	213	220	220	220	220	1744	○
Non Heated Rod With Instrument	Surface Temp.	2	2	3	3	2	2	2	2	18	◐
	Fluid Temp.	2	2	2	2	2	2	2	2	16	⊘
	Steam Temp.	2	2	2	2	—	2	—	2	12	◐
	Film Probe	—	2	—	2	—	—	—	2	6	⊘
	Flag Probe	—	1	—	1	1	—	—	1	4	○
	L L D	—	1	—	1	—	1	—	1	4	●
Tie Rod		16	12	15	11	17	15	18	12	116	⊗
Total		256	256	256	256	256	256	256	256	2048	

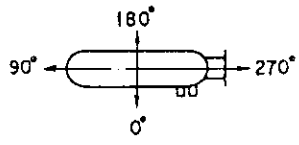

Fig. 2-6 Horizontal Arrangement of Instrumented Rods

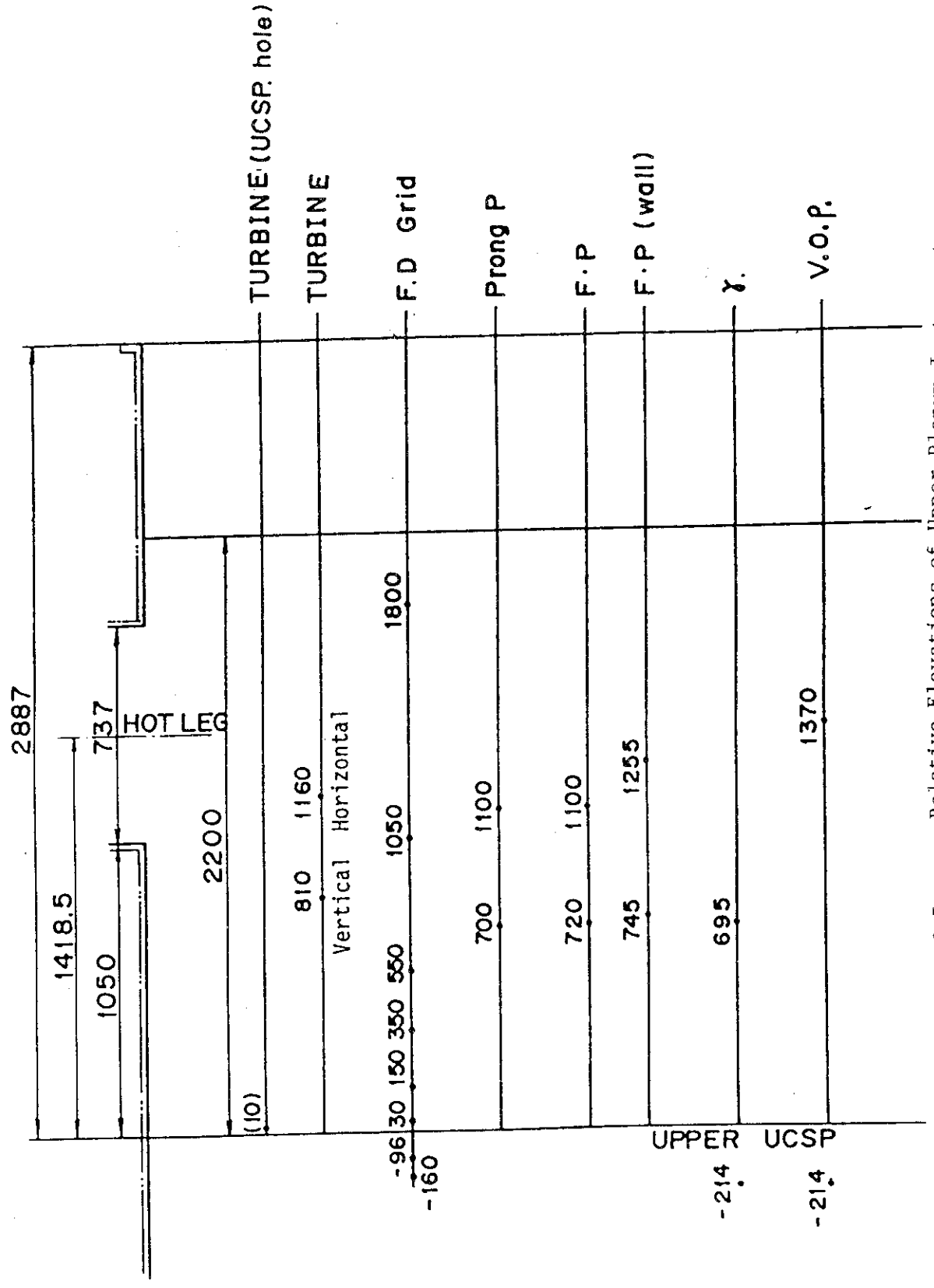

Fig. 2-7 Relative Elevations of Upper Plenum Instruments

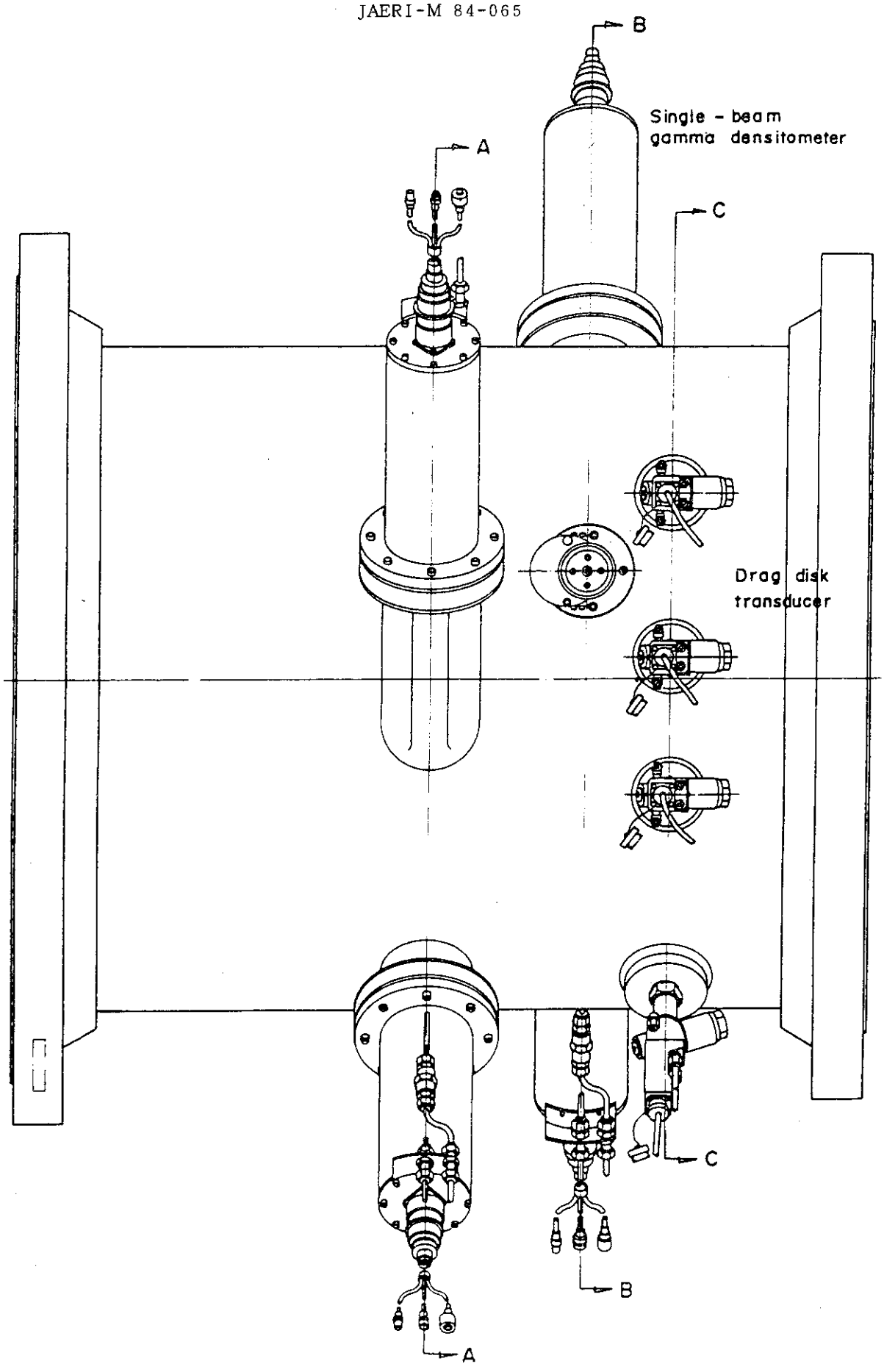

Fig.2- 8 Hot leg spool piece configuration

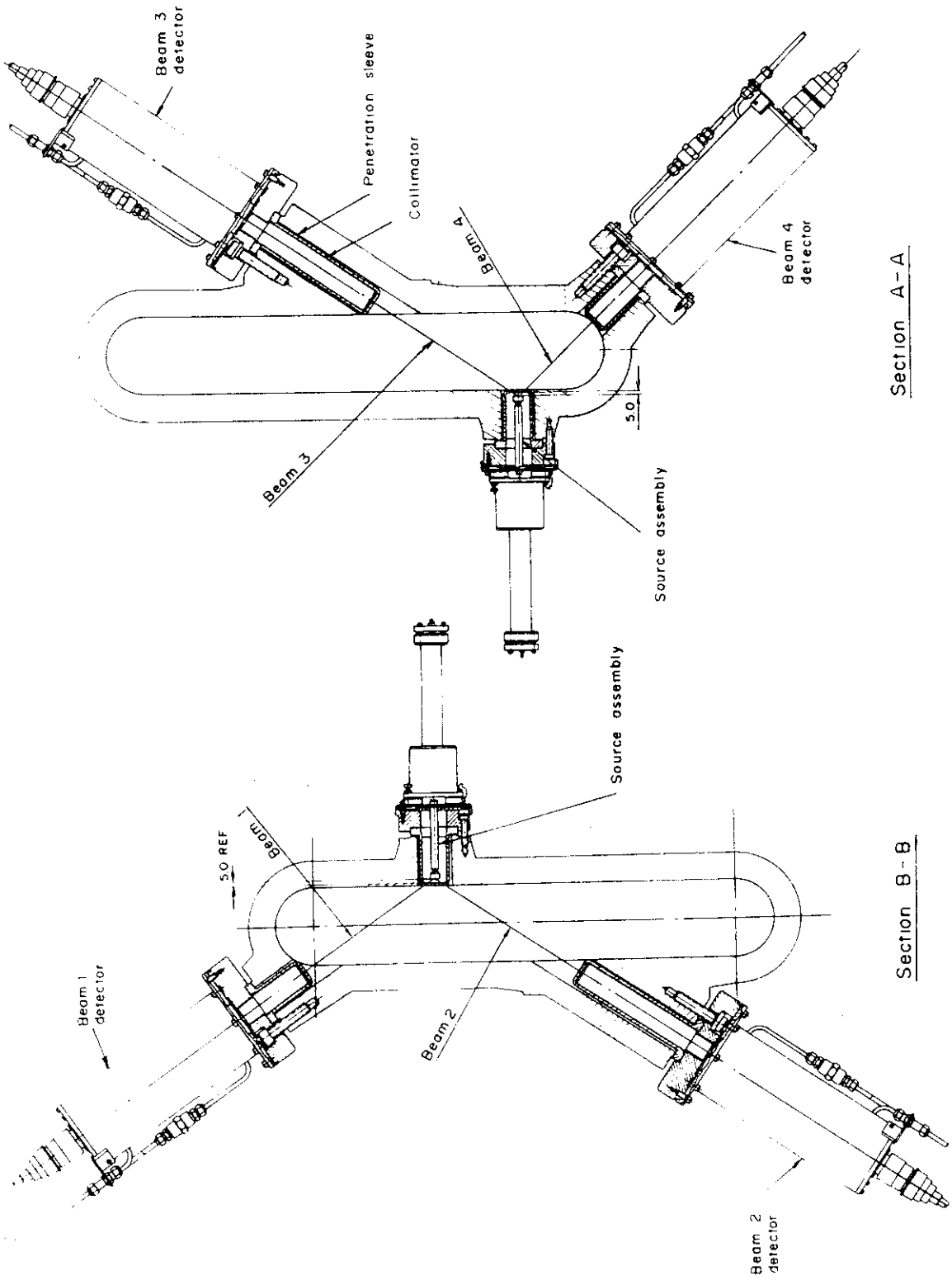

Fig.2- 9 Cross section of hot leg spool piece (single-beam gamma densitometer)

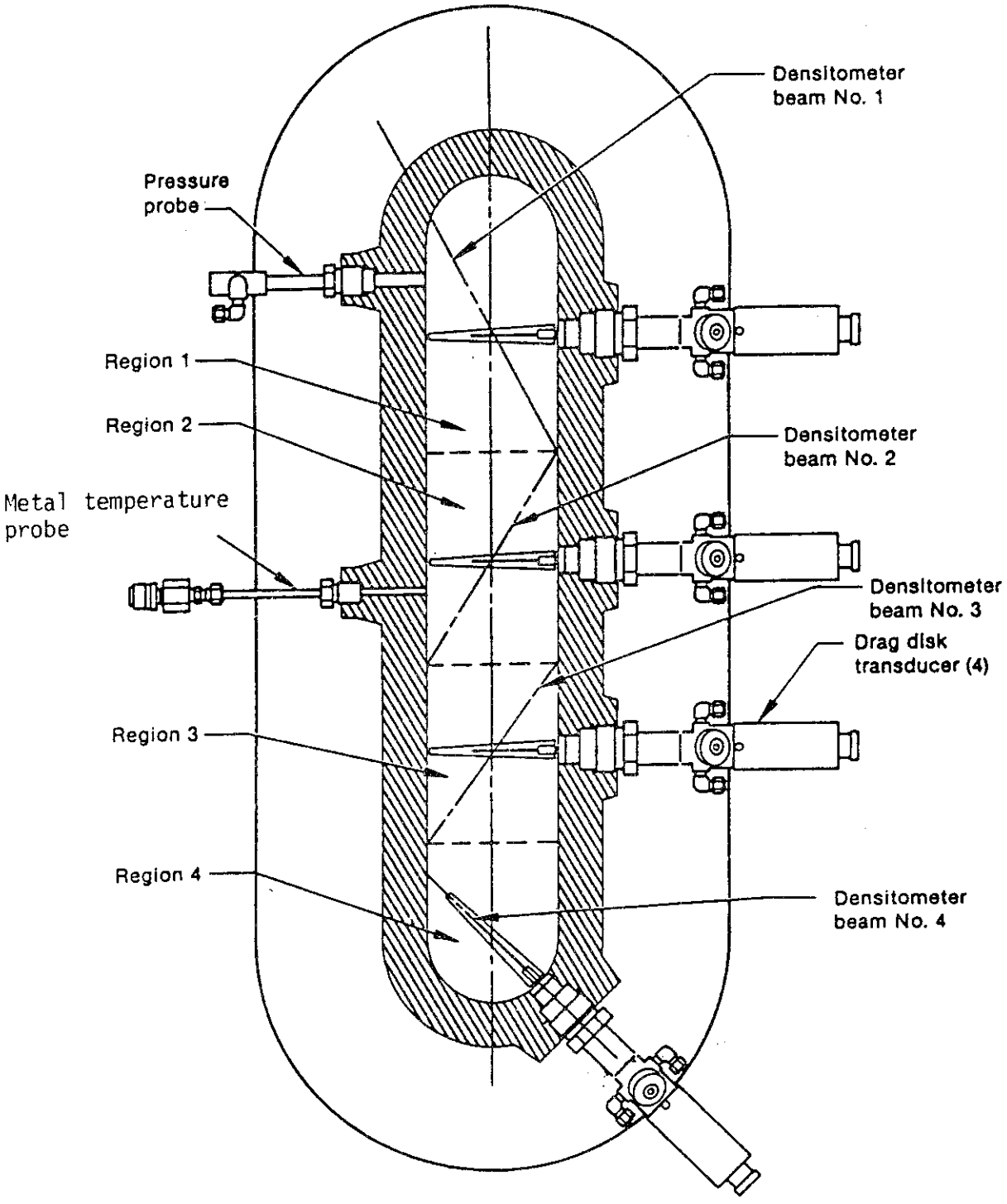

Fig.2-10 Cross section of hot leg spool piece (drag disk, thermocouple, pressure tap)

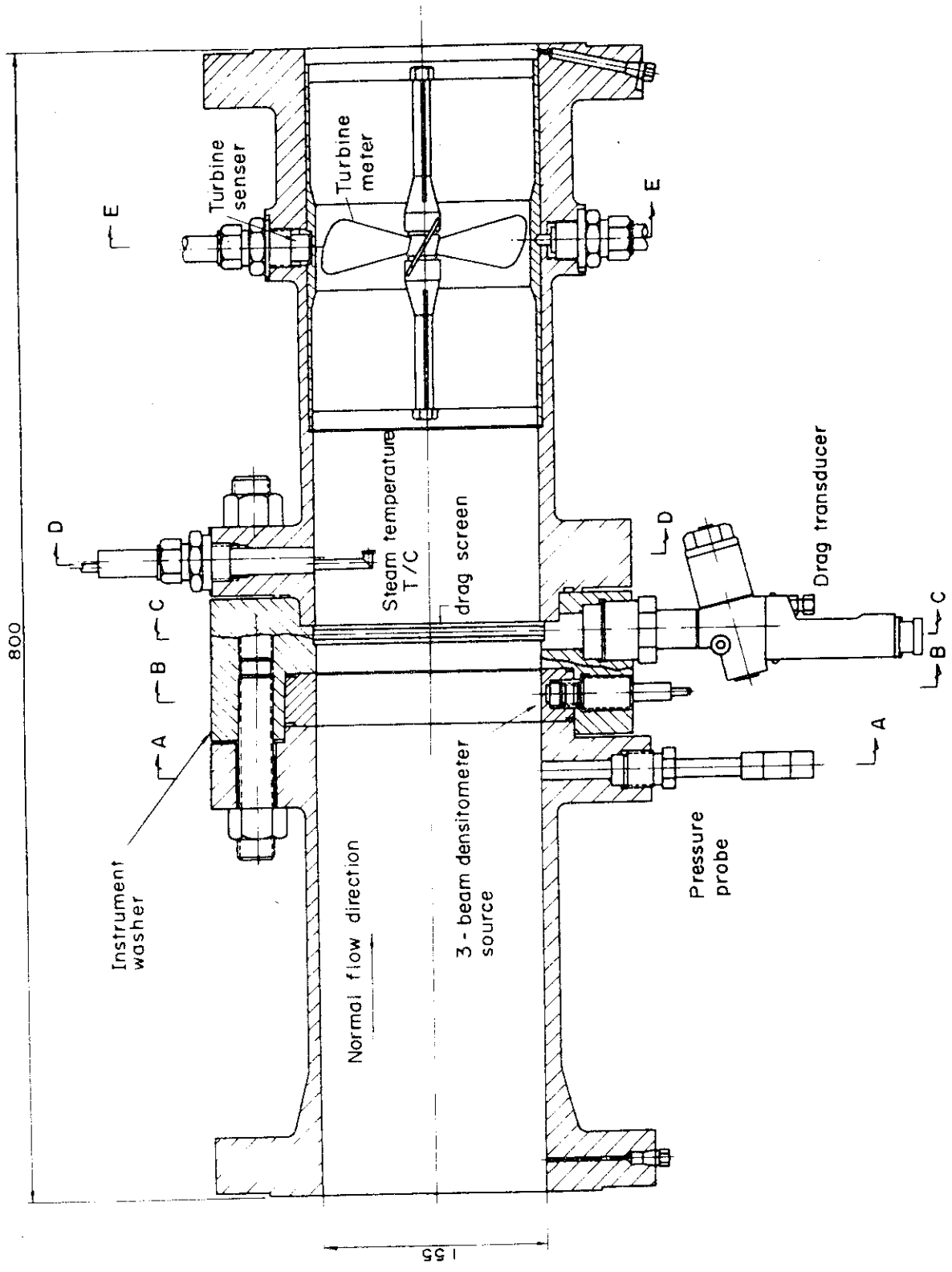

Fig. 2-11 Cold leg spool piece assembly

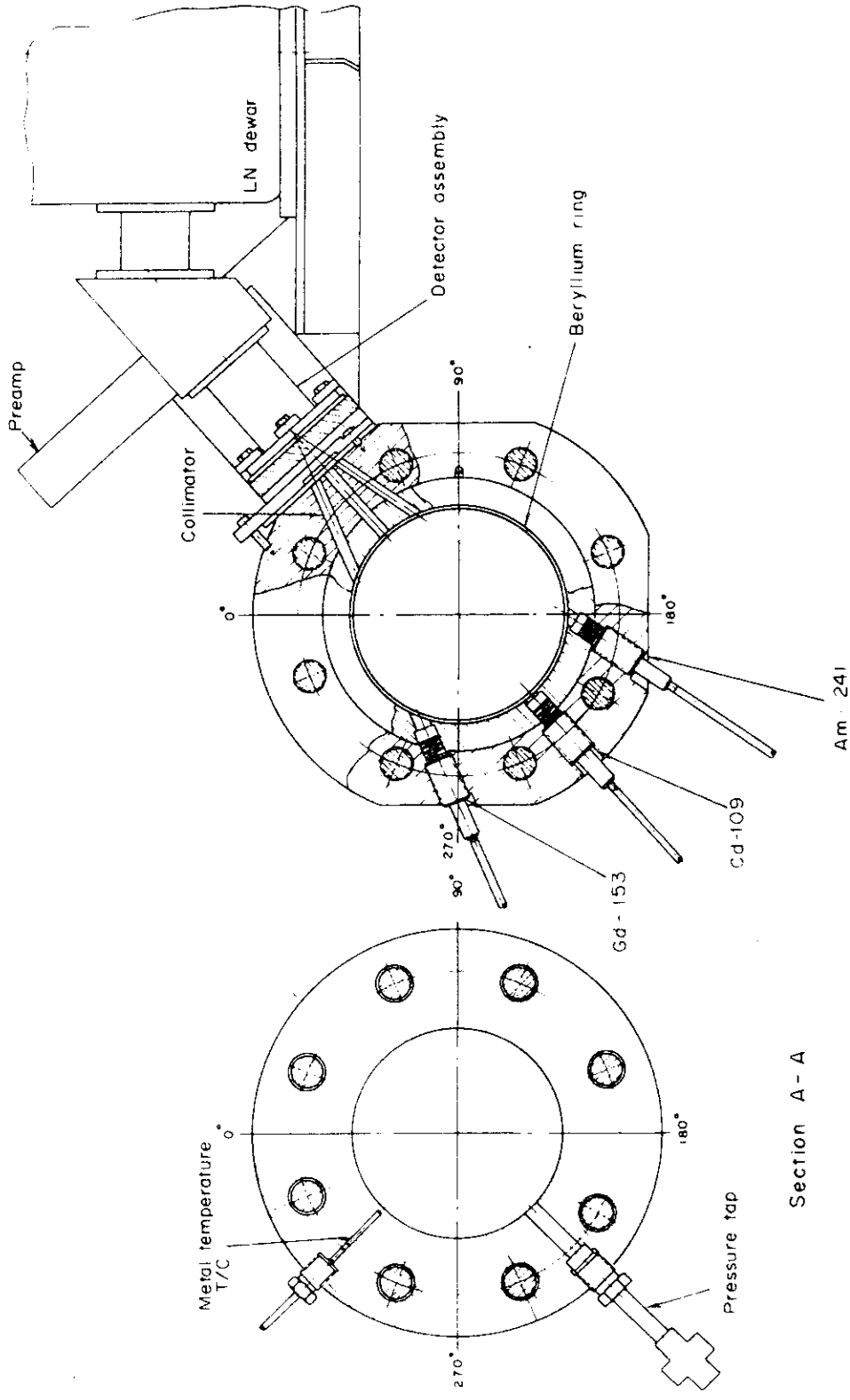

Fig. 2-12 Cross section of cold leg spool piece (3-beam γ-densitometer, metal temperature thermocouple and pressure transducer)

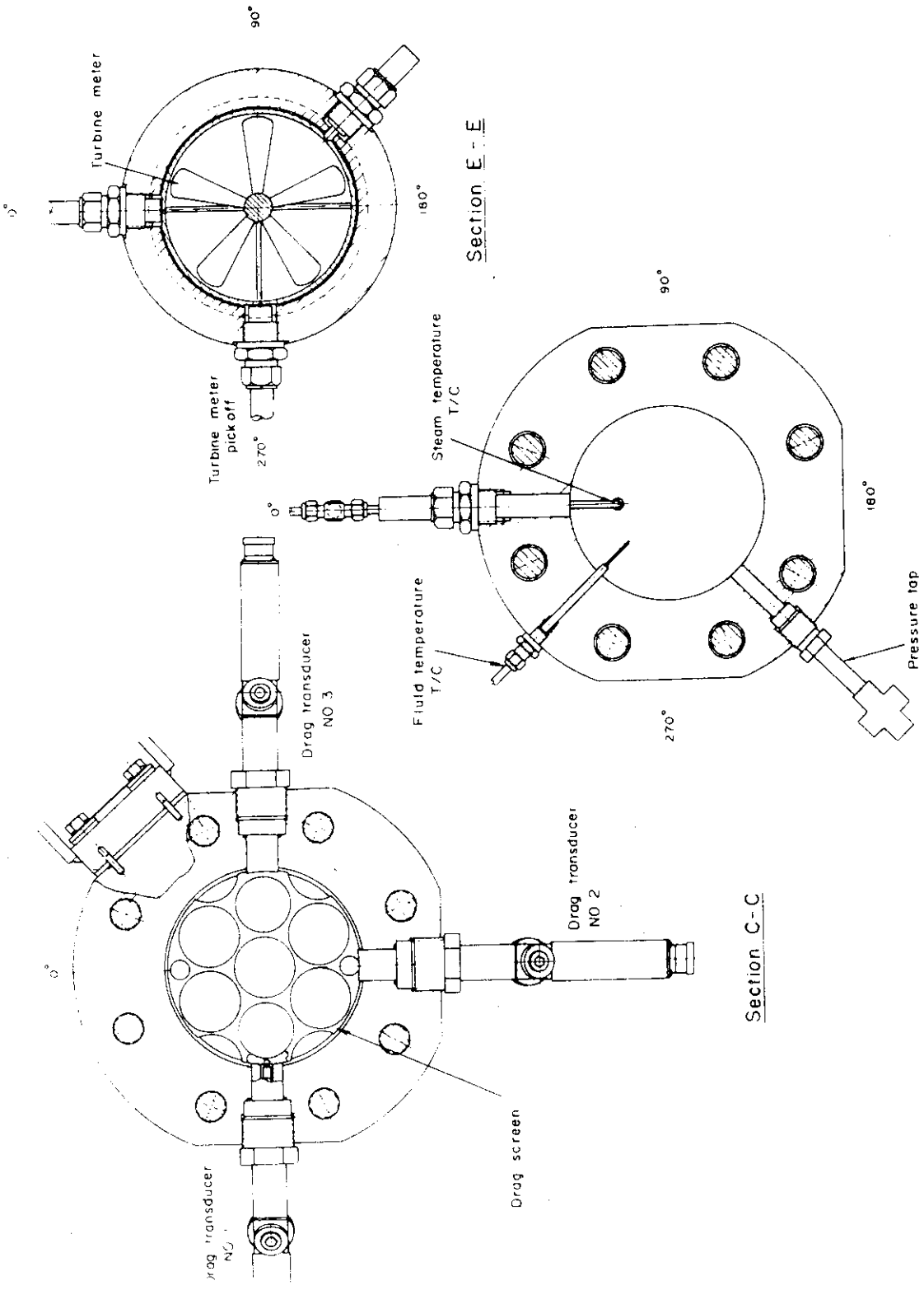

Fig. 2-13 Cross section of cold leg spool piece (drag screen, fluid and steam temperature thermocouples, pressure tap and turbine meter)

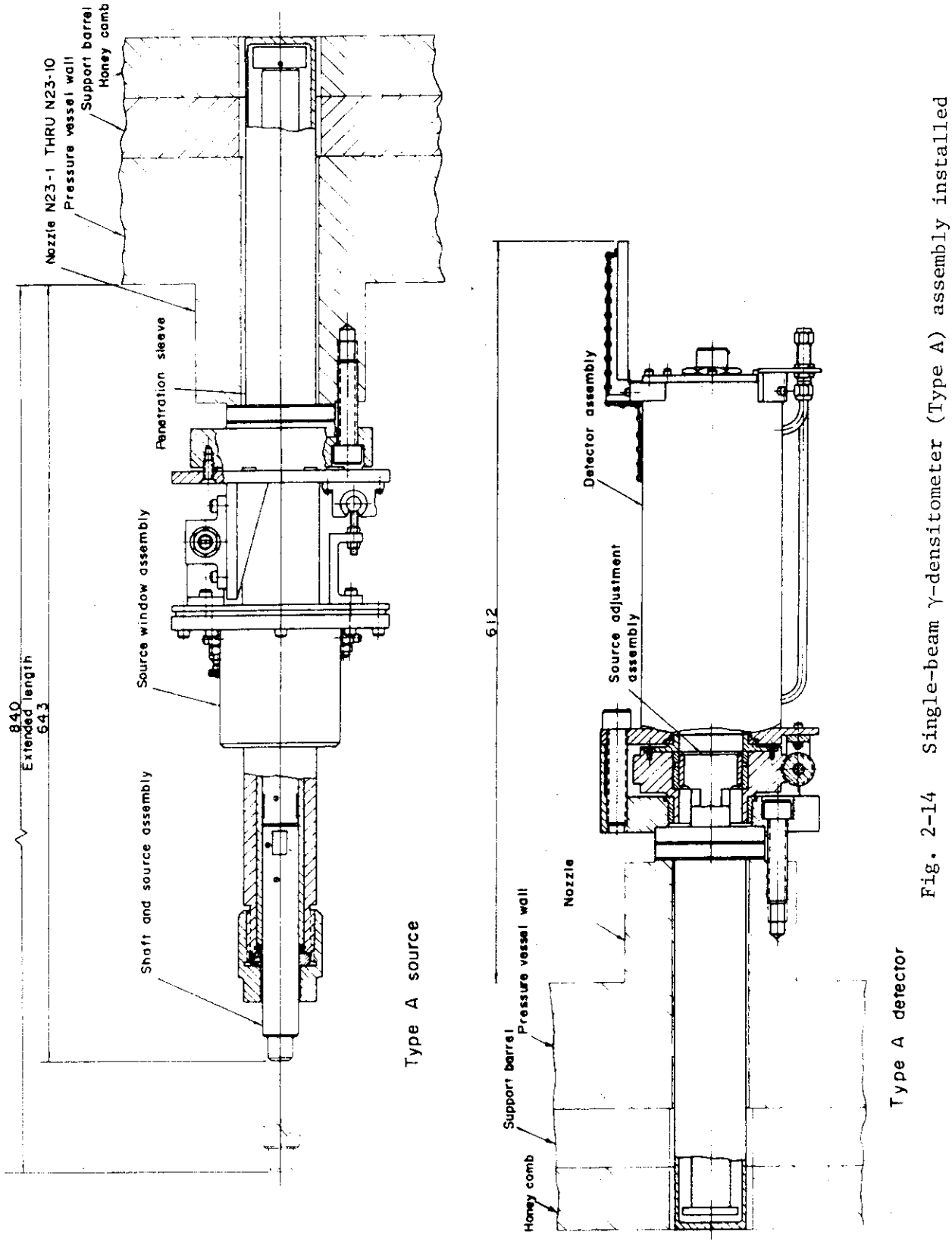

Fig. 2-14 Single-beam γ-densitometer (Type A) assembly installed in core

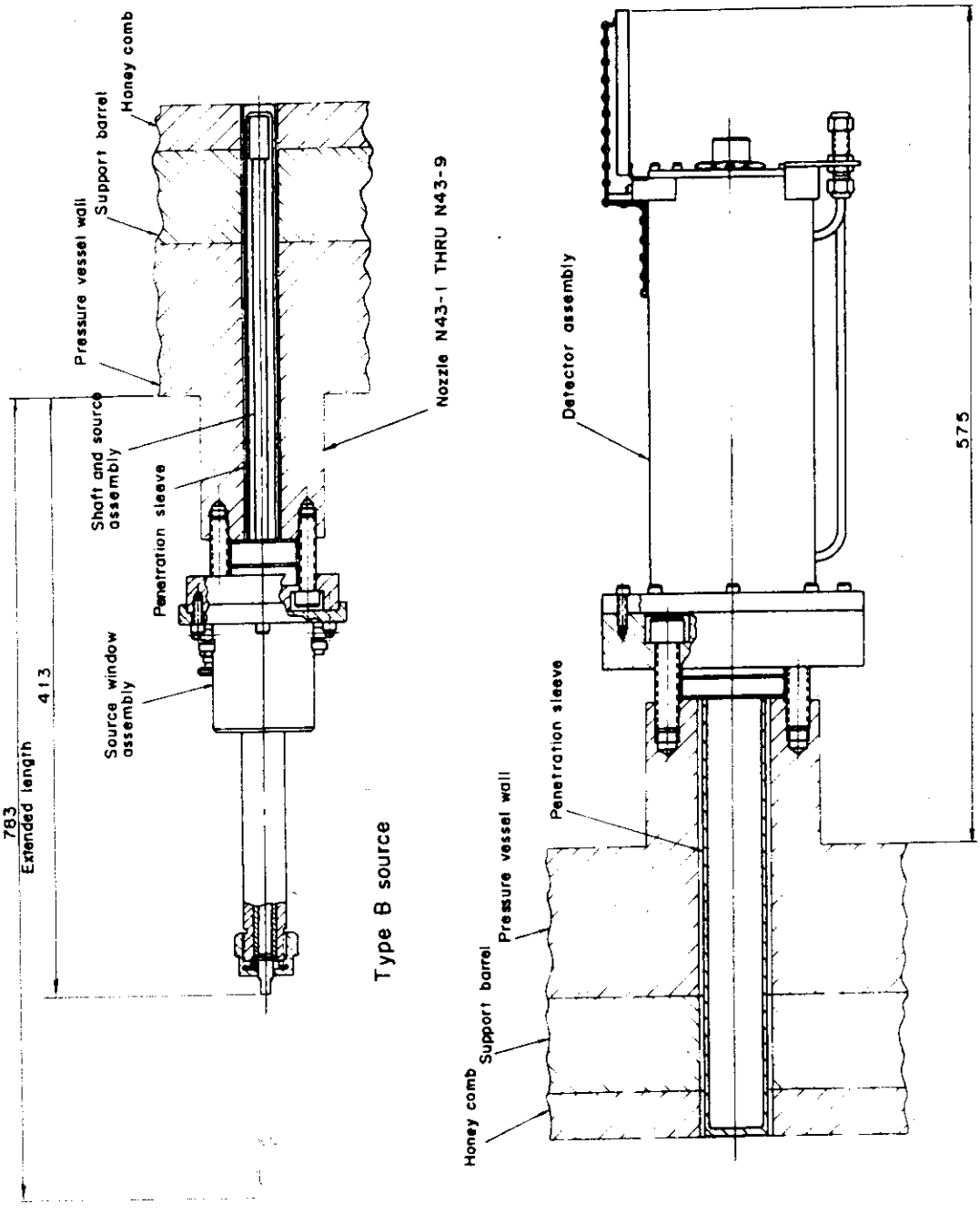

Fig. 2-15 Single-beam γ-densitometer (Type B) assembly installed in upper plenum and below end box tie plate

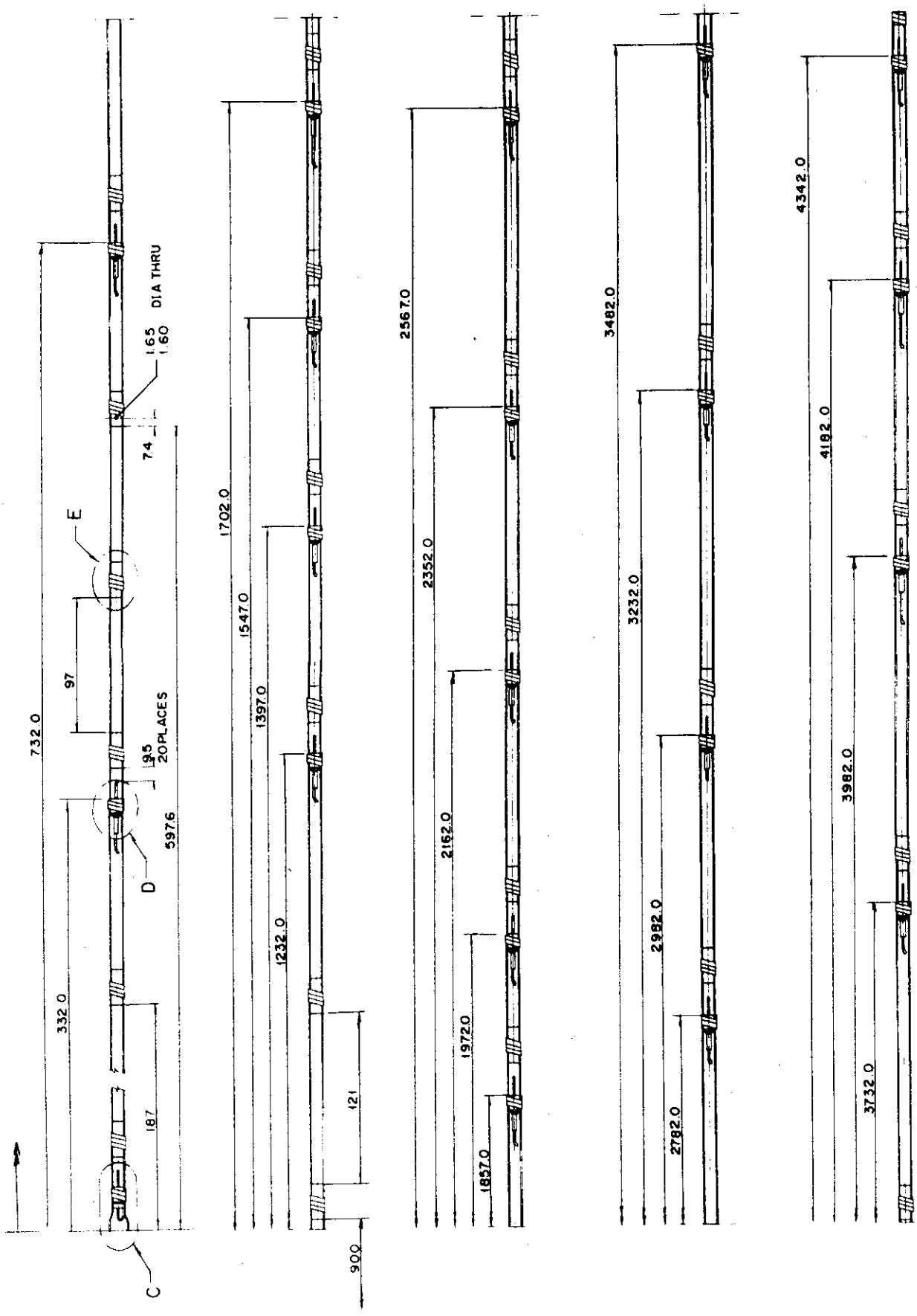

Fig. 2-16 LLD assembly

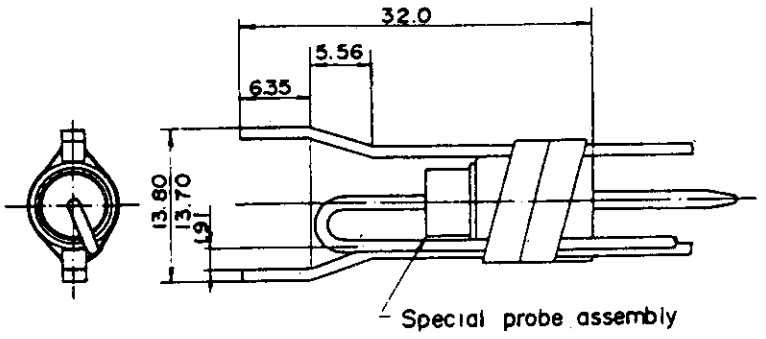

C

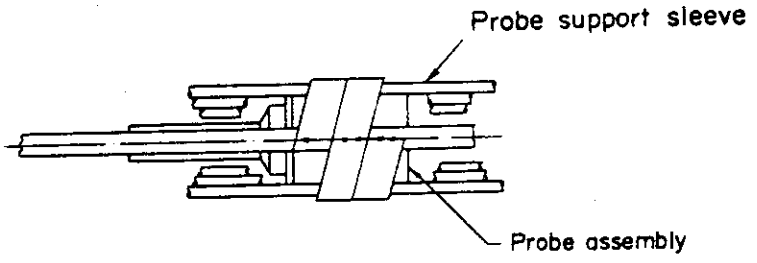

D

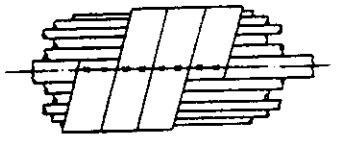

E

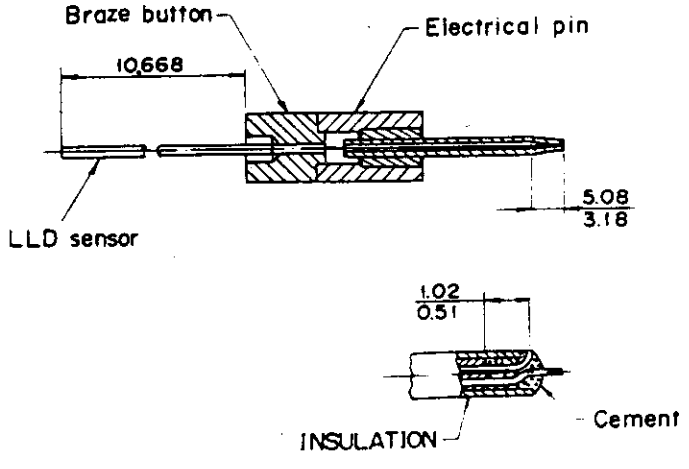

Fig. 2-17 LLD sensor

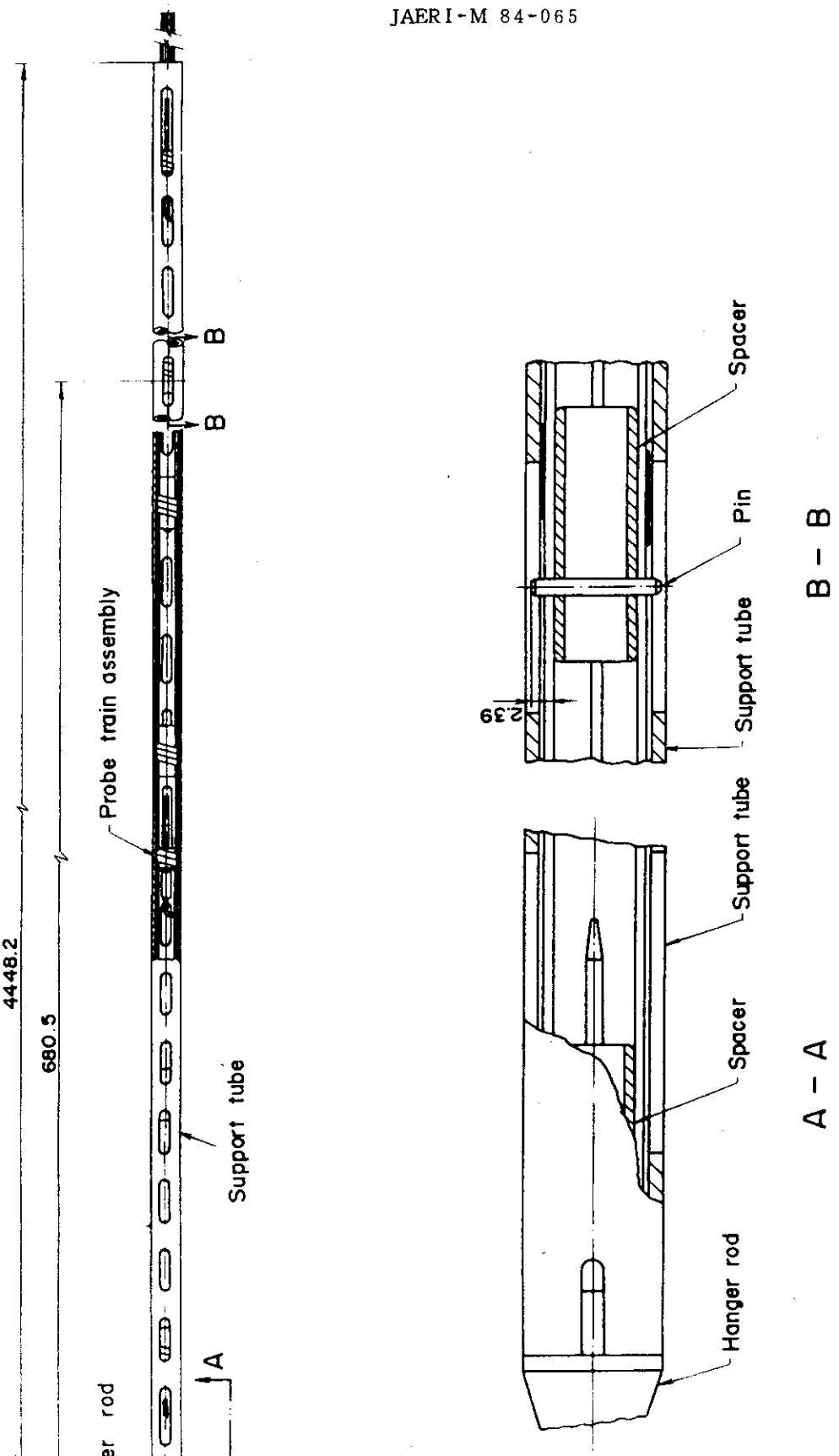

Fig. 2-18 LLD rod

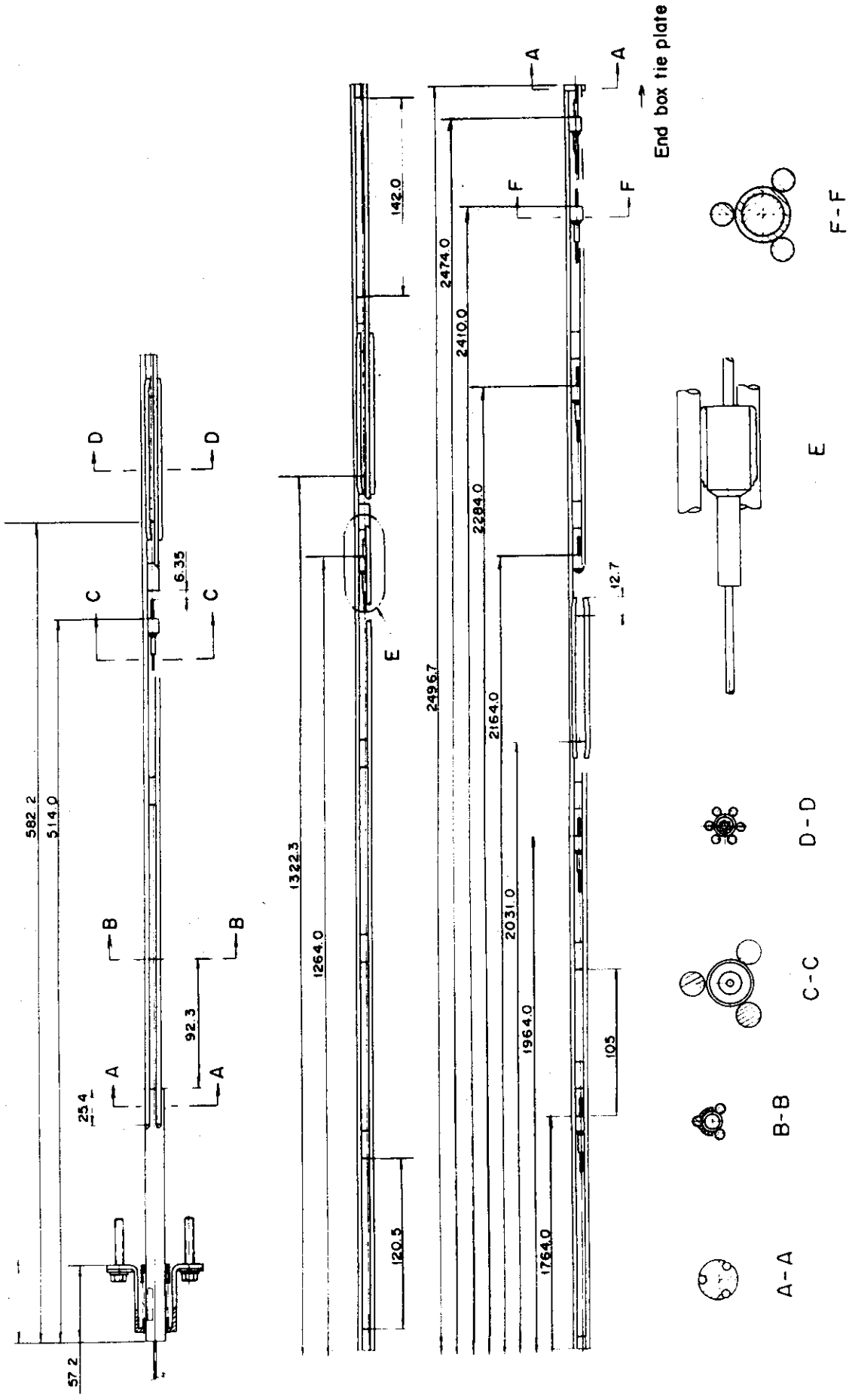

Fig. 2-19 Upper plenum FDG assembly

Fig. 2-20 Downcomer FDG assembly

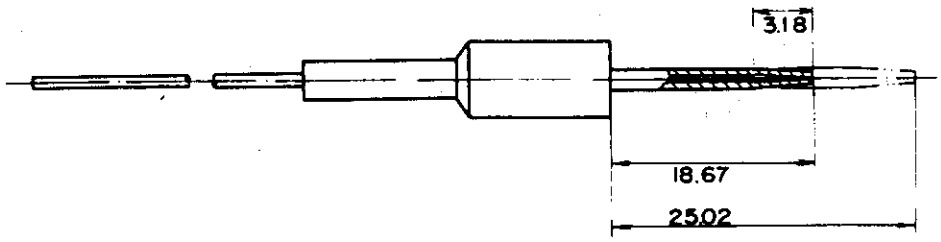

FDG sensor

Fig. 2-21 FDG sensor

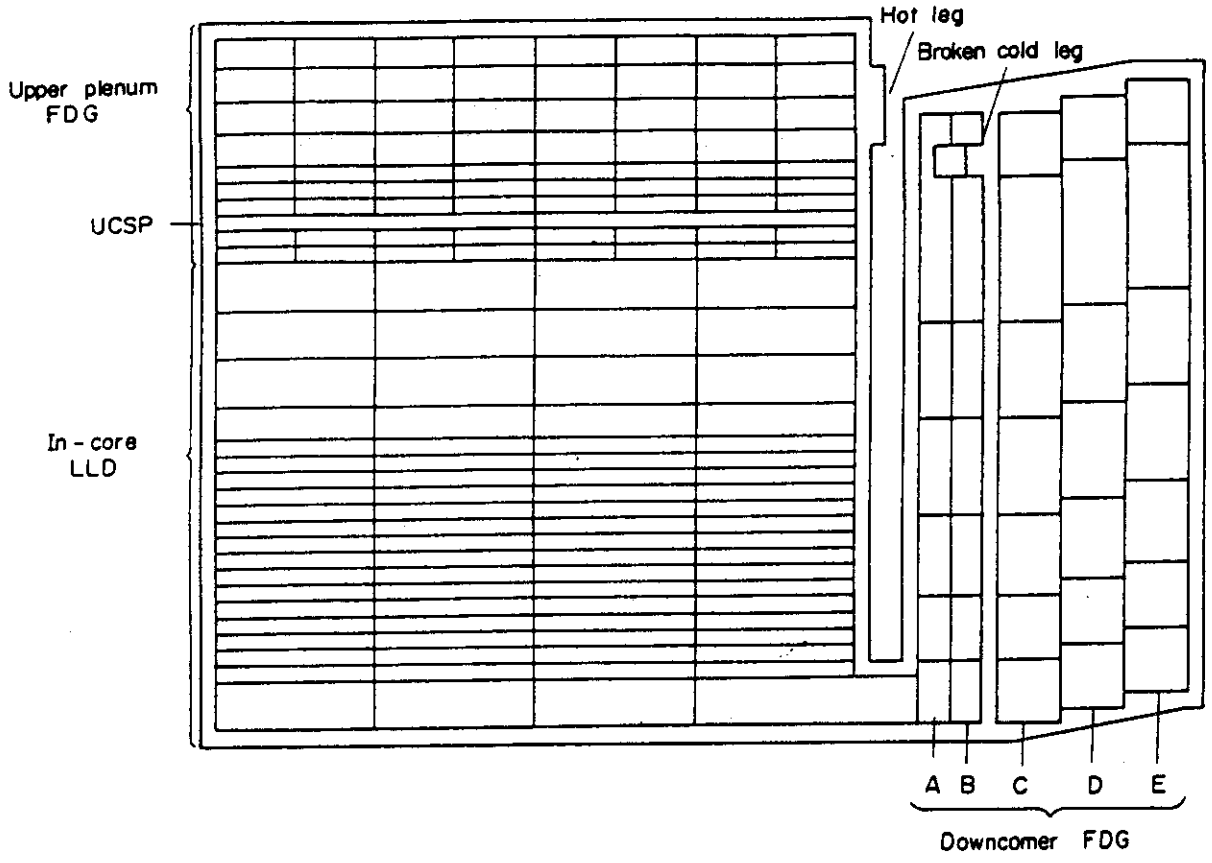

Color identification

(1) Upper plenum FDG and In-core LLD

dry = white

wet = black

(2) Downcomer FDG

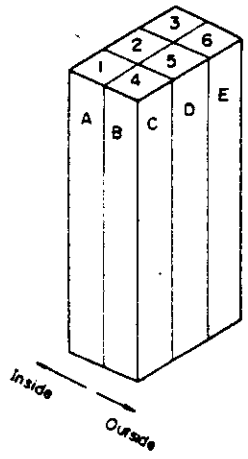

Display position	A	B	C	D	E
Rod No.	1	4	1 and 4	2 and 5	3 and 6
Color identification	dry = white wet = black		both dry = white both wet = black Inside wet, Outside dry > blue Inside dry, Outside wet > light blue		

Fig. 2-22 Display format of LLDs and FDGs

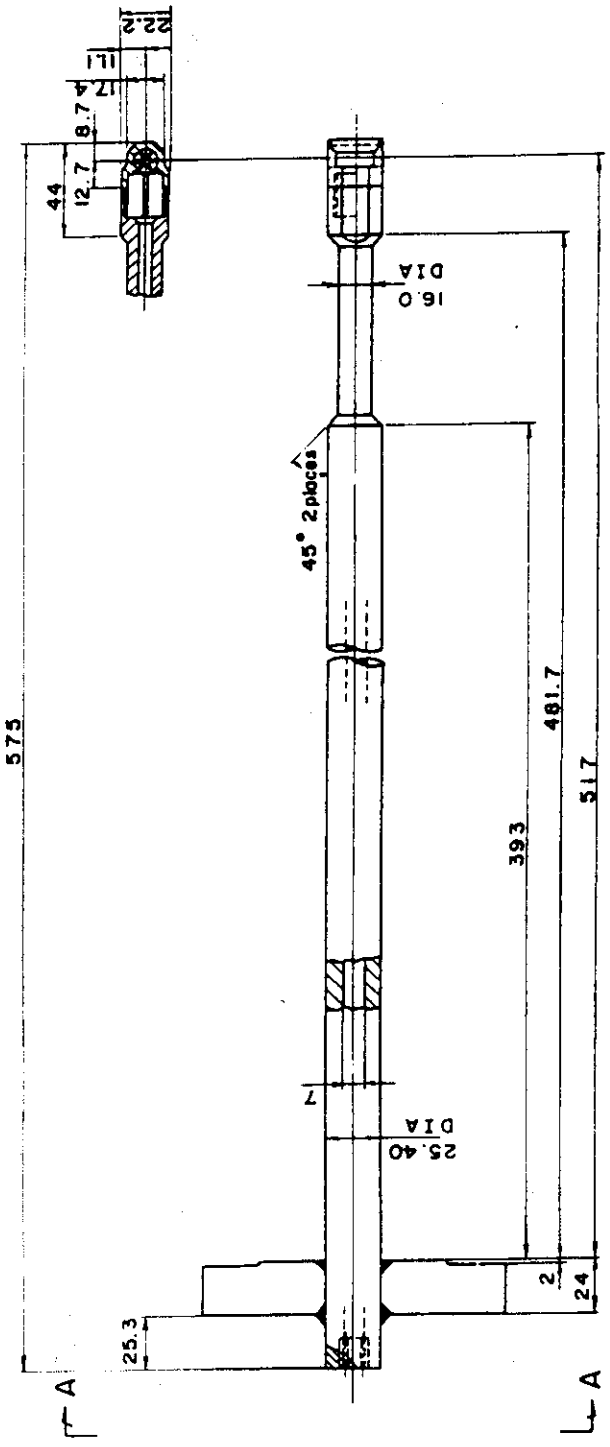

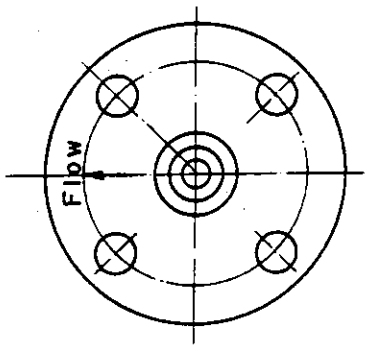

Fig. 2-23 Turbine flowmeter in upper and lower plenum

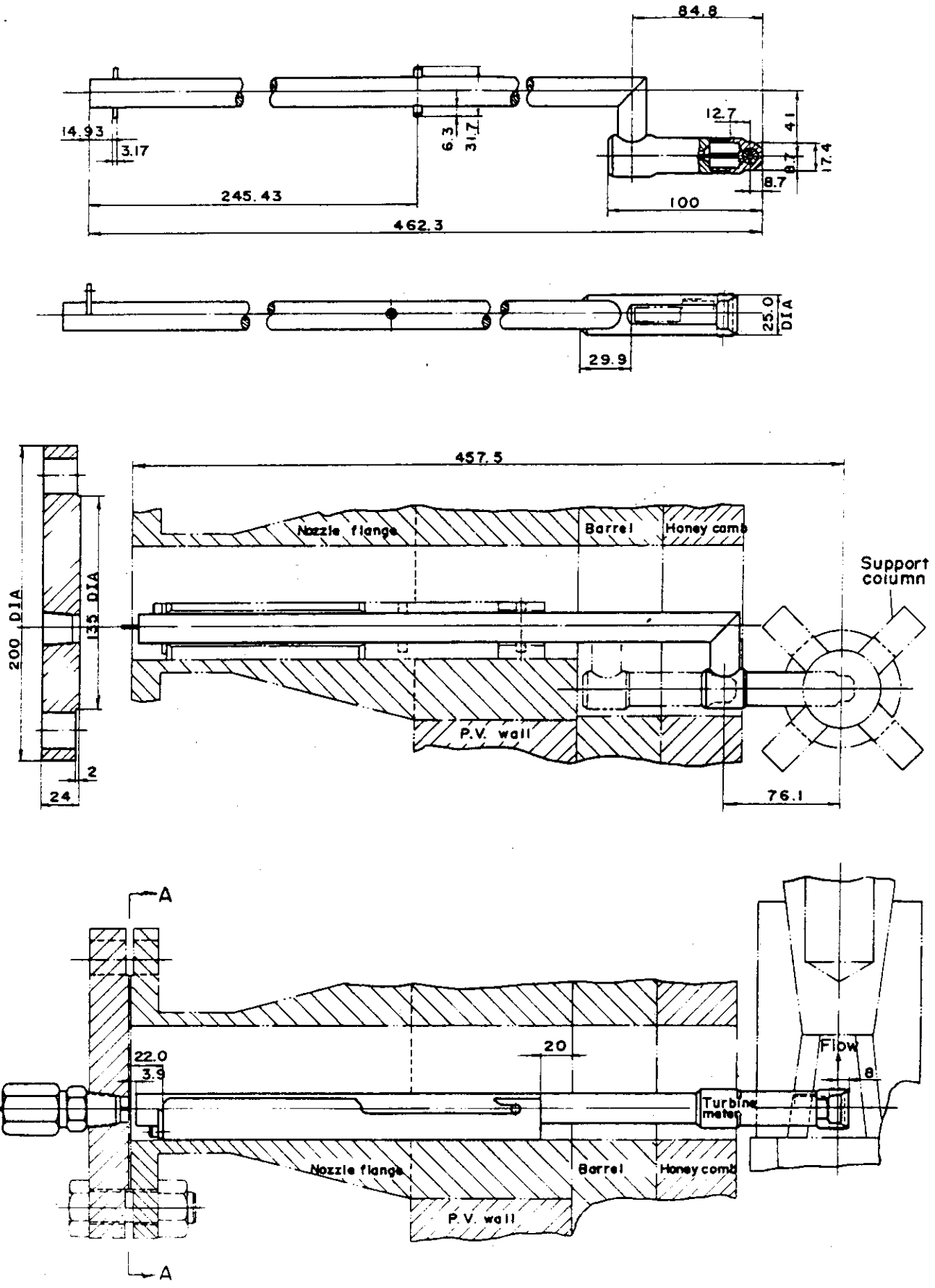

Fig. 2-24 Turbine flowmeter just above UCSP holes

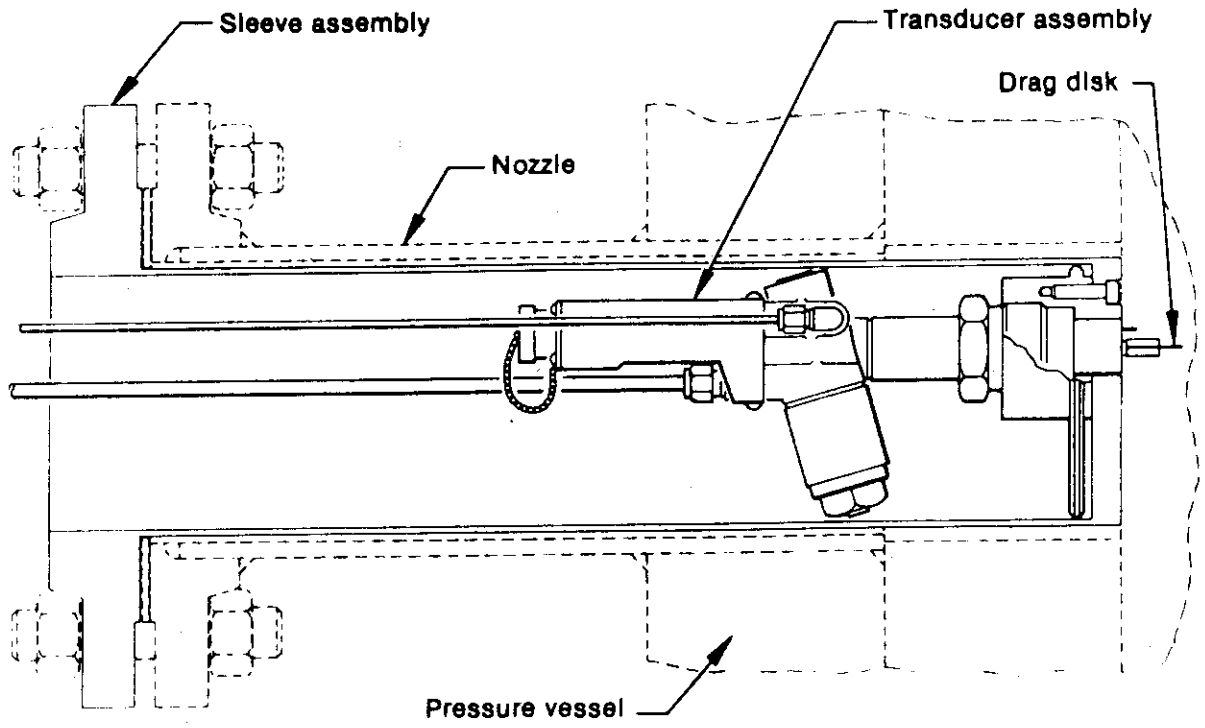

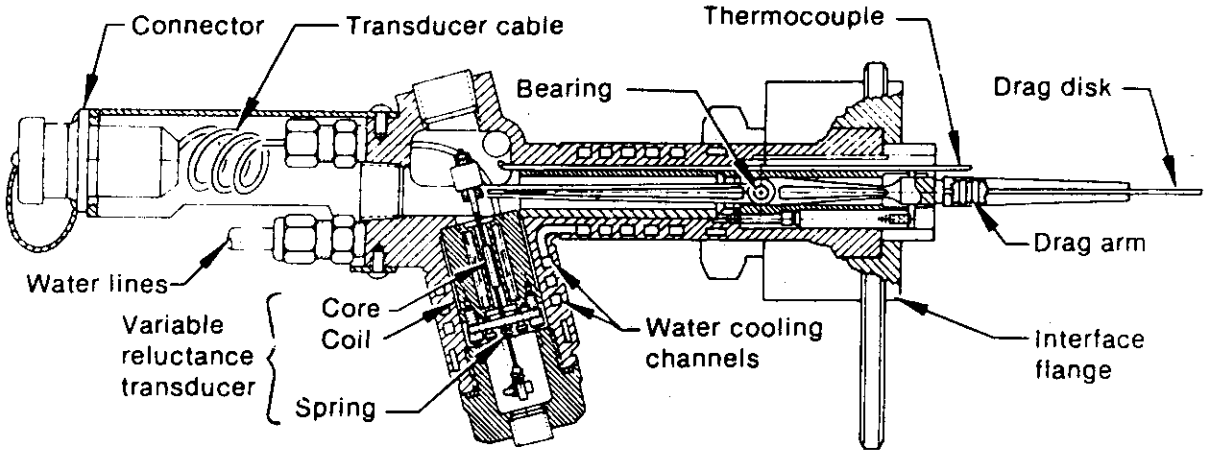

Fig. 2-25 Downcomer drag disk assembly

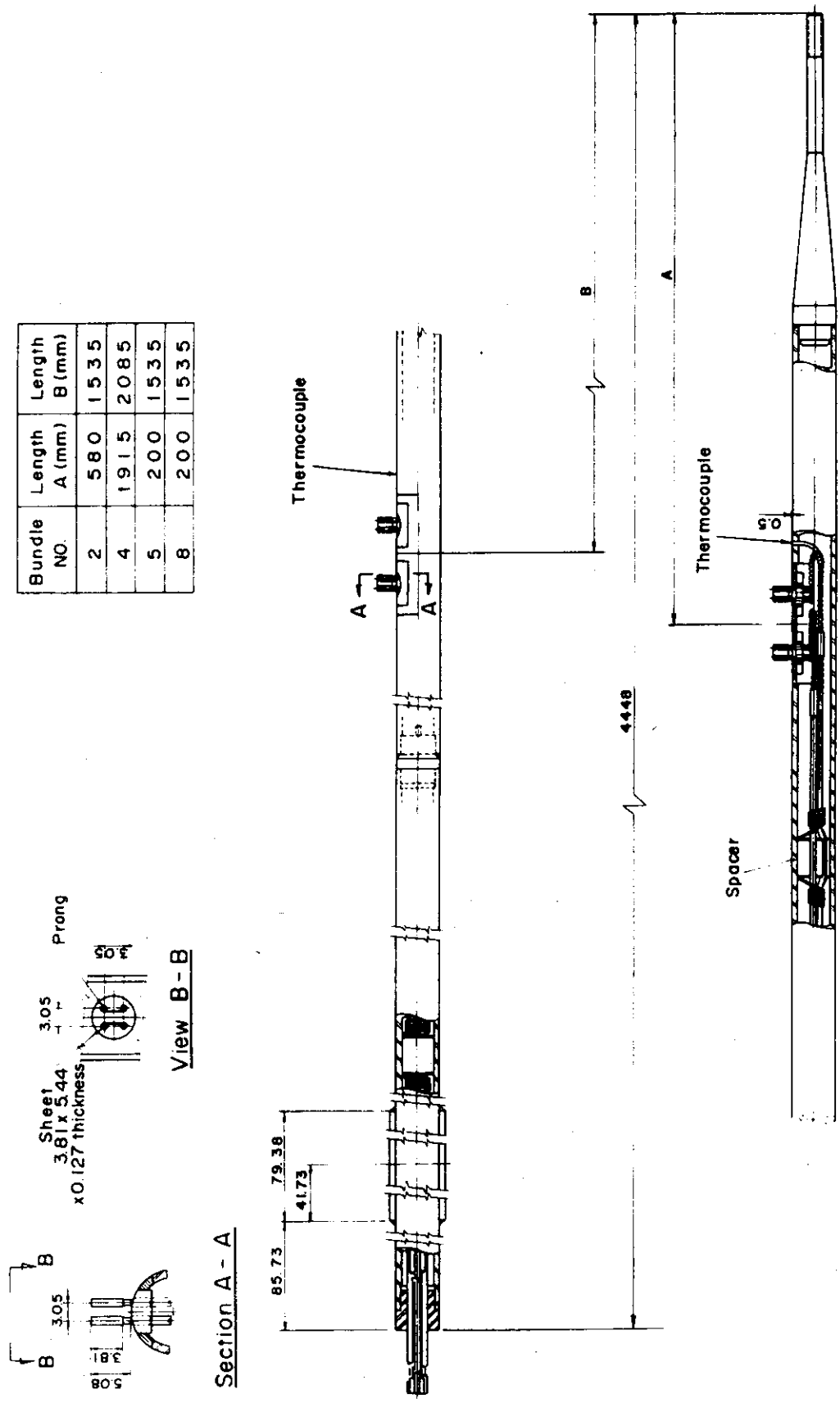

Fig. 2-26 In-core flag probe assembly

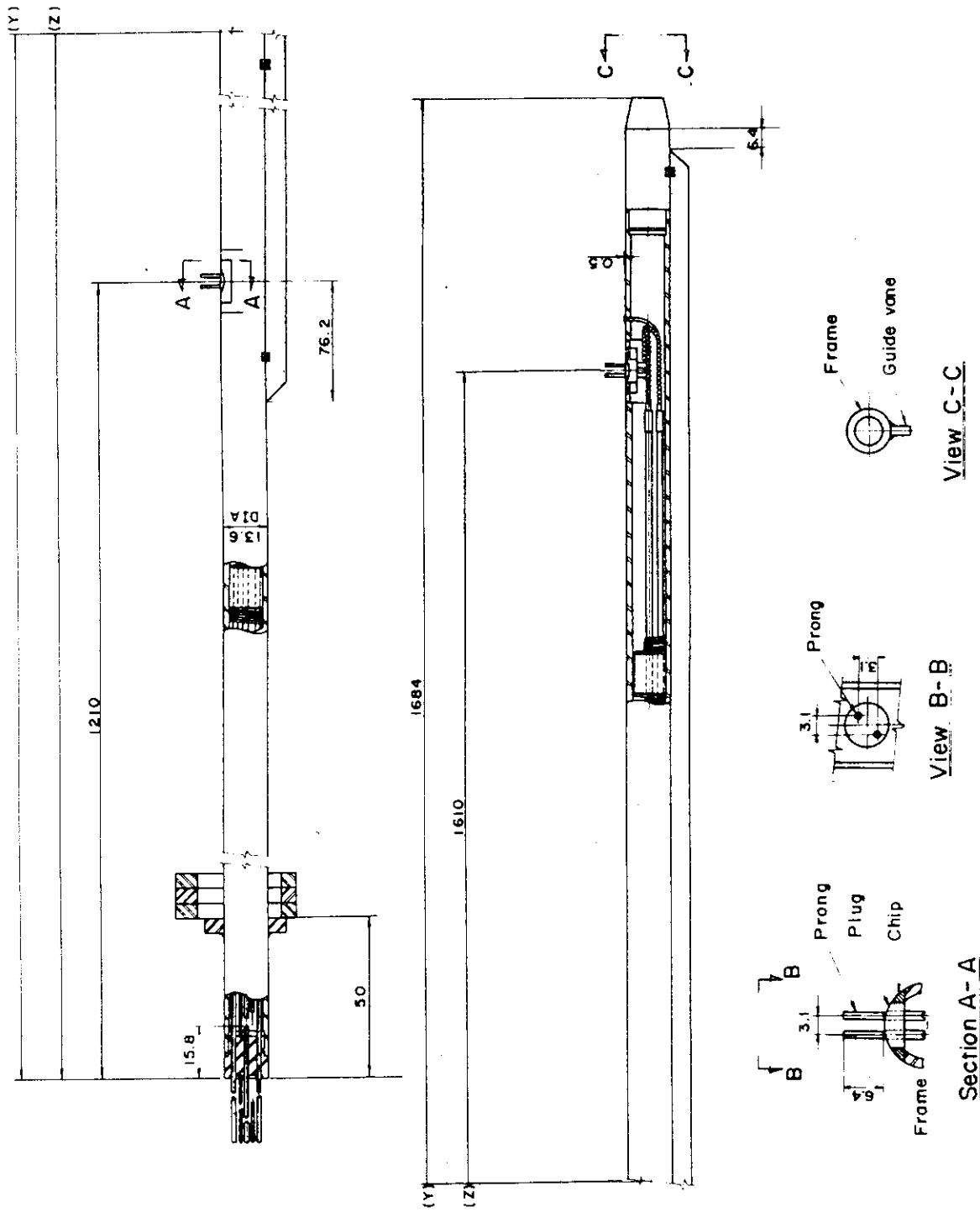

Fig. 2-27 Upper plenum prong probe assembly

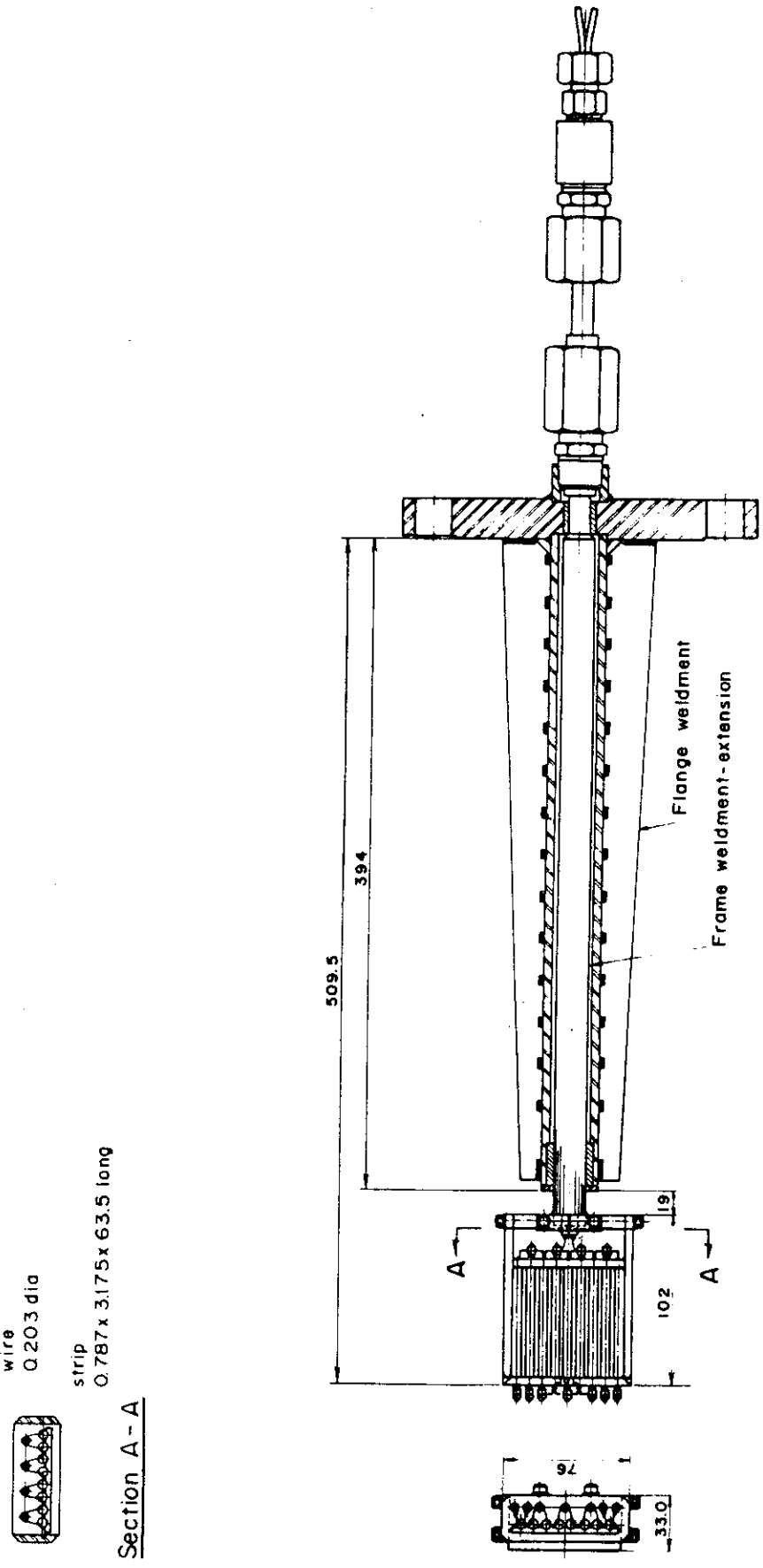

Fig. 2-28 Downcomer string probe assembly

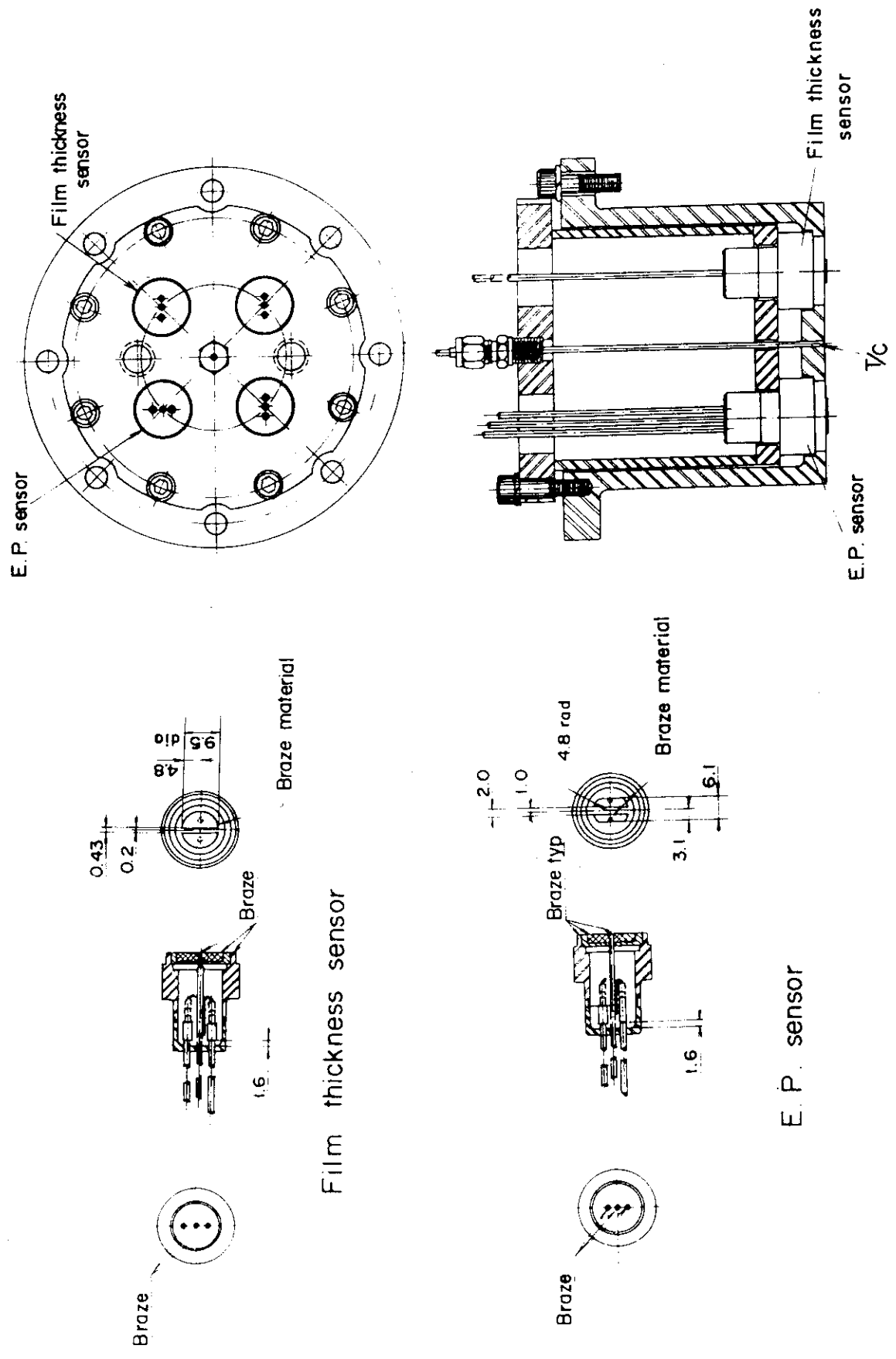

Fig. 2-29 Wall film probe assembly

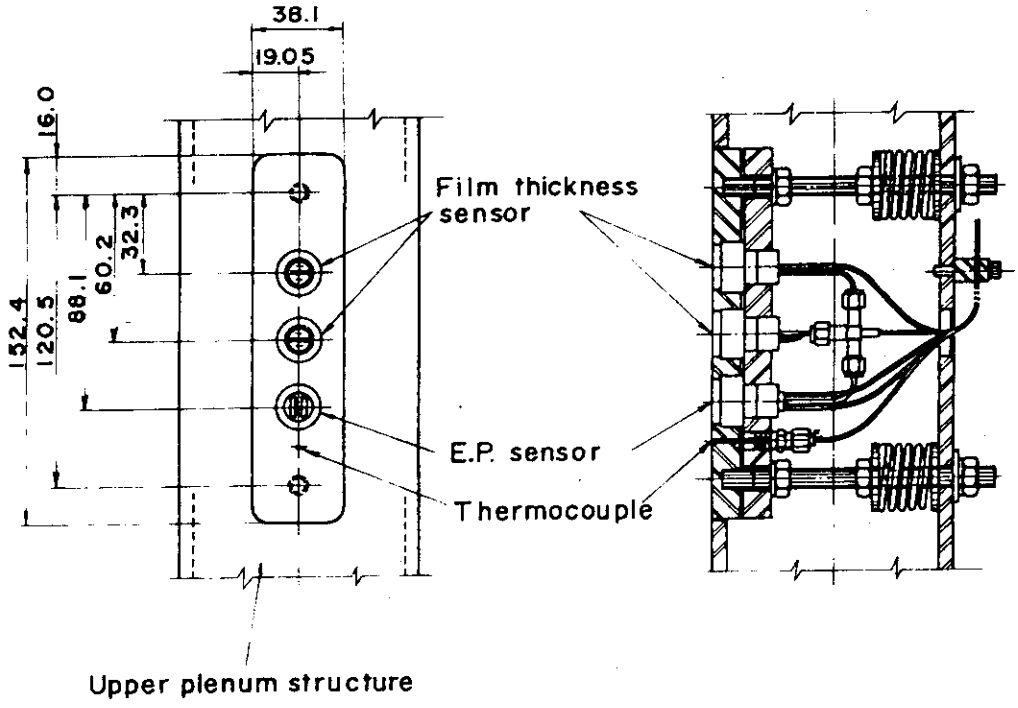

Fig. 2-30 Upper plenum film probe assembly

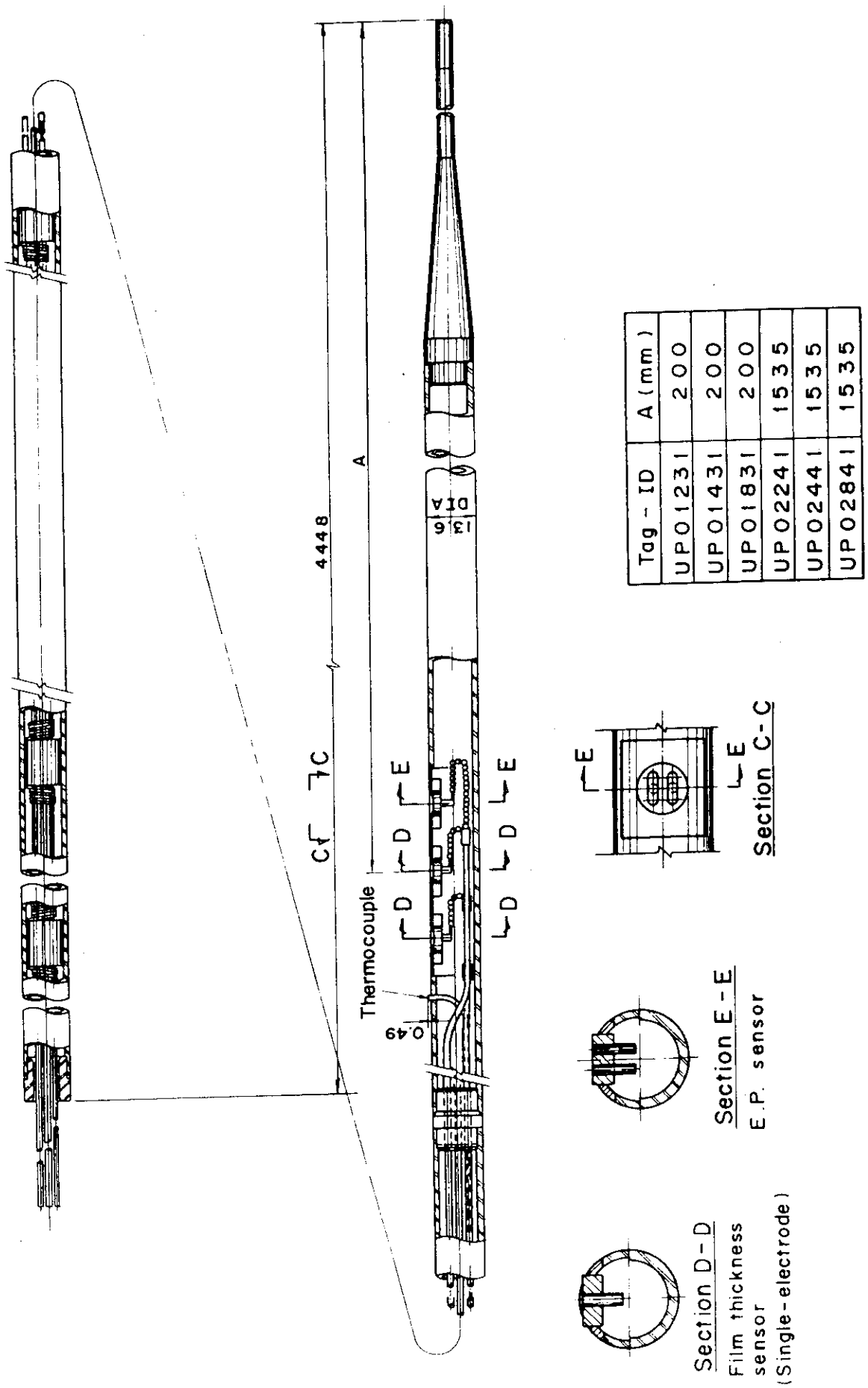

Tag - ID	A (mm)
UP01231	200
UP01431	200
UP01831	200
UP02241	1535
UP02441	1535
UP02841	1535

Fig. 2-31 In-core film probe assembly

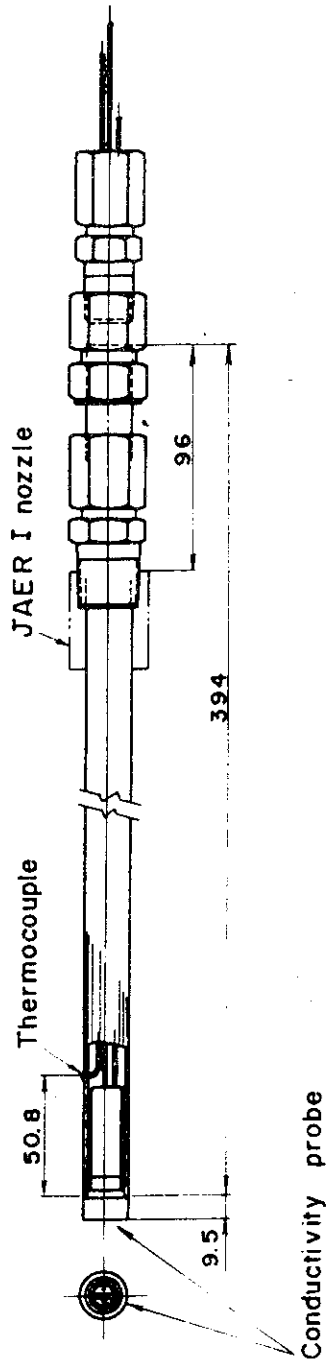

Fig. 2-32 Reference conductivity probe assembly

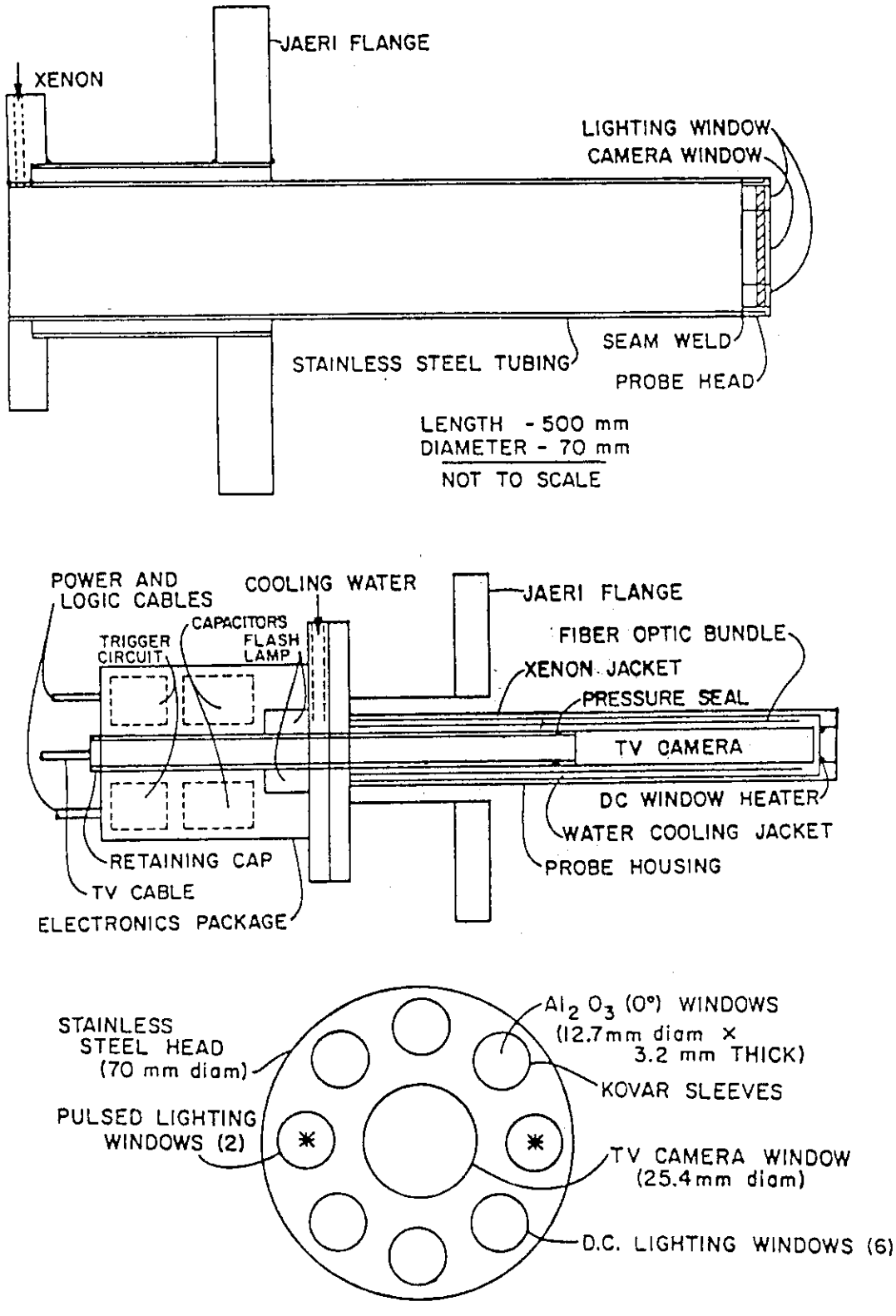

Fig. 2-33 Video optical probe

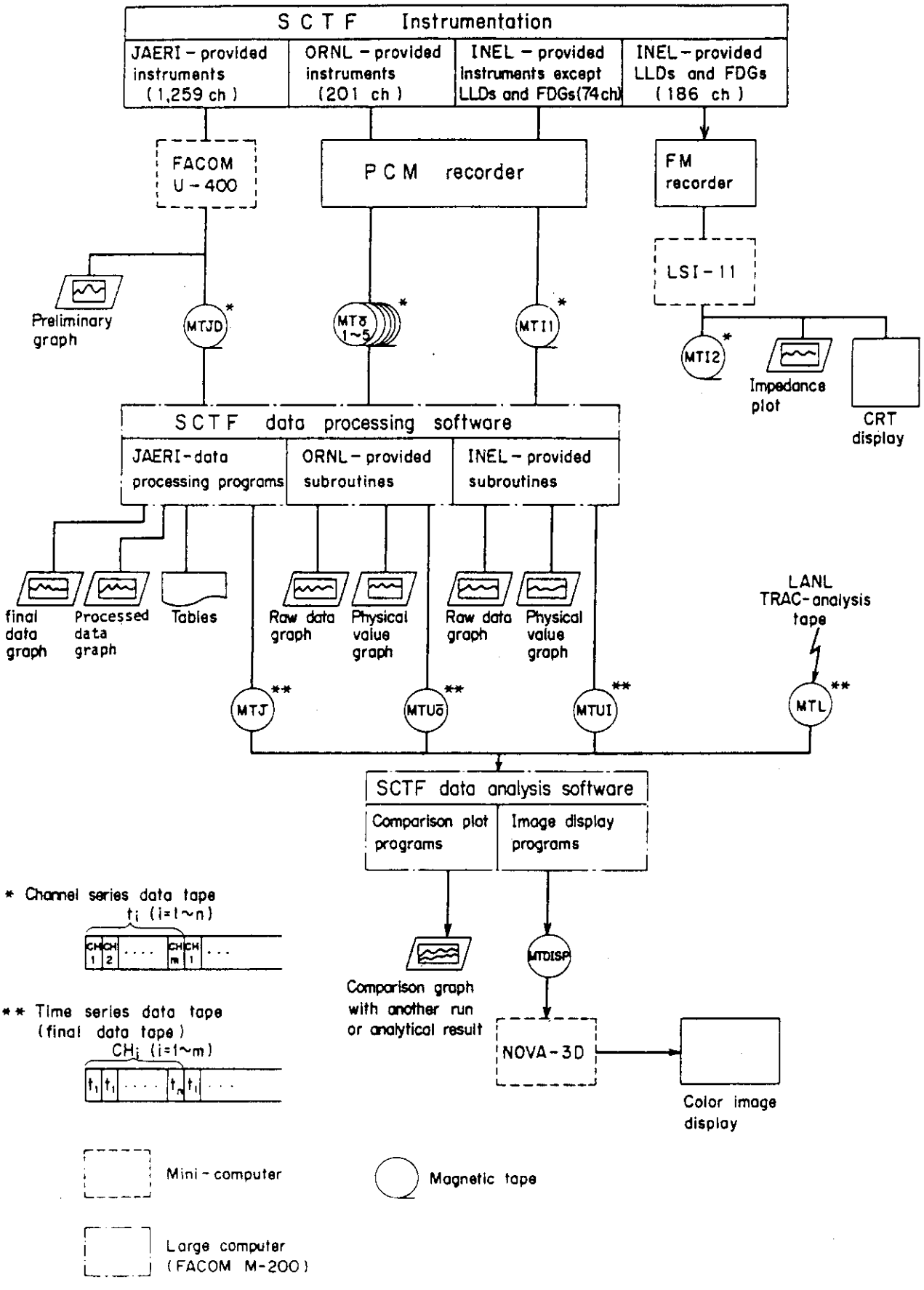

Fig. 2-34 Flow diagram of data reduction procedure

3. Evaluation of USNRC-Provided Instrumentation

3.1 Spool Piece

3.1.1 Hot Leg Spool Piece

3.1.1.1 Void Fraction

Figure 3-1 shows the comparison between the whole pipe average void fraction measured with the four γ-densitometers in the hot leg spool piece and the void fraction calculated from vertical differential pressure data in the horizontal part of hot leg. As shown in this figure, the void fractions measured with the hot leg spool piece agree well with the void fractions calculated from the differential pressure data.

3.1.1.2 Steam Velocity

Comparison between the hot leg fluid velocity at region-1 (top region out of the vertical 4 regions of the cross section) and/or region-2 (the second top region) measured with the hot leg spool piece and the hot leg steam velocity calculated from the conventional instruments are shown in Fig. 3-2. The steam velocity data were calculated as the sum of mass flow rates, MgI and MgII in Fig. 3-2 measured with the venturi and the orifice, because accumulated mass of steam in the containment tank-I was negligible. And in this calculation variation of effective steam flow area of the hot leg due to the change of liquid level was taken into account by using the vertical differential pressure data in the hot leg. The fluid velocity at the region-1 measured with the hot leg spool piece agree well for Tests S1-SH2, and S1-03 with the steam velocity calculated from the Venturi and orifice flow rate data as shown in Figs. 3-2 (a) and (b). On the other hand in Test S1-02 and S1-05, it is found that the steam velocities lie between the fluid velocities at the region-1 and the region-2 as shown in Figs. 3-2 (c) and (d). These results seem reasonable.

3.1.1.3 Total Mass Flow Rate

Comparison between the total mass flow rate measured with the hot leg spool piece and the mass flow rate calculated from the conventional

instruments are shown in Fig. 3-4. The mass-flow rate from the conventional instruments was calculated as the sum of the following mass flow rates: MgI measured with the venturi and MgII measured with the orifice, and the following water accumulation rates: $M_{\ell,s/w}$ in the steam/water separator, $M_{\ell,II}$ in the containment tank-II, $M_{\ell,Inlet}$ in the inlet plenum simulator and $M_{\ell,Hot\ leg}$ in the steam/water separator side of the hot leg, as shown in Fig. 3-3.

The total mass flow rate measured with the hot leg spool piece in these figures agree well with the mass flow rate calculated from the conventional instruments except the middle period in Test S1-SH2 and the early period in Tests S1-01, S1-05 and S1-09. Causes of the temporary disagreement have not been identified yet.

The oscillatory behavior observed in the total mass flow rate measured with the hot leg spool piece in the later period of each test may be attributed to the fluctuation of fluid density and momentum flux which are caused by the complex two-phase oscillation.

3.1.1.4 Hot Leg Flow Reversal

The mass flow rates in four regions of the hot leg spool piece are shown in Fig. 3-5 for Test S1-01. The mass flow rate in region 4 (bottom region) becomes negative at 132 seconds after the BOCREC (Bottom of Core Recovery), indicating the flow reversal at the bottom part of the hot leg. The flow reversal was observed at the lower part of hot leg through the view window. The occurrence of flow reversal is also confirmed by the data of differential pressure across steam/water separator inlet plenum simulator, liquid levels in hot leg, and liquid level in the upper plenum as shown in Fig. 3-6.

3.1.2 Cold Leg Spool Piece

3.1.2.1 Velocity

The steam, water and fluid velocity can be obtained separately with the cold leg spool piece by using the three-beam γ-densitometer, the full-flow turbine flowmeter and the drag screen transdncer. Figure 3-7 shows the steam (CSOOSV), water (CSOOWV) and fluid (CSOOFV) velocities for Test S1-20 (cold leg injection test). It is found from this figure that differences among these data are not recognized during the whole transient. This tendency is observed in all SCTF core-I tests.

Figure 3-8 shows the drag forces measured with three drag screen transducers for Test S1-20. From these three drag transducer data and the turbine meter data, the average fluid density can be calculated by the following equation as presented in Appendix B-3.

$$\rho_{ft} = \frac{I}{V_t^2} \quad , \tag{3-1}$$

where

ρ_{ft}: Average fluid density (kg/m^3),

I : Momentum flux = K ($F_1 + F_2 + F_3$) (kg/ms^2), sum of the three drag transducer engineering unit values, multiplied by the calibration constant K,

V_t : Turbine meter velocity (m/s).

The calculation flow chart for the cold leg spool piece is shown in Fig. B-2. As indicated in this flow chart, if the value of ρ_{ft} is smaller than ρ_s (steam density), the drag transducer data are rejected and the unity slip model is adopted. In the present test, the drag force of "UD03ZS" is negative and the absolute value is almost the same as the drag force of "UD01ZS" as shown in Fig. 3-8, resulting very small momentum flux I and very small fluid density ρ_{ft} according to equation (3-1). Therefore, the ρ_{ft} is smaller than the ρ_s and the steam, water and fluid velocities have the same value due to the unity slip model path in Fig. B-2. The above-mentioned sign reversal of the output signal from "UD03ZS" will be corrected by software.

3.1.2.2 Mass Flow Rate

Comparison between the mass flow rate measured with the cold leg spool piece and the steam mass flow rate measured with the Venturi at the intact cold leg are shown in Fig. 3-9 for the forced flooding tests. The spool piece mass flow rate almost agree with the Venturi steam mass flow rate. This result is reasonable because the steam flow rate in the intact cold leg should be equal to the steam flow rate in the broken cold leg under the forced flooding condition. In the cold leg injection test, bypass water mass flow rate is measured by the cold leg spool piece. Figure 3-10 shows the water mass flow rate measured with the

cold leg spool piece for Test S1-20. On the other hand, Fig. 3-11 shows the bypass water mass flow rate measured by the liquid level transient in containment tank - I (M_{ℓ}, I, shown in Fig. 3-3).

Since the mass flow rate measured with the cold leg spool piece is not reliable as described previously, these two mass flow rates cannot be quantitatively compared. However, it is recognized that the rapid increase of mass flow rate at about 450 seconds after the BOCREC in Fig. 3-10 is corresponding to the rapid increase of water mass flow rate in Fig. 3-11 with the delay time of about 30 seconds.

3.2 Pressure Vessel γ-Densitometer

3.2.1 In-Core γ-Densitometer

Ten γ-densitometers are installed on the vessel wall so that the γ-beams penetrate the gap between the core bundles at three elevations as shown in Fig. A-1.

Figure 3-12 shows the transients of fluid densities measured with the γ-densitometers at each location in the core for Test S1-08 (steep power profile test).

The overscales shown in the fluid densities at the elevation of 1.905 m are due to the obstruction of the γ-beam by the movement of rod bundles.

As generally shown in Fig. 3-12, the fluid density in the core gradually increases during the quench propagation period and reaches almost constant value after the quench of the whole core (383 sec). Before the whole core quench time, the fluid density is higher at the lower elevation. These overall tendencies qualitatively agree with the data of vertical differential pressures as discussed in section 3.2.2.

After the quench of the whole core, the highest fluid density is observed at the gap between bundles 7 and 8 and the lowest fluid density is observed at the gap between bundles 1 and 2 at the elevation of 3.235 m. On the other hand, the horizontal differential pressure at the elevation of 3.235 m indicates that the direction of cross flow is from bundle 8 toward bundle 1 at this elevation[2]. Therefore, the above-mentioned horizontal distribution observed in the fluid density at the elevation of 3.235 m is qualitatively reasonable. It is also suggested from the significant higher fluid density at the bundle 8

side at the upper part of core that the more water fall back occurs at the bundle 8 side than at the bundle 1 side.

3.2.2 Comparison of Void Fractions Measured with γ-Densitometers and D/P Cells

The void fractions calculated from the fluid densities measured with the γ-densitometers are compared with those calculated from the vertical differential pressures as shown in Fig. 3-13. The differential pressure measurement sections for the comparison with the γ-densitometers are above and below the measurement locations of the corresponding γ-densitometers as shown in Fig. 3-14. In addition, the differential pressures are measured along the center line of bundles 2 and 8 while the compared γ-densitometer beam penetrates at the gap between bundles 1 and 2 or at the gap between bundles 7 and 8.

It is generally seen in Fig. 3-13 that the γ-densitometer gives higher void fraction than the differential pressure especially at the upper part of the core and at the Bundle 1 side, while relatively good agreement is obtained at the lower part of the core and at the Bundle 8 side. The above characteristics are also observed in the test results from the Semiscale small break experiment S-PL-4[9].

The reason for the discrepancy between the void fractions obtained from the γ-densitometer and from the vertical differential pressure has not clearly been explained yet. However the following reasons are considered to contribute to the above-mentioned discrepancy.

1) Effect of liquid film on the core wall and on the non-heated rod

As suggested from the data of core side wall film probes presented in Fig. 3-26, there exist liquid film flow on the core side wall above the quench front. In addition, the liquid film also exist on the surface of non-heated rods because the non-heated rods are quenched before the quench of the heater rods at the same elevation. However, the liquid film on the side wall is considered to bypass the γ-densitometer nozzles which penetrate the core side wall. And furthermore, the γ-beam is not affected by the liquid film on the non-heated rods because the γ-beam penetrate through the gap between bundles. On the other hand, the gravitational pressure drop includes the effect of liquid films both on the core side walls and on the non-heated rods.

Therefore, the void fraction calculated from the differential pressure is lower than the void fraction measured with the γ-densitometer.

2) Difference of measurement locations

As mentioned before, the γ-beam penetrates through the gap between rod bundles while the differential pressure is measured along the center line of each bundle. The gap between rod bundles is 4.8 mm and 1.33 times larger than the gap between rods of 3.6 mm. Furthermore, there are no non-heated rods at the peripheral part of each bundle, whereas there are 22 non-heated rods out of 256 rods in each bundle. Along the non-heated rod, the water fall back from the upper plenum into the core was observed by using a high speed camera[3]. In addition, the water droplets coming from the lower part of the core are easily traped by the non-heated rod but spattered by the heater rod above the quench front.

Therefore, the average fluid density is higher in the rod bundle than at the gap between rod bundles especially above the quench front.

3) Effect of frictional pressure drop

The vertical differential pressure includes the frictional and accelerational pressure drops as well as the gravitational pressure drop which is directly converted into the void fraction. If the frictional and accelerational pressure drops are excluded, the void fraction is estimated to be higher.

The maximum contribution of the frictional pressure drop to the void fraction was estimated to be about 2 % at the top of the core and about 1.5 % at the middle elevation of the core[4]. Since the discrepancy of void fractions is much larger than 2 %, the effect of frictional pressure drop is not the major reason for this discrepancy.

The contribution of the accelerational pressure drop is estimated to be much less than the contribution of the frictional pressure drop under the reflood phase[4].

3.2.3 Fluid Density below End Box Tie Plate

Figures 3-15 (a) and (b) show the fluid densities between the end box tie plate and the top grid spacer of bundle 2 measured with the γ-densitometer and the void fractions calculated from the γ-densitometer

data for Test S1-SH2 (high pressure test) and Test S1-02 (low pressure test), respectively. The flow pattern transition times identified by the observation results with the video optical probe located between the end box tie plate and the top grid spacer of bundle 3 are also indicated in Fig. 3-15. The transition from the droplets flow to the churn-turblent flow occurred at the void fractions of about 0.988 for Test S1-SH2 and about 0.961 for Test S1-02, respectively.

3.2.4 Fluid Density in Upper Plenum

Figure 3-16 shows comparisons between the void fractions calculated from the fluid densities measured with the γ-densitometers and the void fractions calculated from the liquid level measured with the D/P cells in the upper plenum. The measured liquid level is assumed to be the collapsed level above the Upper Core Support Plate (UCSP) though the lower end of the liquid level measurement span is 0.162 m below the upper surface of the UCSP as shown in Fig. 3-14. Furthermore, the froth level in the upper plenum is assumed to be saturated at the elevation of the bottom of the hot leg nozzle (1.05 m above the UCSP). Therefore, it should be noted that the viod fraction calculated from the liquid level is the average value between 0 and 1.05 m above the UCSP while the void fraction calculated from the fluid density is the local value at 0.695 m from the UCSP.

As shown in Fig. 3-16, the void fractions calculated from the γ-densitometers above bundles 2 and 4 are higher than those calculated from the liquid levels during the test. On the other hand, the void fractions calculated from the γ-densitometers above bundle 8 and above the core baffle are higher before 300 seconds and lower after 300 seconds than those calculated from the liquid levels. The above-mentioned characteristics indicate that the continuous liquid phase is always below the elevation of 0.695 m from the UCSP above bundles 2 and 4, whereas it exceeded the same elevation at about 300 seconds above bundle 8 and above the core baffle. In addition, the final void fractions calculated from the γ-densitometers almost agree with those from the liquid levels above the core baffle. The horizontal liquid level distribution above the UCSP after 300 seconds is mainly caused by the hot leg flow reversal as discussed in section 3.1.1.4.

3.3 Liquid Level Detector (LLD) and Fluid Distribution Grid (FDG)

3.3.1 In-Core LLD

Figure 3-17 shows the examples of output signals of the in-core LLD (Sensor Nos. 1 through 20) at bundle 2. Shown in Fig. 3-18 is the bubble plots for the LLD which show the wet or dry condition of the sensors. The decision of wet or dry condition was based on the threshold level of output voltage shown in Fig. 3-17. Sensors except Nos. 13, 14 and 15 did not work well.

3.3.2 Upper Plenum FDG

The examples of output signals and bubble plots for the upper plenum FDG No. 8 are shown in Figs. 3-19 and 3-20, respectively. The transients of output signals for Sensor Nos. 1, 2 and 4 seem to be reasonable. However, most of the data show unreasonable behavior. Therefore, the upper plenum FDGs provided no usefull information on the overall fluid behavior in the upper plenum.

The reason why most of the LLD and FDG sensors did not work well is the hard cable problem as discussed in section 4.4.

3.4 Turbine Flowmeter

3.4.1 UCSP Hole Turbine Meter

Eight turbine meters are installed at the elevation of 37 mm above the UCSP. The location is as follows;

above Bundle 1 : Open hole,
above Bundle 2 : Guide tube,
above Bundle 3 : Support column,
above Bundle 4 : Support column,
above Bundle 5 : Open hole,
above Bundle 6 : Guide tube,
above Bundle 7 : Support column, and
above Bundle 8 : Guide tube.

Shown in Figs. 3-21 (a) through 3-21 (h) are the comparisons between the turbine velocities and the average superficial steam velocities defined based on the total area of UCSP holes which are

obtained with the mass-balance calculation.[7] Some of the turbine velocities and the calculated steam velocities qualitatively agree well just after the BOCREC. However, the turbine velocity seems to be more sensitive than the calculated steam velocity. In this period, it is considered that the flow passing the UCSP hole is almost steam single-phase and the turbine velocity can be regarded to indicate the steam velocity. Based on this fact, another steam velocity was estimated with the differencial pressure between the two points at 5 mm and 56 mm above the end box tie plate. The total area A_1 of tie plate holes per one bundle is,

$$A_1 = \frac{\pi}{4} (12)^2 \times 225 = 2.54 \times 10^4 \text{ mm}^2.$$

The flow area at 56 mm above the tie plate is,

$$A_2 = 220 \times 223 = 4.91 \times 10^4 \text{ mm}^2.$$

When the Bernoulli theorem is applied.

$$P_1 + \left(\frac{A_0}{A_1} U_g \right)^2 \frac{\rho_g}{2} = P_2 + \left(\frac{A_0}{A_2} U_g \right)^2 \cdot \frac{\rho_g}{2}$$

$$\therefore U_g = \left| \frac{2(P_2 - P_1)}{0.575\ \rho_g} \right|^{\frac{1}{2}} , \qquad (3\text{-}2)$$

where A_0 : Average flow area at UCSP hole per one bundle (2.25×10^4 mm^2).

U_g : Superficial steam velocity defined at A_0,

P_1, P_2 : Pressure at 5 mm and 56 mm above the tie plate, respectively,

ρ_g : Density of steam.

Broken lines shown in Fig. 3-21 are the calculated results with Eq. (3-2). Just after the BOCREC, the results by using Eq. (3-2) shows the similar characteristics with the turbine velocity.

Difference between the turbine velocity and the steam velocity obtained by mass balance calculation increases with time because entrained water flow rate from the core increases.

3.4.2 Upper Plenum Turbine Meter

Figure 3-22 shows the vertical steam velocity measured with the upper plenum turbine meters for Test S1-01. For reference, the average vertical steam velocities which calculated from the measured steam flow rate at the loops are also shown in this figure. The turbine meters give very low velocity compared with the calculated average vertical steam velocity.

Figure 3-23 shows the horizontal steam velocities measured with the upper plenum turbine meters for Tests S1-01. The data indicate that the measured horizontal steam velocities are much less than the available range of the turbine meters. Besides, the flow direction of steam would be very complicated in the upper plenum because of the upper plenum internals. Therefore, the horizontal steam velocities in the upper plenum are not well measured with the turbine meters.

3.4.3 Core Inlet Turbine Meter

Figure 3-24 shows the examples of the transients of core inlet water velocities measured with the core inlet turbine meters for Test S1-01. The data show the abnormal transients of core inlet water flow velocities. First of all, very high velocity (> 0.3 m/s) or very low velocity (< -1.0 m/s) is recorded so often both before and after the BOCREC. Besides, these values are much different from the average flow velocity seen in Fig. 3-25 for Test S1-01. Therefore, the core inlet turbine meters are not reliable at present stage. The flow velocity range for the tests is much less than the available range of the turbine meters.

3.5 Film and Impedance Probes

Among 26 film probes and 19 impedance probes, most of the instruments are not available due to the hard cable stress corrosion problem discussed in Section 4.4. In this section, some of the film and impedance probes which have no hard cable problems are evaluated for the data obtained in Test S1-02 (low pressure test).

3.5.1 Film Probe

The film thicknesses (upper and lower sensors in a probe) and average film velocity obtained from a core wall film probe and from an upper plenum structure film probe are shown in Figs. 3-26 and 3-27, respectively.

3.5.1.1 Film Thickness

The following characteristics of film thickness are observed in Figs. 3-26 and 3-27.

(1) The film thickness begins to increase at just after the BOCREC (106 sec) and reaches the maximum value at about 300 seconds for the core side wall film probe and 450 seconds for the upper plenum structure film probe.

(2) The film thickness signals from the upper and lower sensors in each film probe are very similar with each other.

(3) The film thickness data show very oscillatory behavior. The average maximum film thickness for the core side wall and the upper plenum structure film probes are about 2.4 mm and 4 mm, respectively, and the amplitude of oscillation is about 2 mm. At the period after reaching the maximum film thickness, however, the flow pattern around the film probes must be a bubbly flow and the probes are submerged in two-phase mixture as known from Fig. 3-28. Therefore, the values of the maximum film thickness are not reliable.

3.5.1.2 Film Velocity

As shown in Figs. 3-26 and 3-27, the data of average film velocities are very oscillatory. There are two kinds of oscillation; the larger amplitude of about ±1000 cm/sec and the smaller amplitude of about ±200 cm/sec.

Figure 3-29 shows the transient data of probe temperature, liquid conductivity, EP probe velocity, average coherence between the two film thickness signals, and wave velocity, which were used for the calculation of the average film velocity for the core side wall film probe. As shown in this figure, the EP probe velocity shows peculiar behavior while the data of probe temperature and liquid conductivity

seem to be reasonable. The average coherence between the two film thickness signals is always below 0.1 during the test. The very poor coherence may be due to the fact that the cross flow in the core disturbs the propagation of film wave between the two sensors in a film probe. Because of the very low coherence, the data of average film velocities are unreliable.

3.5.2 Impedance Probe (Flag, Prong and String Probes)

Since most of the impedance probles are not available due to the hard cable stress corrosion, only the void fraction data obtained from the upper plenum prong probes and the downcomer string probes are evaluated.

3.5.2.1 Upper Plenum Prong Probe

Figure 3-30 shows the void fractions measured with the upper plenum prong probes. As shown in this figure, both the relative capacitance void fraction and the corrected void fraction show exactly the same behavior, because the sensor loss angles were not satisfactorily measured and the calculation of corrected void fraction by using the loss angle data were not made in this test.

The following characteristics of void fraction are observed in Fig. 3-30.

(1) Before the BOCREC, the void fraction should be 1.0. However, two probes out of six indicate between 0.9 and 0.95.

(2) In general, the void fraction becomes lower at the hot leg side. This is consistent with the data of liquid level distribution in the upper plenum measured with the D/P cells as shown in Fig. 3-28(a).

Figure 3-31 shows the comparisons of the void fractions measured with the prong probes and the void fractions measured with the adjacent γ-densitometers. The locations of these instruments are shown in Figs. A-1, A-2 and A-6.

As the γ-denstitometer measures the average void fraction along the γ beam while the prong probe measures the local void fraction between the two small electrodes, the two void fractions are not necessary to agree with each other. However, there should be a similarity between the time histories of these two void fractions.

As shown in Fig. 3-31, the void fraction history above Bundle 4 measured with the prong probe is similar to that with the γ-densitometer. If the initial value is shifted to agree, the two void fraction histories almost agree with each other as illustrated in Fig. 3-31. On the other hand, the void fraction history above the core baffle region measured with the prong probe is much different from that with the γ-densitometer. Since the location of the prong probe is below the mixture level in the upper plenum after about 450 seconds as known from Fig. 3-28 (a), the void fraction should be much lower at this period as indicated by the data from the γ-densitometer. Therefore, the data from the prong probe seem to be doubtful.

3.5.2.2 Downcomer String Probe

Figure 3-32 shows the void fractions measured with the downcomer string probes and the liquid level in the downcomer for Test S1-14 (cold leg injection base case test). In order to measure the horizontal mass velocity from the intact cold leg side to the broken cold leg side, both of the string probe and the drag disk at 5.625 m from the bottom of pressure vessel should be installed vertically. However, these two instruments were installed horizontally by mistake.

The void fraction measured with the string probe located at 5.625 m from the bottom of pressure vessel decreases rapidly when the Acc injection port is switched from the lower plenum to the intact cold leg. Then, the void fraction rapidly increases up to 0.98 and remains at the same value until the froth level of downcomer reaches the string probe elevation at 500 seconds.

On the other hand, the two string probes located at 0.67 m from the bottom of pressure vessel indicate that the void fractions were higher than 0.5 during the test though the elevation is below the water level during the test. Therefore, these two string probes are not reliable.

3.6 Downcomer Drag Disk

The water velocities at three locations in the downcomer measured with the drag disks are shown in Figs. 3-33 (1) and (2) for Tests S1-20 and S1-24, respectively.

At the elevation of 0.67 m from the bottom of the pressure vessel,

the measured water velocities are compared with the water velocities obtained by the mass balance calculation using the data from conventional instruments. As shown in Fig. 3-33, these two kinds of water velocities are generally not agreed with each other. Only the water velocity measured with the drag disk at the outer side (UD01P92) for Test S1-24 is relatively close to the water velocity obtained by the mass balance calculation at the time after about 50 seconds from the BOCREC.

Since the downcomer drag disk at the elevation of 5.625 m from the bottom of the pressure vessel was not correctly installed as discussed in Section 3.5.2.2, the horizontal water velocity could not be obtained from the drag disk. The measured water velocity is negligibly small except during the first 50 seconds for these two tests.

In Test S1-20, the Acc water was initially injected into the lower plenum and then the injection port was switched to the intact cold leg at 7 seconds after the BOCREC. In Test S1-24, on the other hand, the Acc water was injected into the intact cold leg from the beginning. The Acc injection was switched to the LPCI at 19 and 40 seconds from the BOCREC for Test S1-20 and S1-24, respectively. Therefore, the initial oscillations in the measured water velocities are mainly caused by the Acc injection into the intact cold leg.

The two-phase mass velocities could be calculated by combining the momentum fluxes measured with the drag disks and the fluid densities measured with the adjacent string probes in the downcomer if both instruments worked well. However, the reliable two-phase mass velocities could not be obtained because both of the drag disks and the string probes failed to provide available results as discussed above.

3.7 Video Optical Probe

3.7.1 Transition from Droplet Flow to Churn-Turbulent Flow

Generally, flow patterns could be known with the observation by using Video Optical Probe (VOP). Especially the observation with the VOP between the tie plate and the top grid spacer has a consistency with the differential pressure across the tie plate. In addition the transition from the droplets flow to the churn-turbulent flow at the top grid spacer holes could be known by using the VOP. Flow pattern map for a vertical flow by Hewitt and Roberts[8] shows the upper boundary of bubbly or churn-turbulent flow as follows:

$$\rho_g U_g^2 \approx 100 \ (kg/s^2m) \quad . \qquad (3\text{-}3)$$

The VOP observation indicated that the flow pattern of two-phase jet from the top grid spacer changed to churn-turbulent flow at the following condition, here the superficial velocity U_g was obtained by the mass balance calculation.

$$\begin{aligned} \rho_g U_g^2 &\doteqdot 134 \ (kg/s^2m) \ \text{(for test S1-SH2)} \\ \rho_g U_g^2 &\doteqdot 139 \ (kg/s^2m) \ \text{(for test S1-01)} \\ \rho_g U_g^2 &\doteqdot 111 \ (kg/s^2m) \ \text{(for test S1-02)} \end{aligned} \qquad (3\text{-}4)$$

The relatively good agreement between Eqs. (3-3) and (3-4) suggests that the transition from the droplet flow to the churn-turbulent flow at the top grid spacer holes can be described well by Eq. (3-3).

3.7.2 Observation Results

The followings are the examples of observation results for Tests S1-SH2, S1-01 and S1-02.

(1) Test S1-SH2 (high pressure test)

i) Between the tie plate and the top grid spacer

0 sec. - (steam condition)

105 sec. - Some droplets fall from the tie plate.

114 sec. - Droplets up-flow can be seen.

185 sec. - Churn-turbulent flow can be seen.

300 sec. - Bubbly flow can be seen.

ii) Upper plenum

0 sec. - (steam condition)

117 sec. - Droplets impinge on the window of the VOP. Soon water film on the window moves to the lower left (toward the hot leg).

324 sec. - Violent two-phase flow is moving down. It seems to be slug flow.

(2) Test S1-01 (base case test)

i) Between the tie plate and the top grid spacer

0 sec. - (Steam condition. Some droplets fall from the tie plate)

112 sec. - Droplets flow can be seen.

120 sec.-- Flow becomes violent.

240 sec. - Churn-turbulent flow.

320 sec. - Slug flow.

ii) Upper plenum

0 sec. - (Steam condition)

110 sec. - Water film on the VOP window is rising up leftwards to the hot leg. It gradually becomes violent.

274 sec. - The water film on the VOP window is falling down left to the hot leg.

390 sec. - Large lumps of water are falling.

(3) Test S1-02 (low pressure test)

i) Between the tie-plate and the top grid spacer

0 sec. - (Steam condition)

110 sec. - Droplets flow.

300 sec. - Churn-turbulent flow.

360 sec. - Slug flow.

ii) Upper pelnum

0 sec. - (Steam condition)

110 sec. - Droplets impinge on the window.

215 sec. - Violent two-phase flow with random orientation.

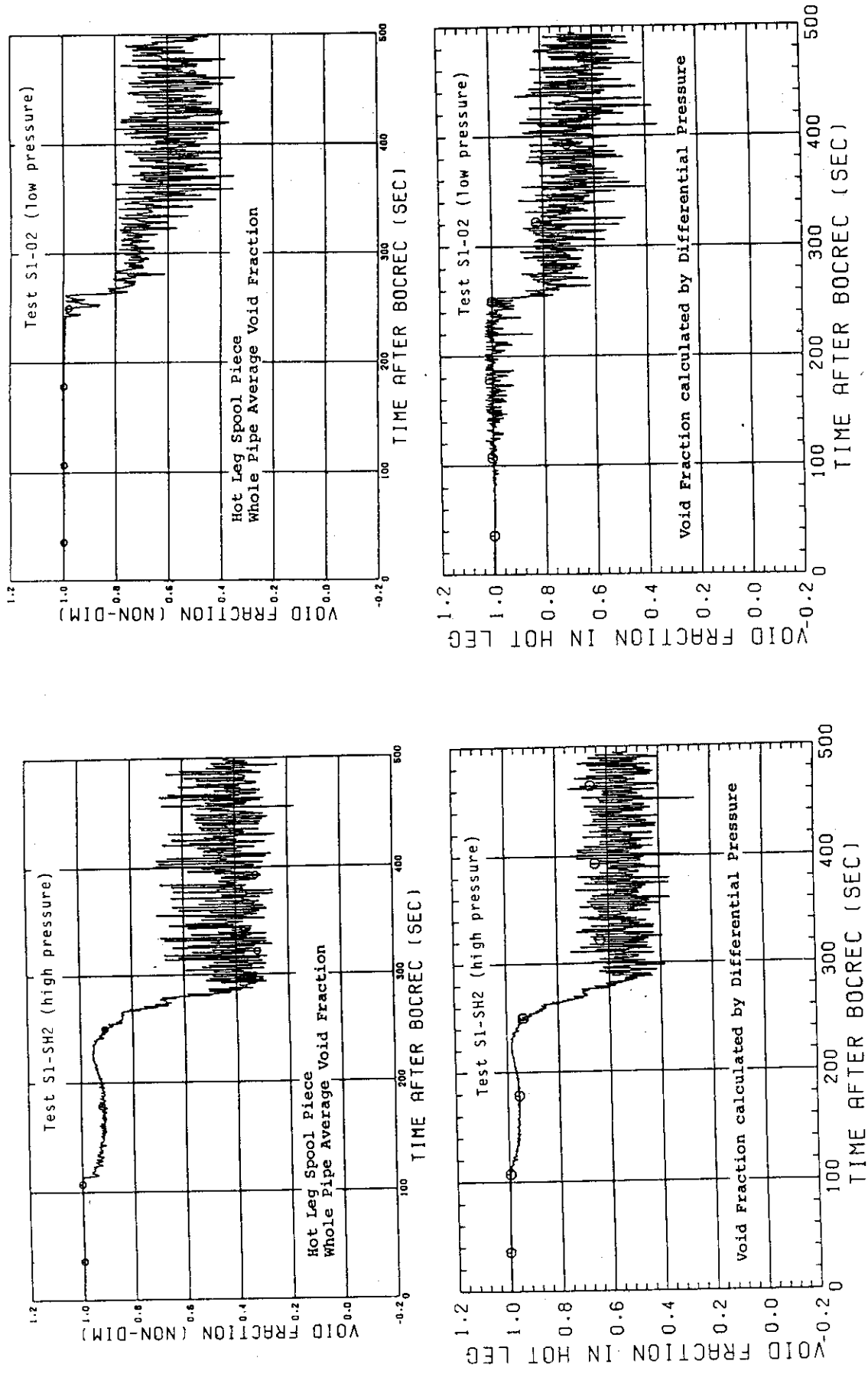

Fig. 3-1 Comparison between whole pipe averaged void fraction measured with hot leg spool piece and void fraction calculated from vertical differential pressure

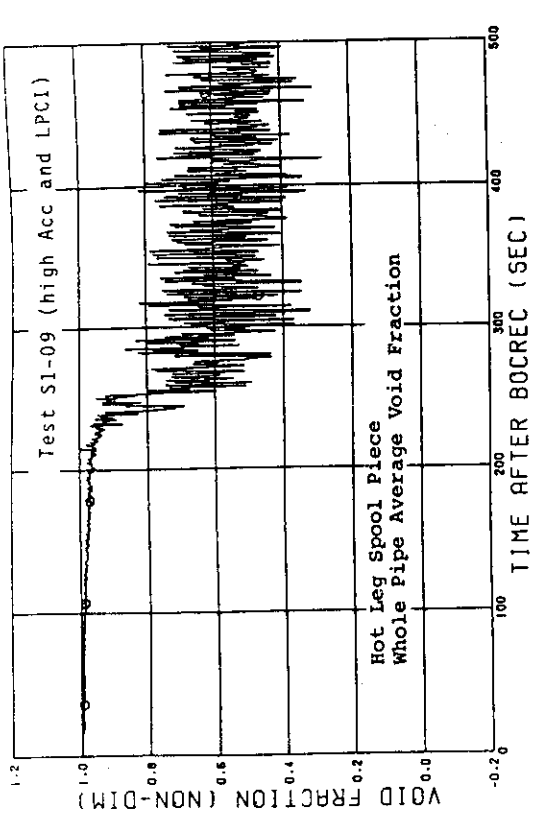

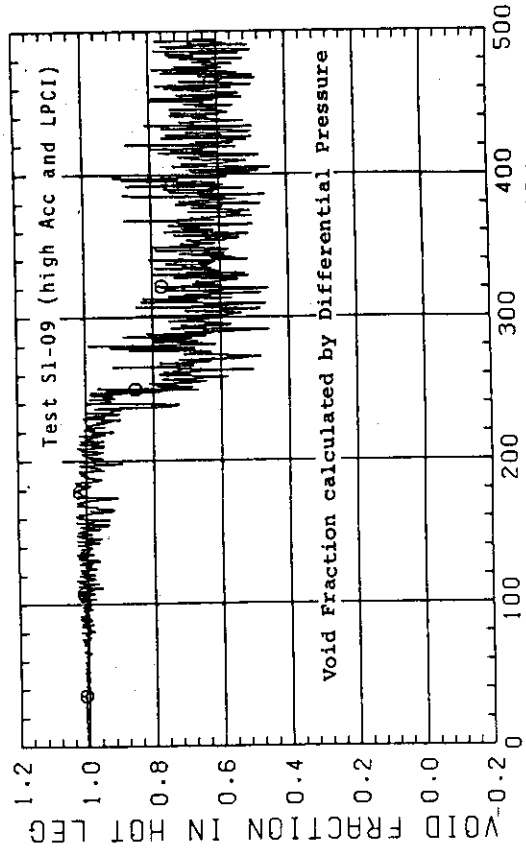

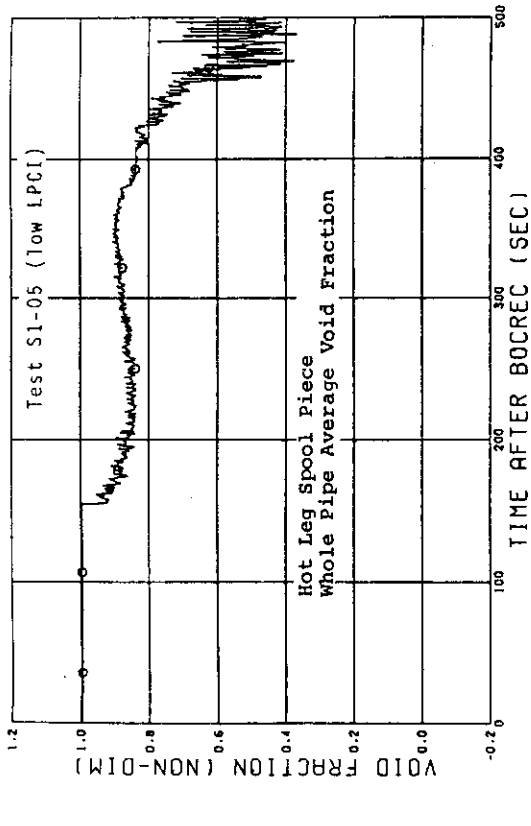

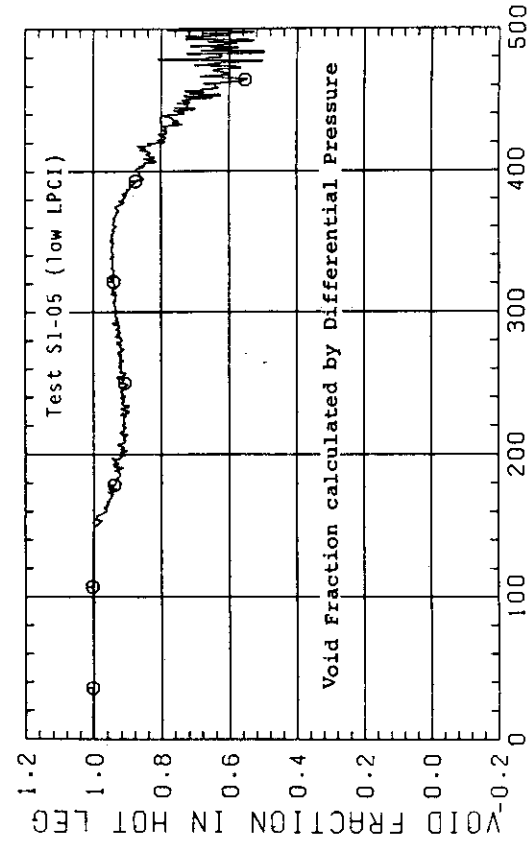

Fig. 3-1 (continue)

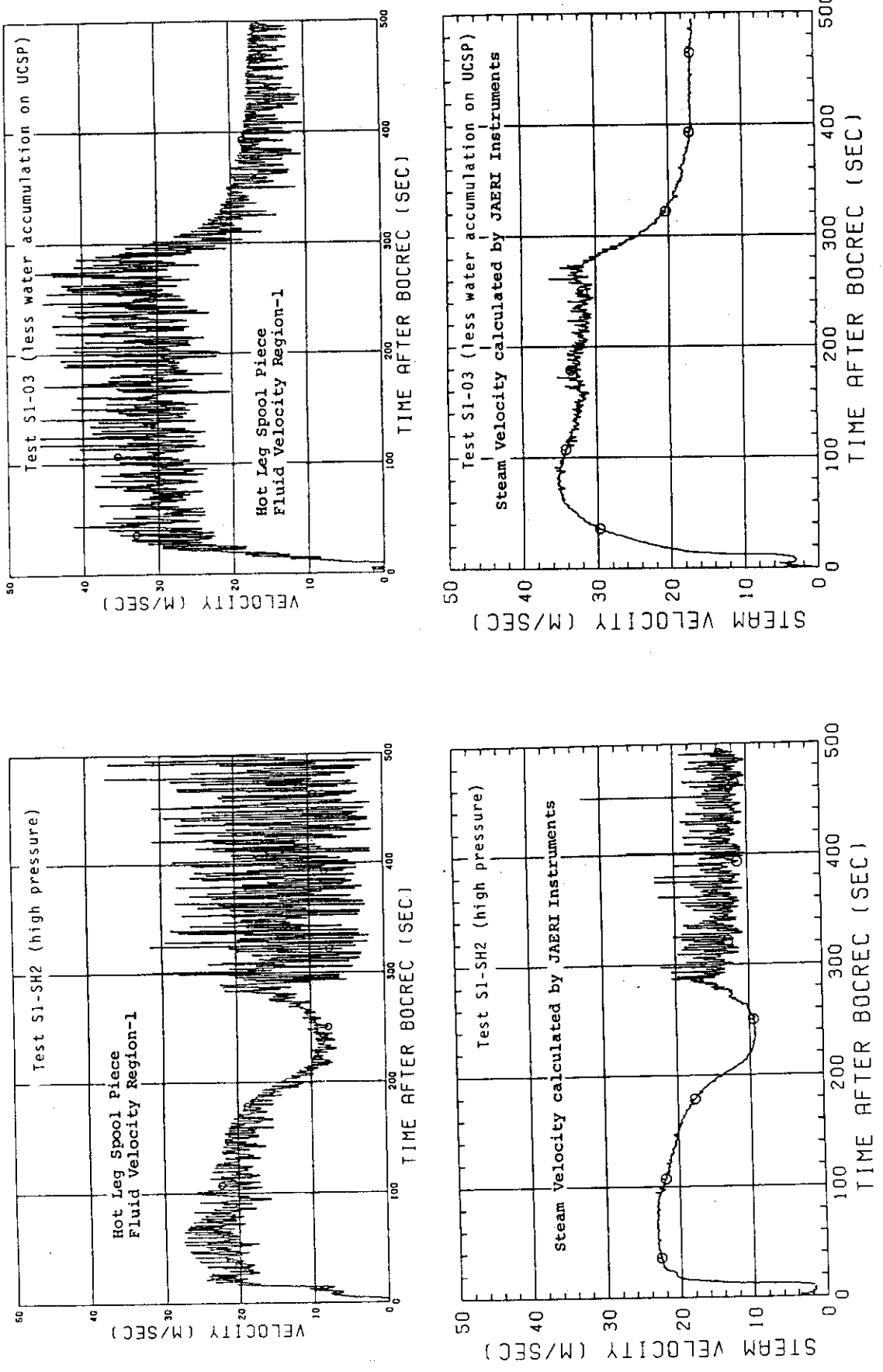

Fig. 3-2 Comparison between fluid velocity measured with hot leg spool piece and hot leg steam velocity calculated from conventional instrumentation data

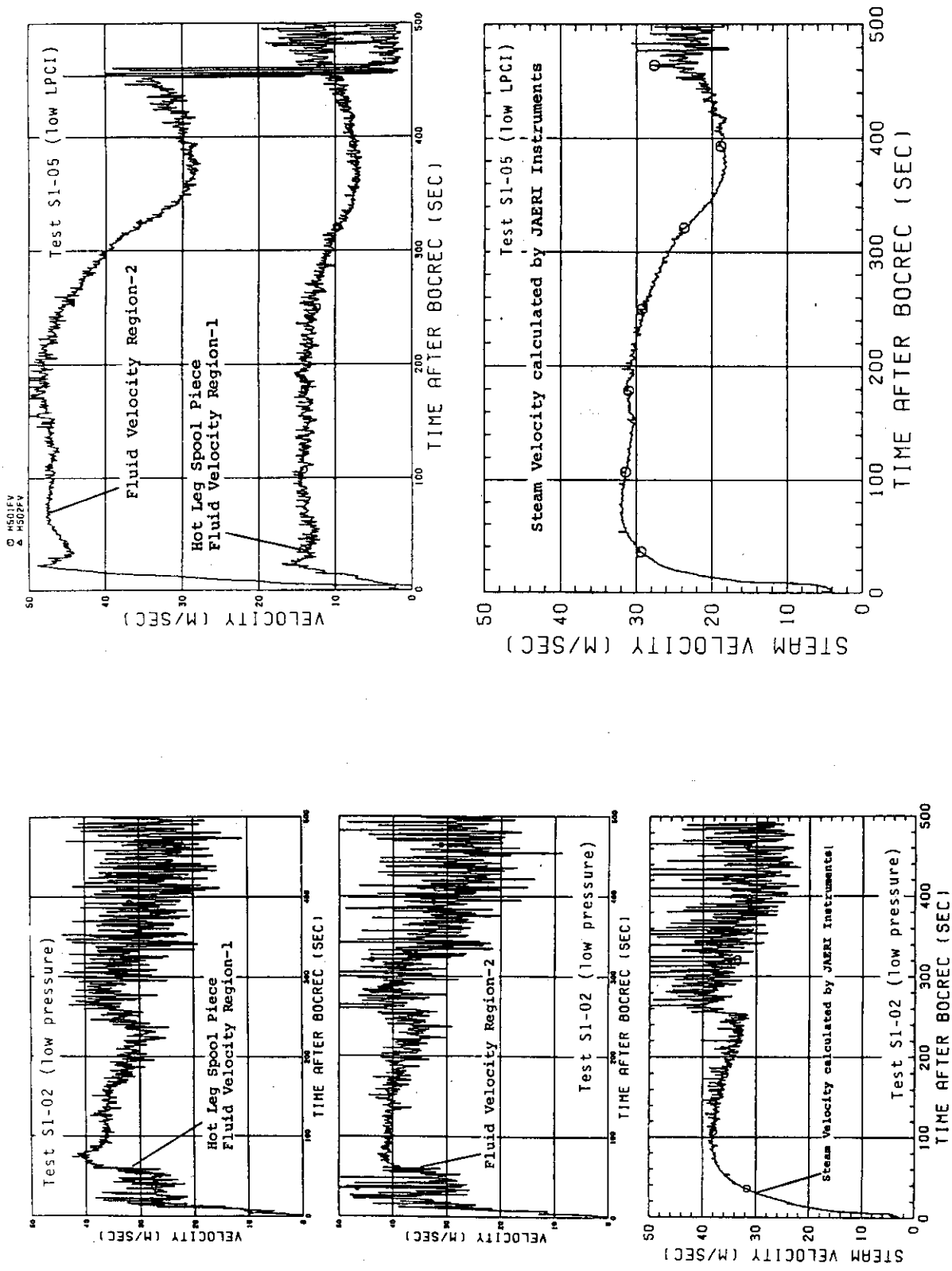

Fig. 3-2 (continue)

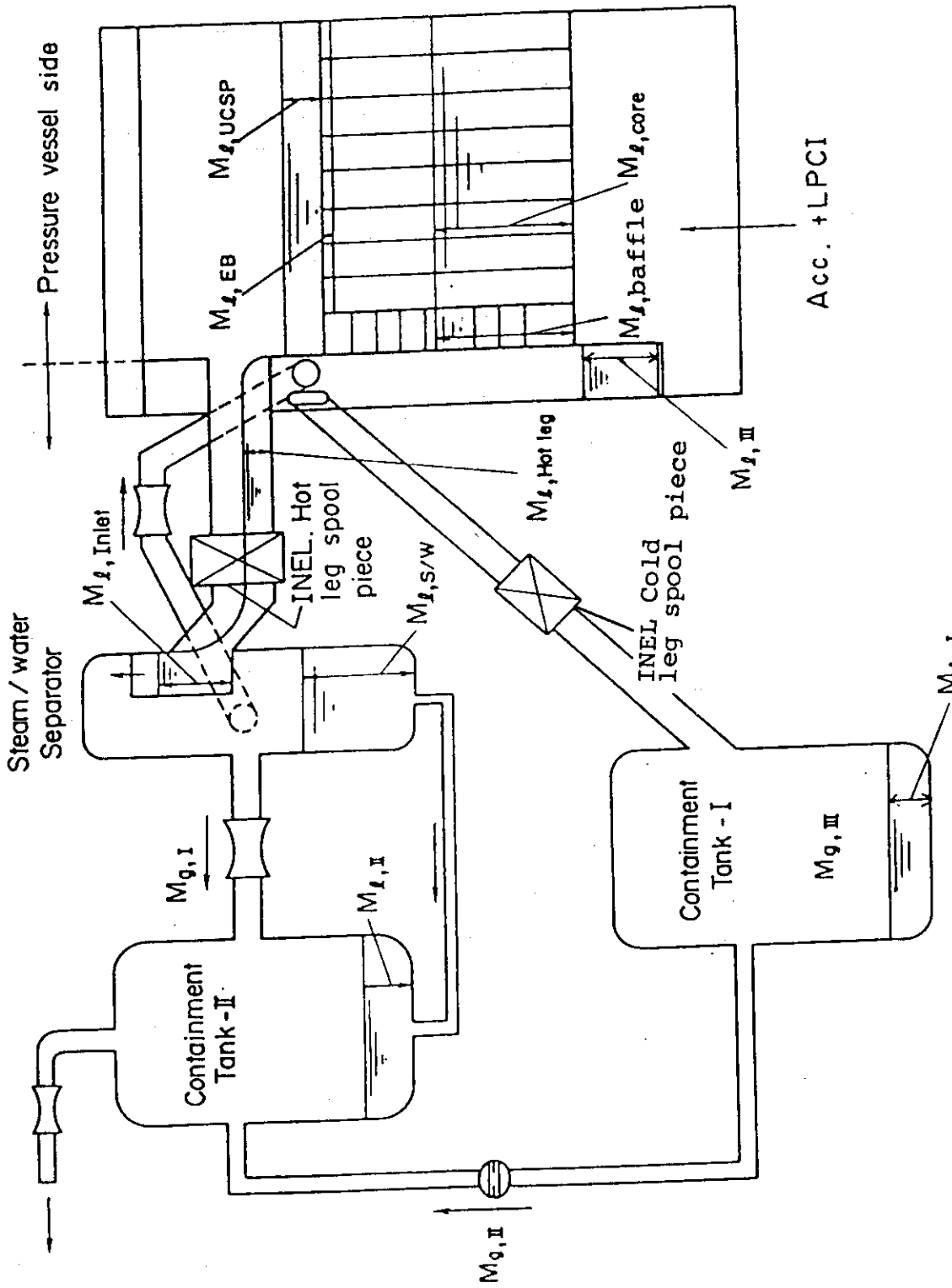

Fig. 3-3 Model and definition of variables for mass balance calculation

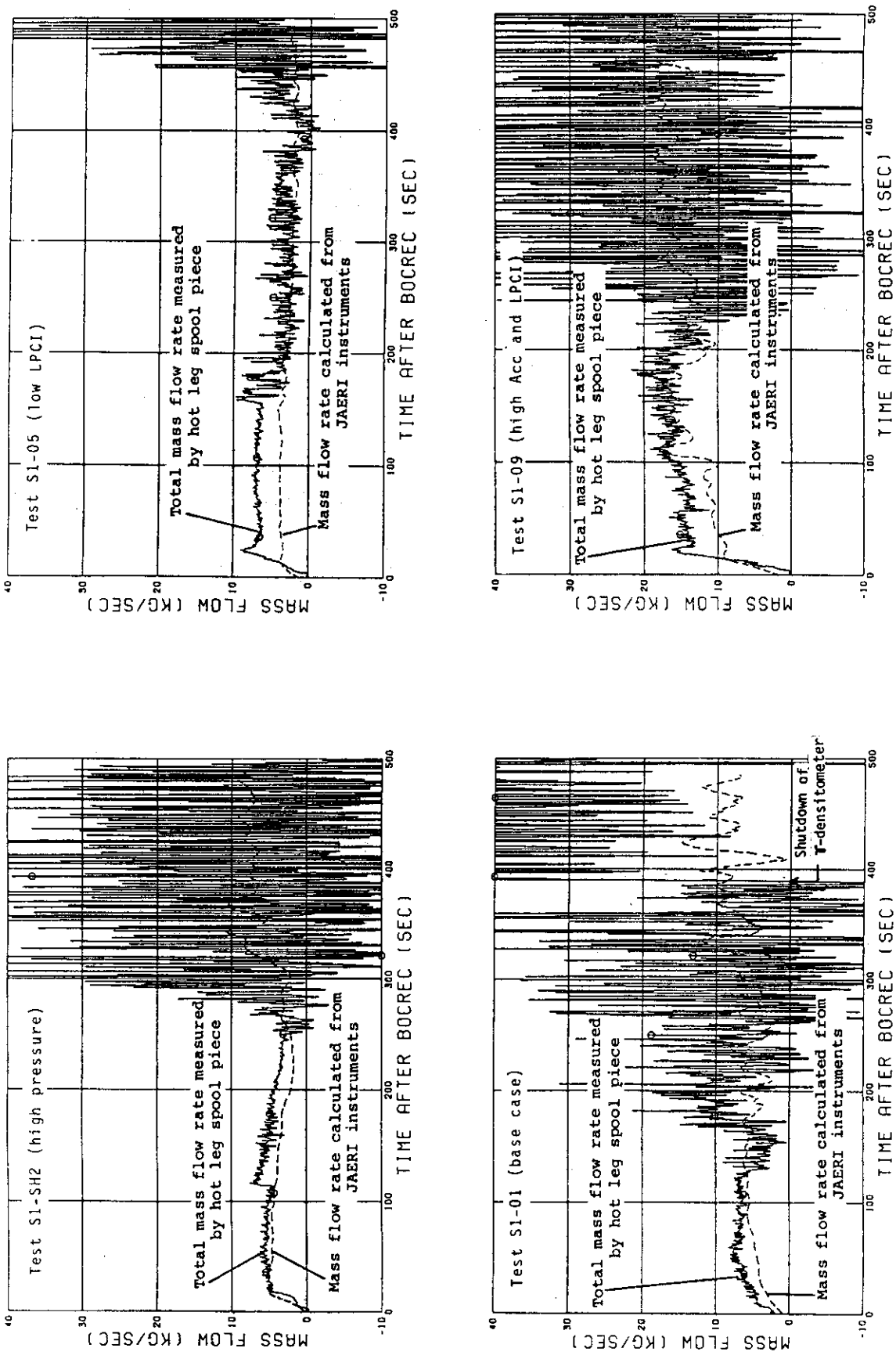

Fig. 3-4 Comparison between total mass flow rate measured with hot leg spool piece and hot leg mass flow rate calculated from conventional instrumentation data

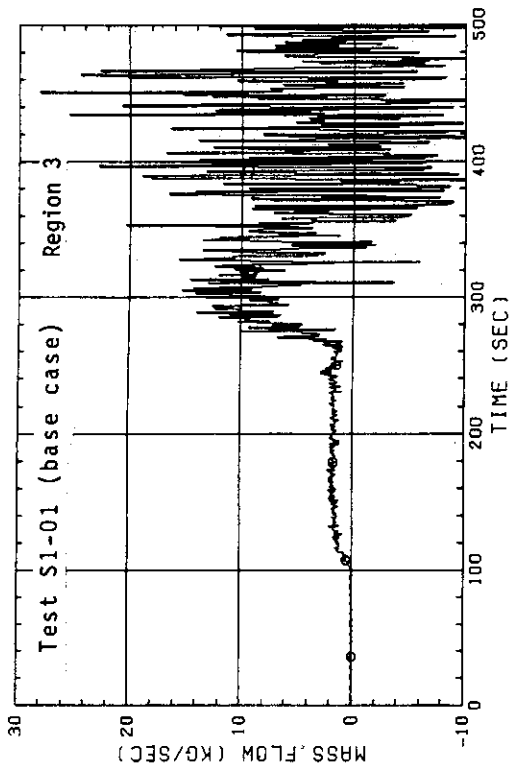

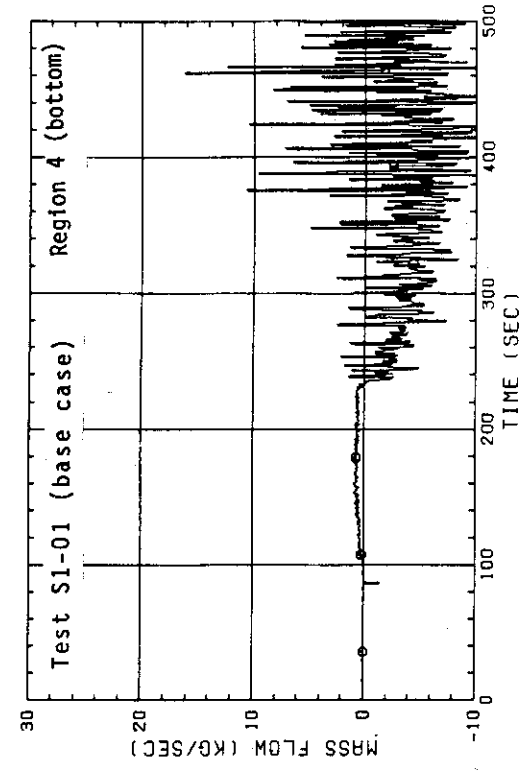

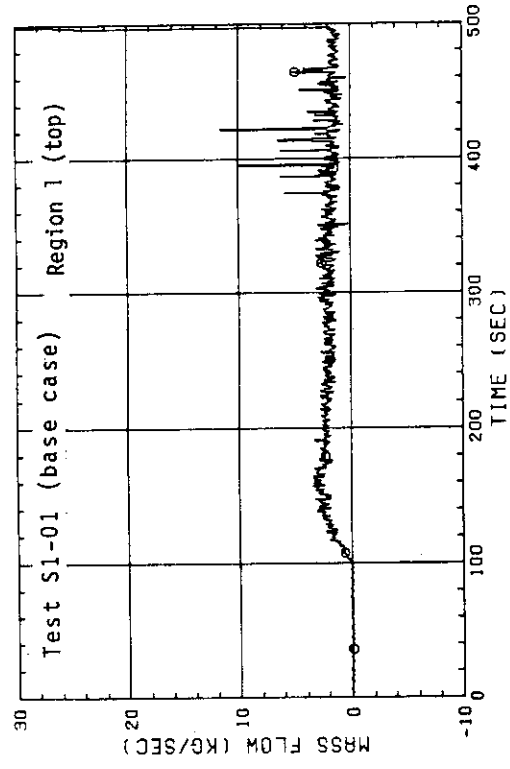

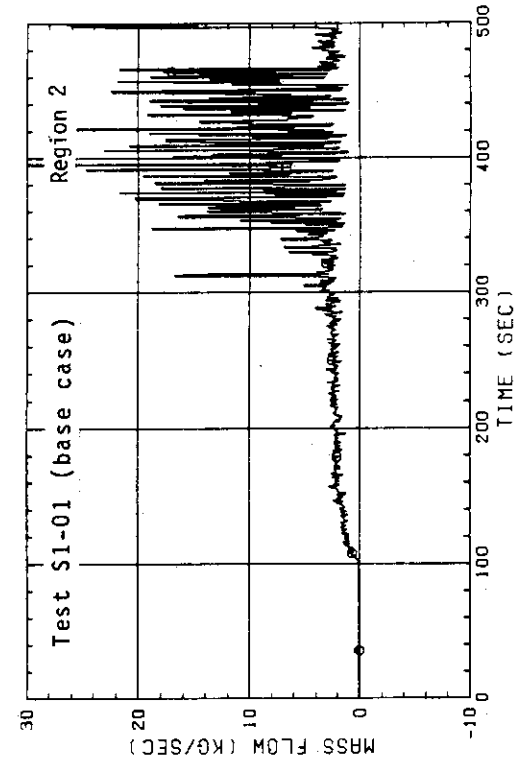

Fig. 3-5 Mass flow rates in four regions of hot leg spool piece

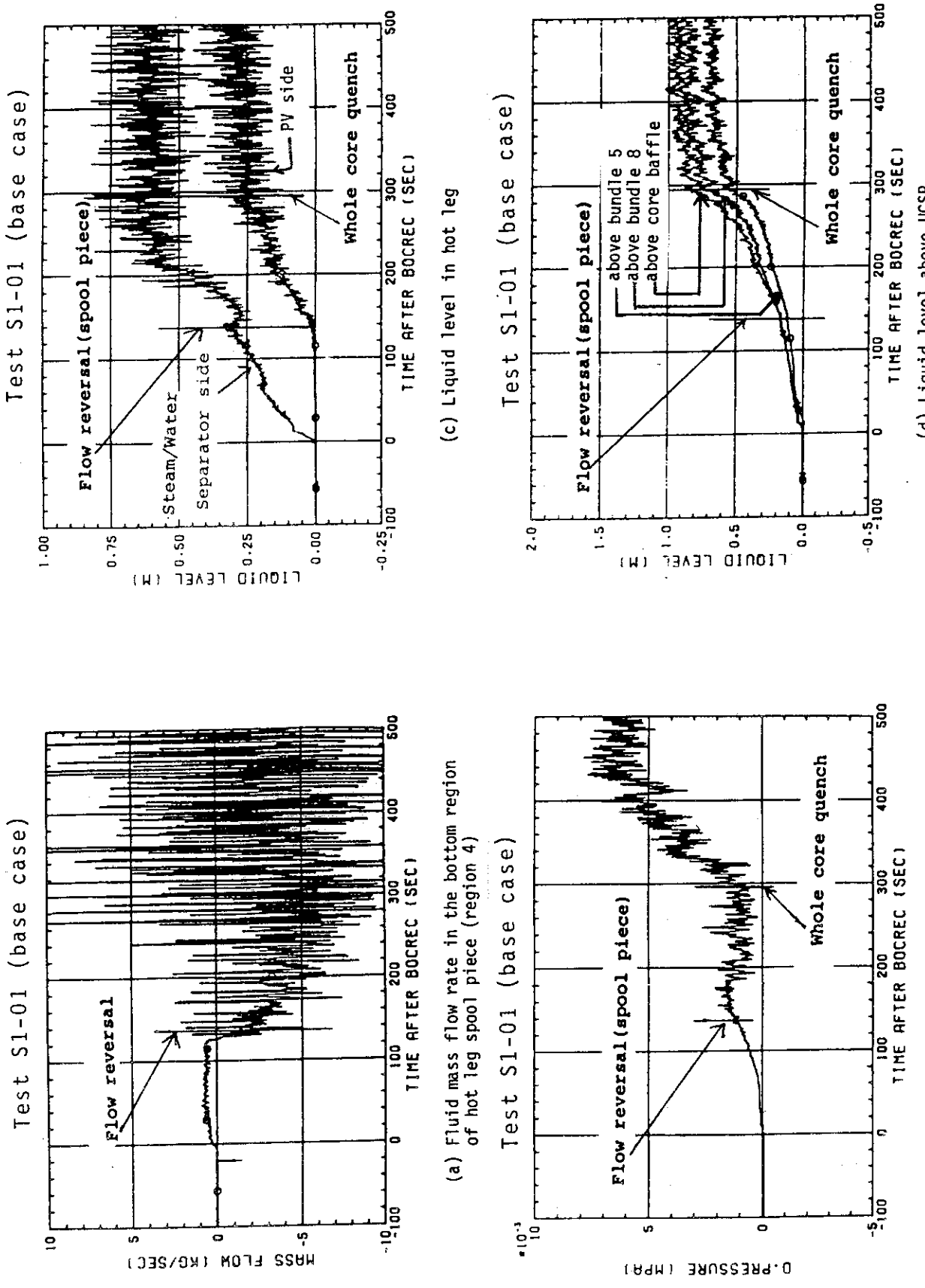

(a) Fluid mass flow rate in the bottom region of hot leg spool piece (region 4)

(b) Differential pressure across steam/water separator inlet plenum simulator

(c) Liquid level in hot leg

(d) Liquid level above UCSP

Fig. 3-6 Evidences of hot leg flow reversal observed in conventional instrumentation data.

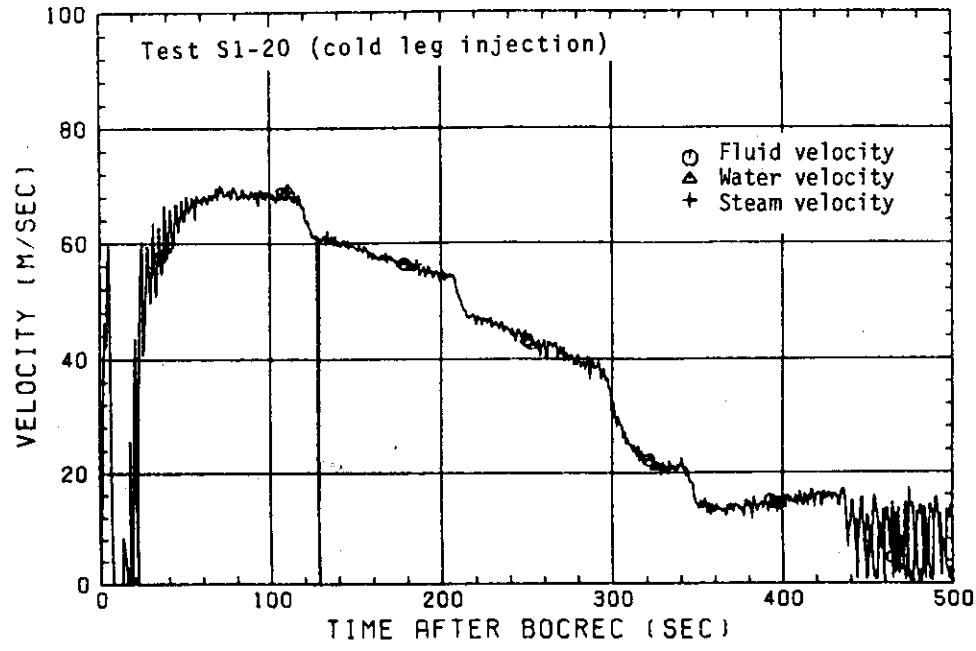

Fig. 3-7 Fluid, water and steam velocities measured with cold leg spool piece

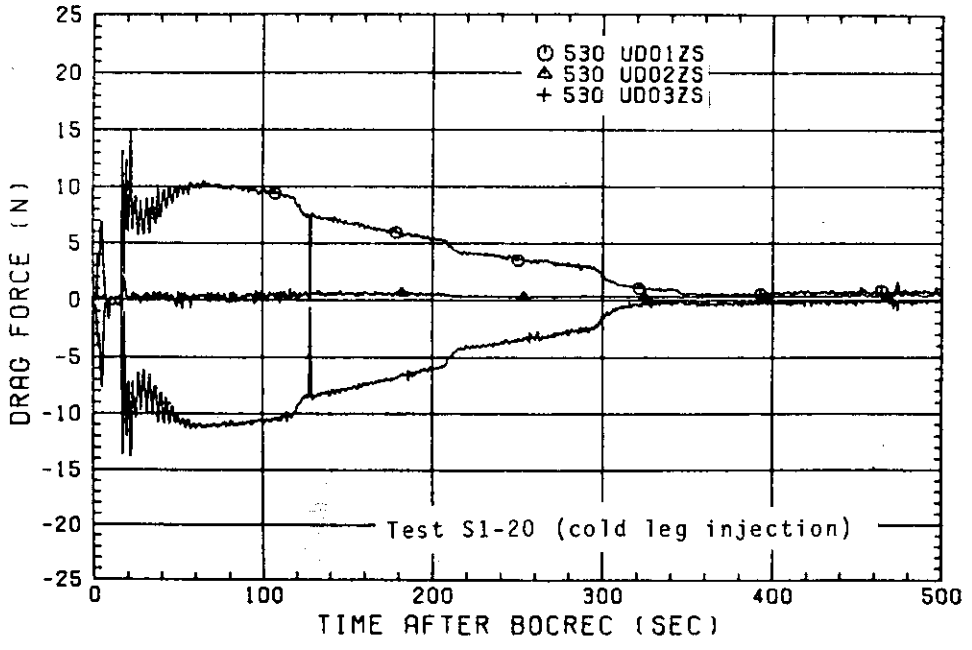

Fig. 3-8 Drag forces measured with drag screen transducers in cold leg spool piece

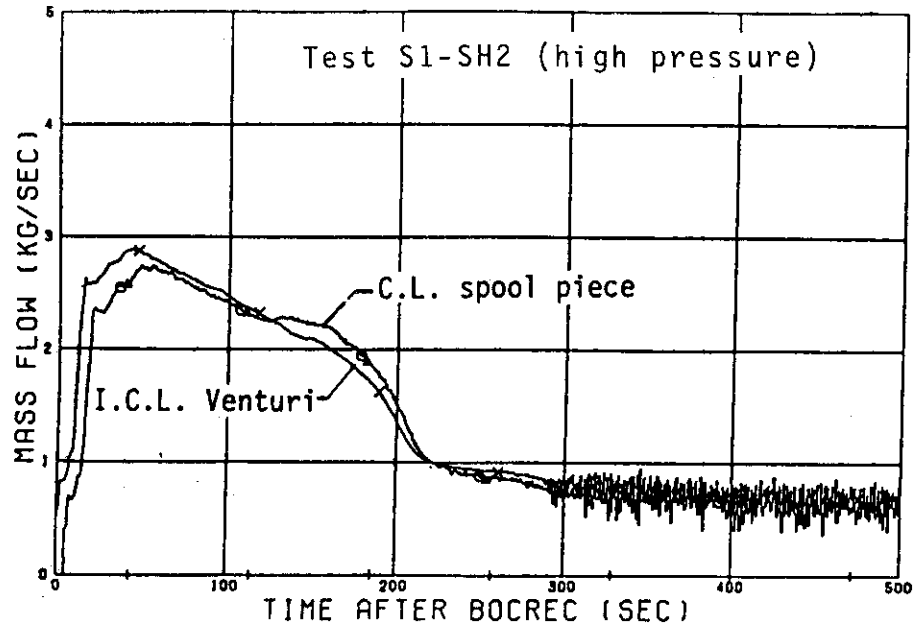

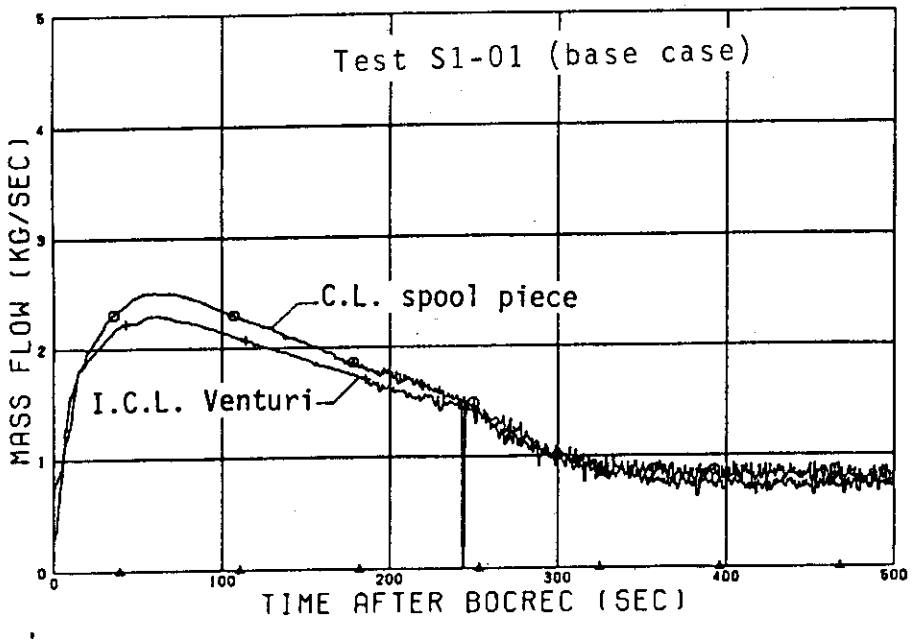

Fig. 3-9 Comparison between mass flow rate measured with cold leg spool piece and steam mass flow rate measured with Venturi at intact cold leg for forced flooding tests

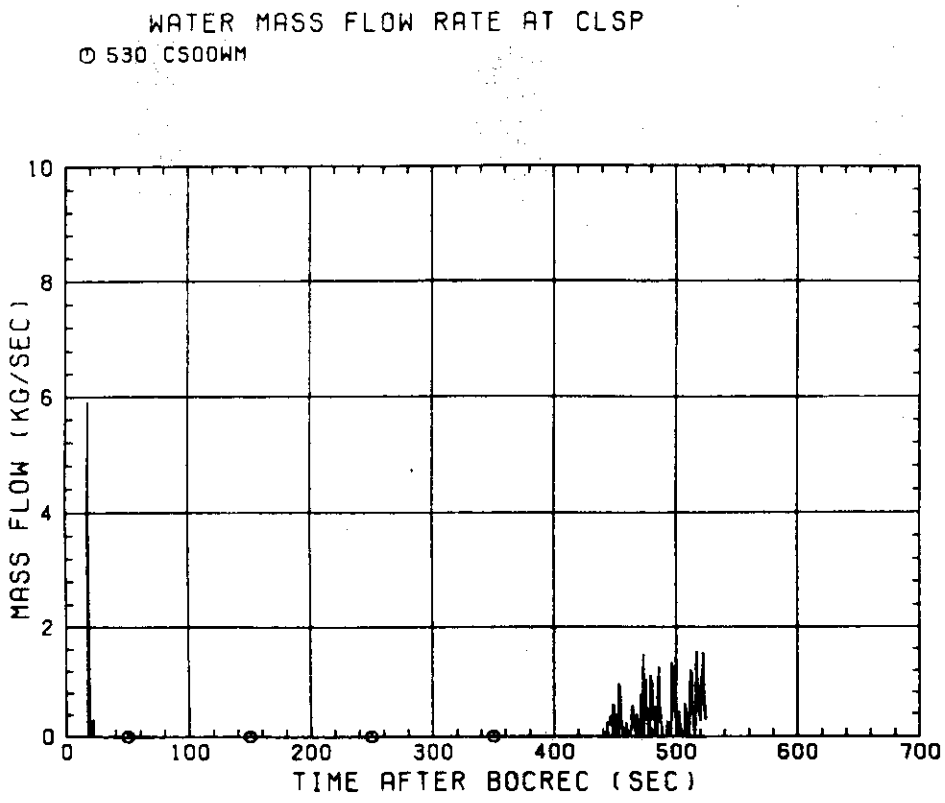

Fig. 3-10 Water mass flow rate measured with cold leg spool piece for cold leg injection test

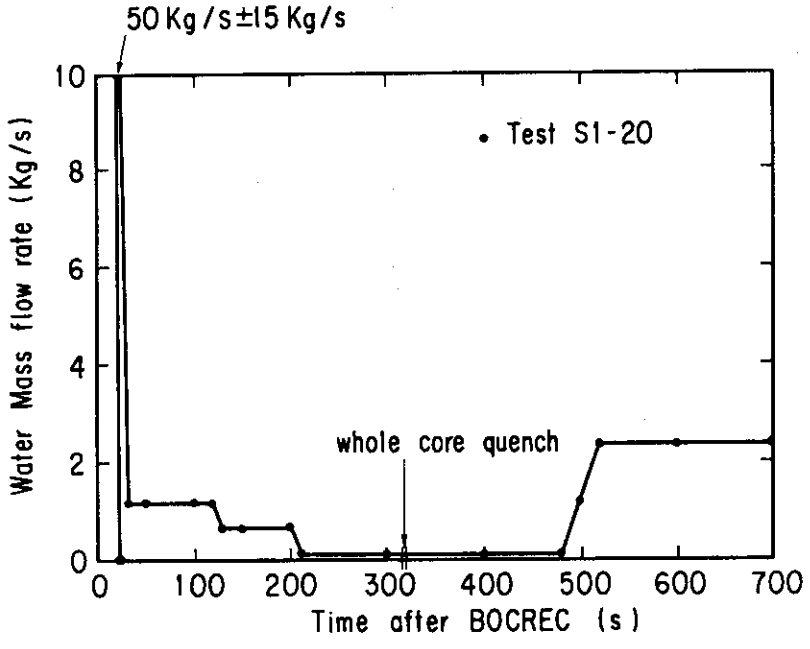

Fig. 3-11 Bypass water mass flow rate measured by liquid level transient in containment tank-I

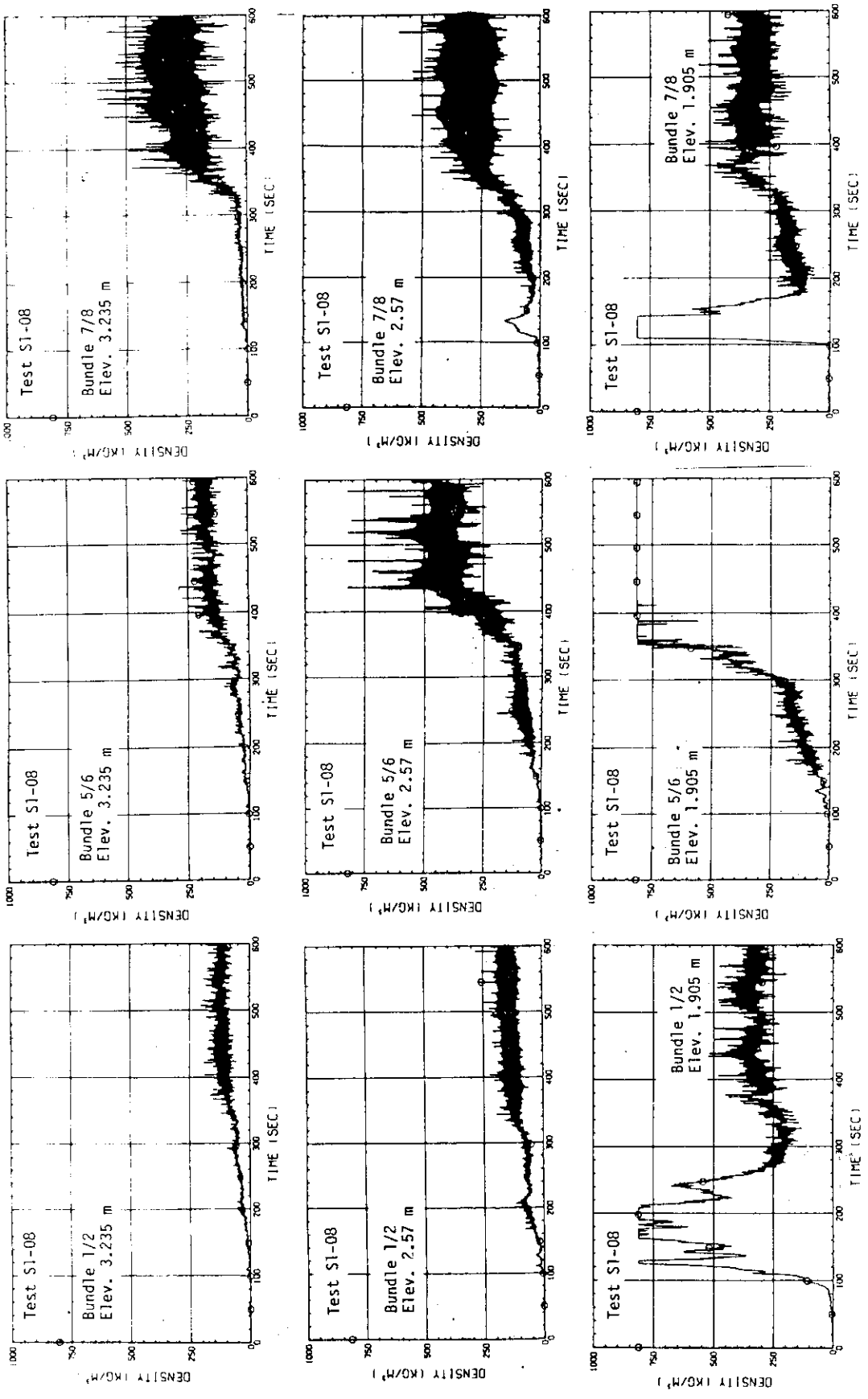

Fig. 3-12 Fluid densities in core measured with γ-densitometer

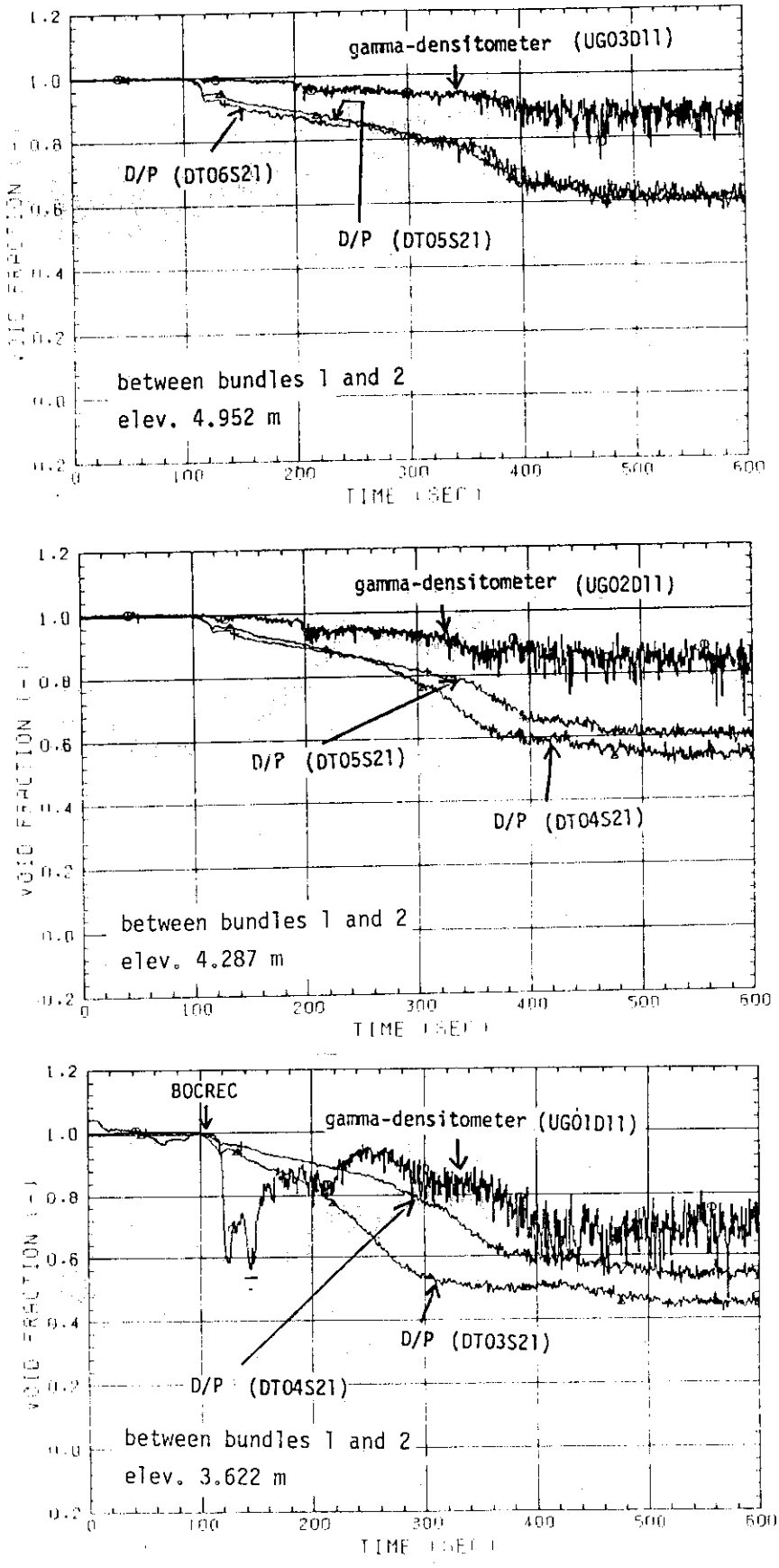

Fig. 3-13 Comparison between void fractions measured with γ-densitometers and void fractions calculated from vertical differential pressures

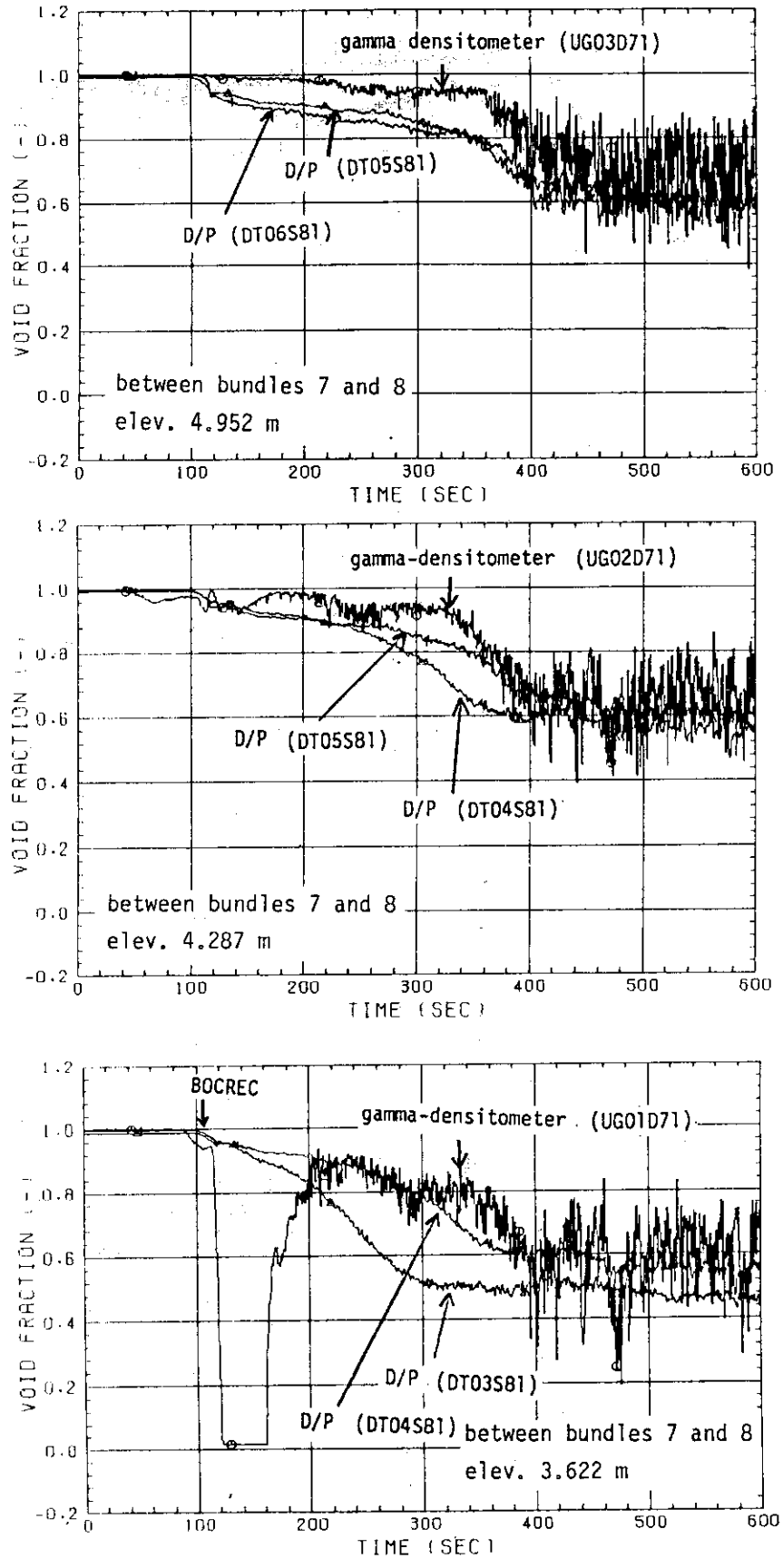

Fig. 3-13 (continue)

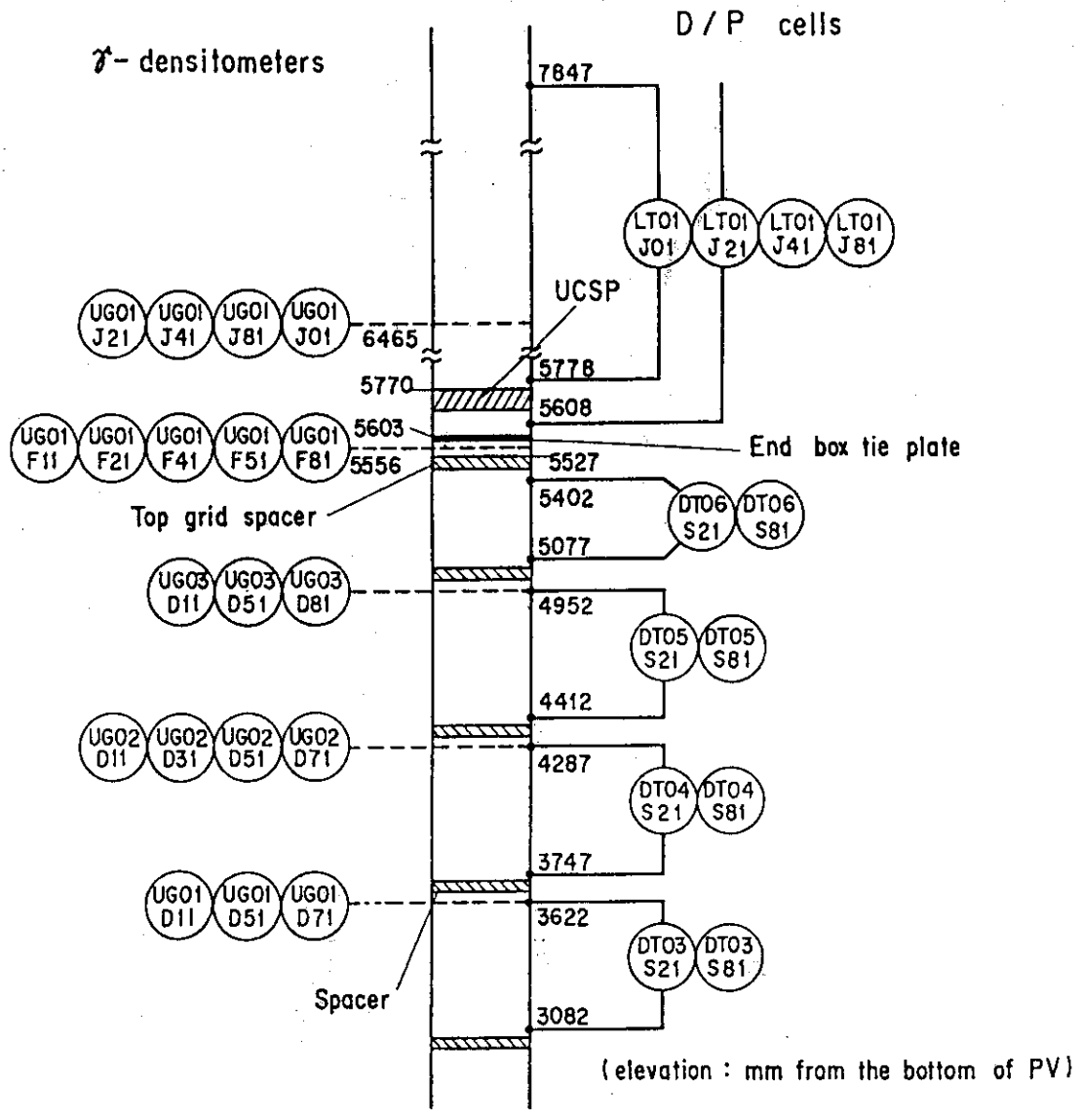

Fig. 3-14 Measurement locations of γ-densitometers, in-core vertical differential pressures and upper plenum liquid levels

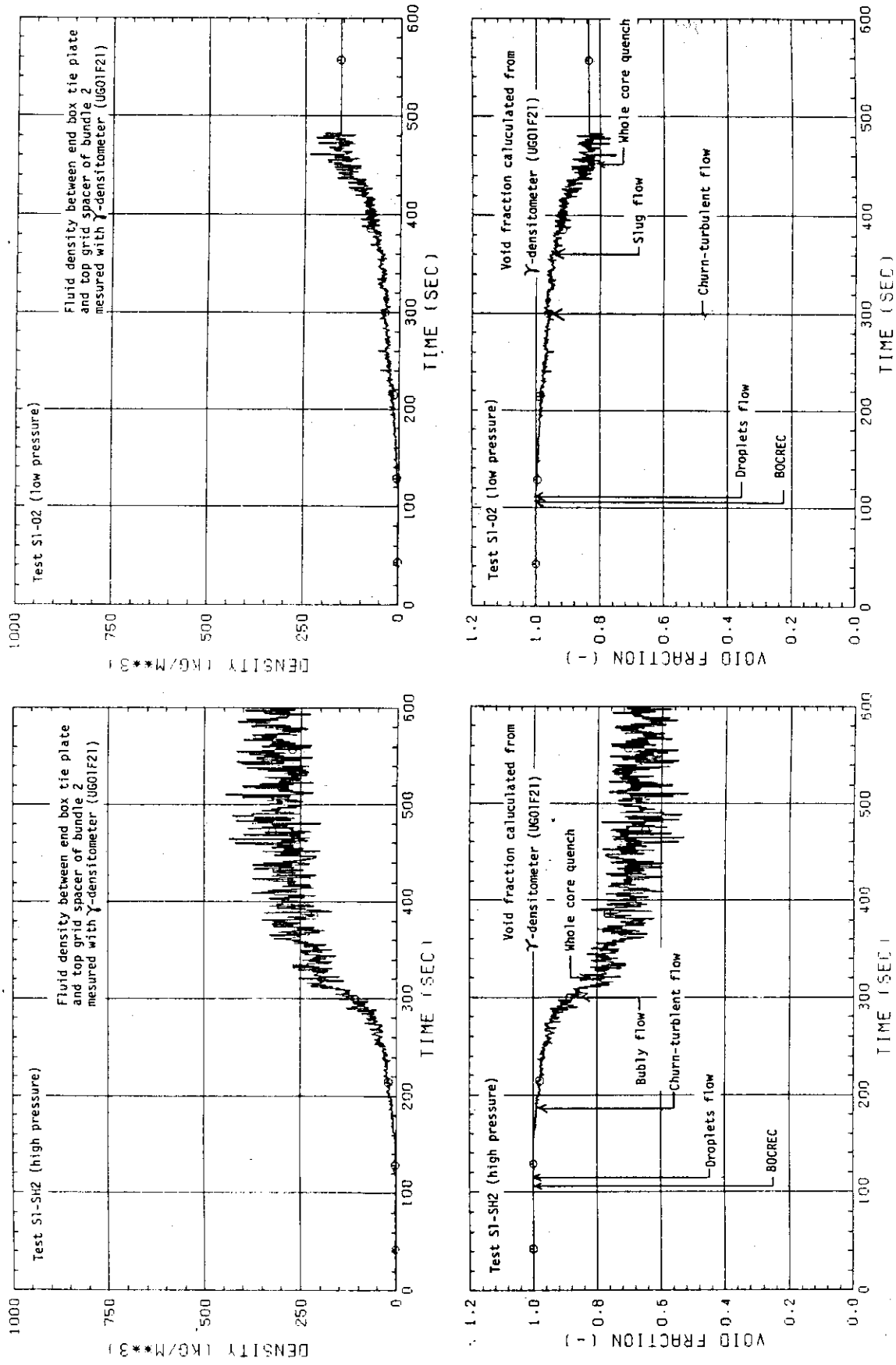

Fig. 3-15 Fluid densities below end box tie plate

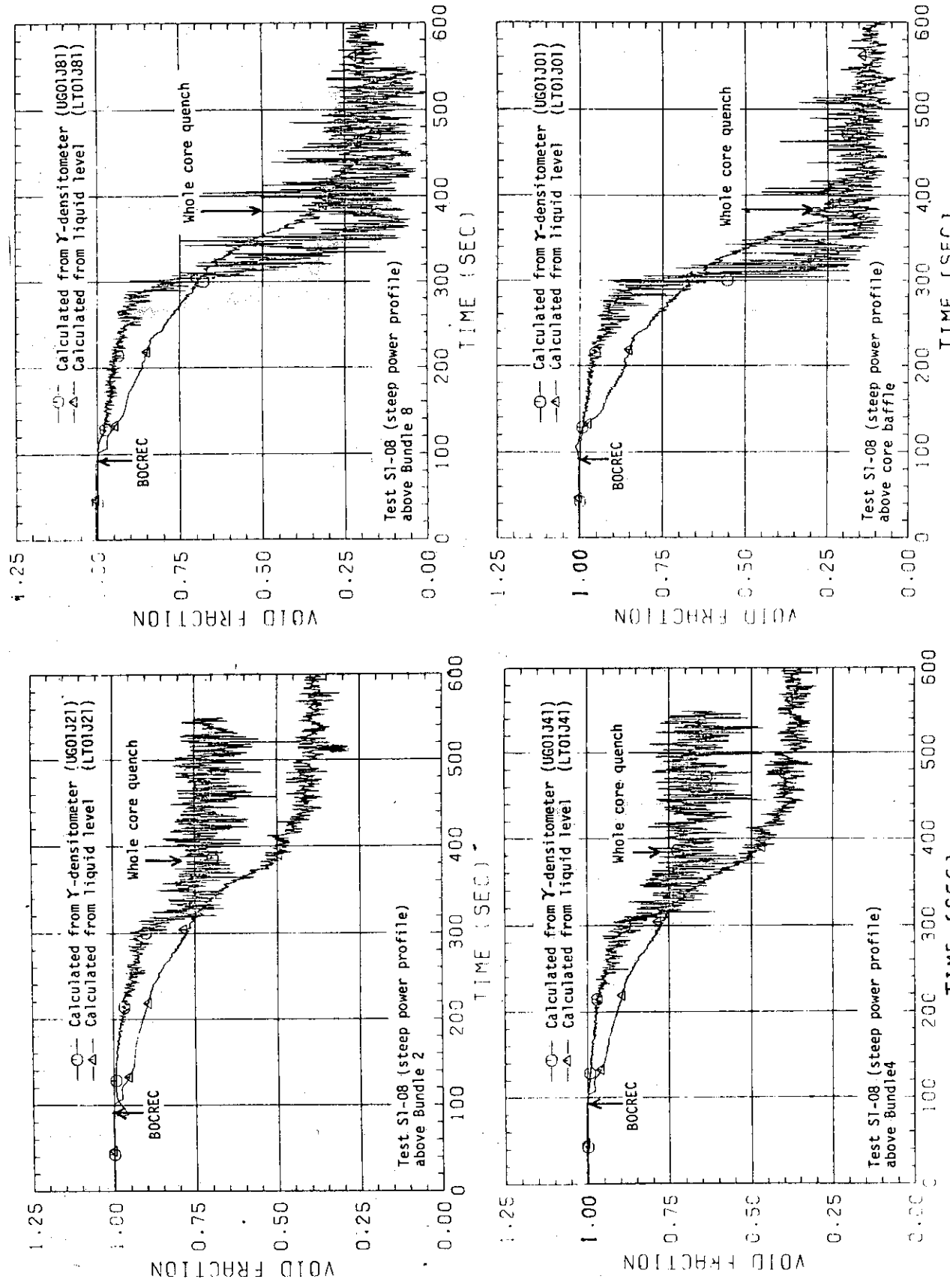

Fig. 3-16 Comparison between fluid densities and liquid levels in upper plenum

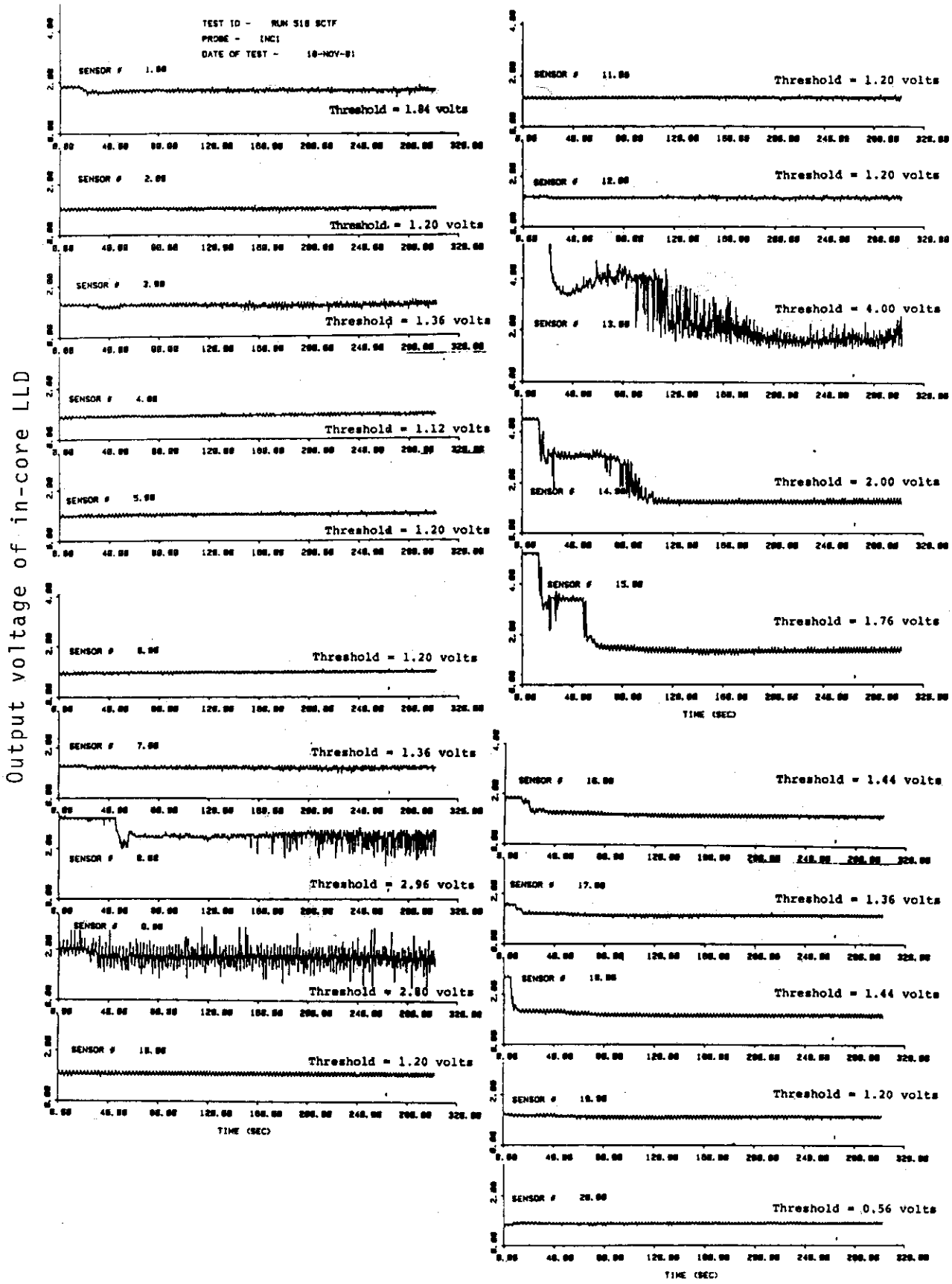

Fig. 3-17 Transients of output signals of in-core LLD at bundle 2 in Test S1-10

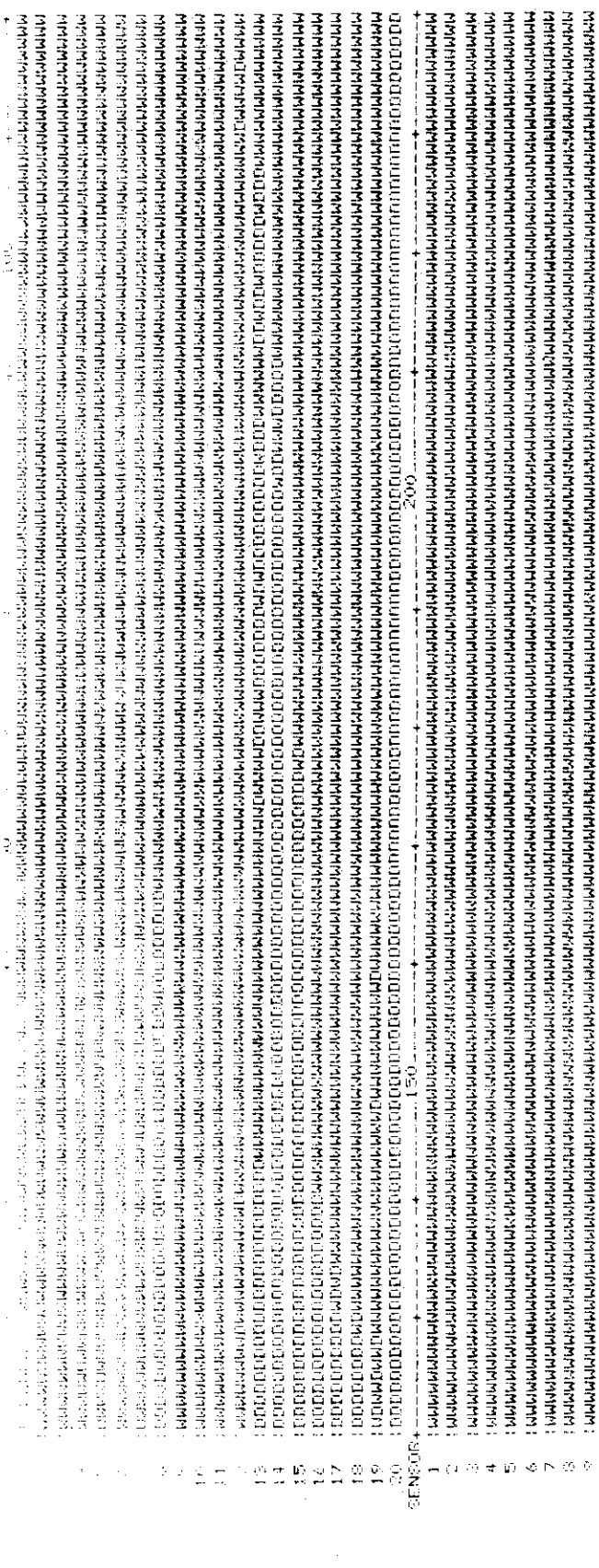

Fig. 3-18 Bubble plots for in-core LLD at bundle 2 in Test S1-10

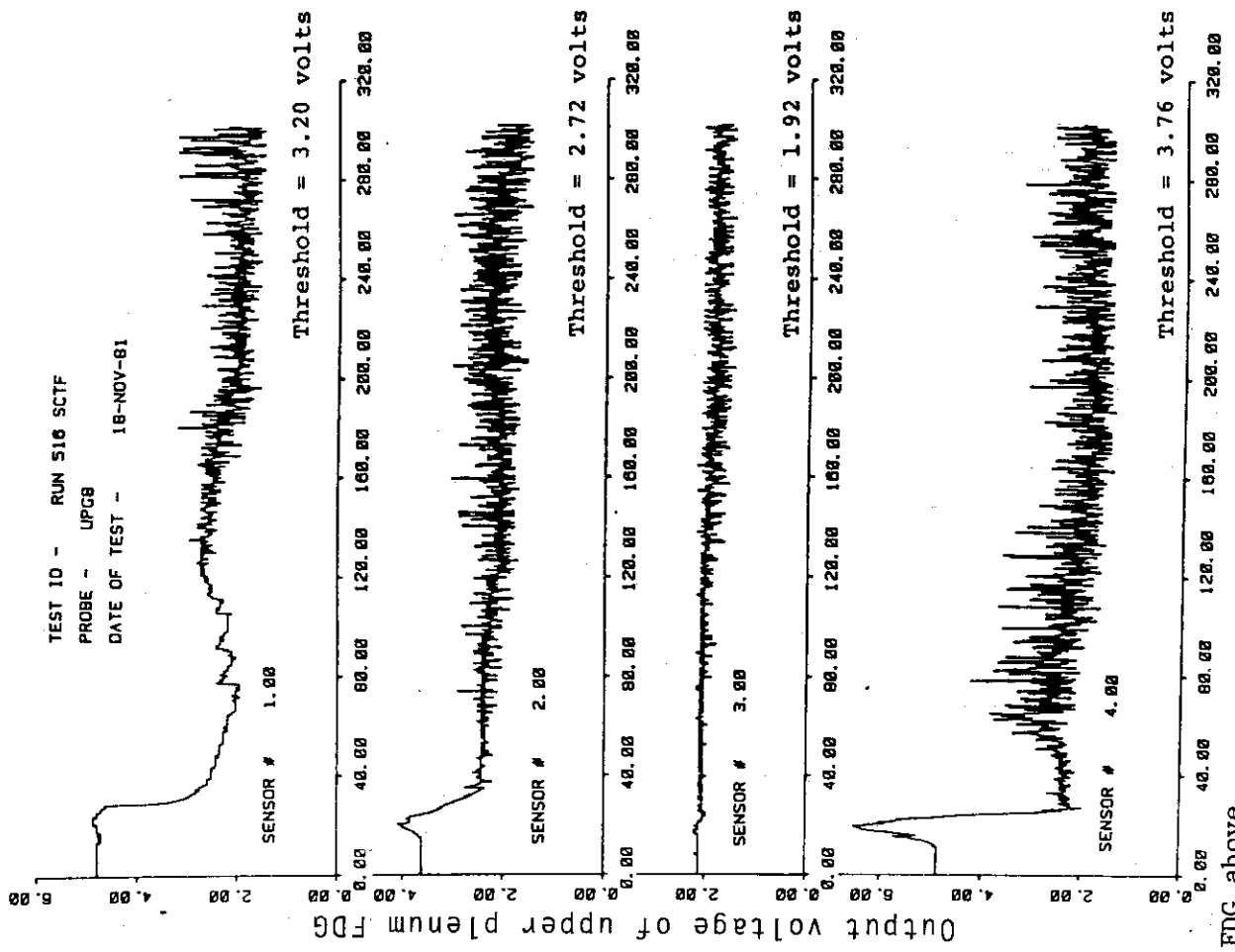

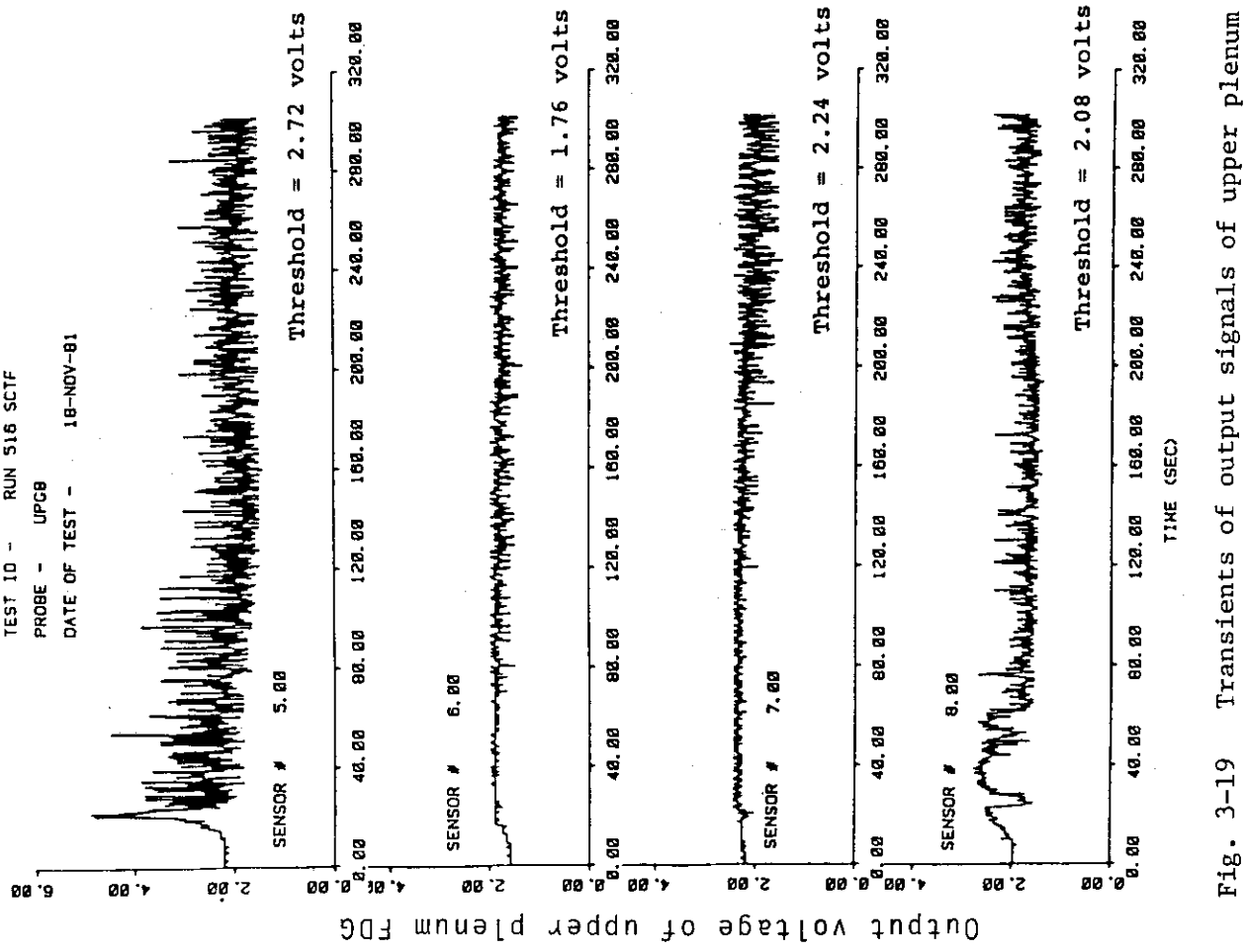

Fig. 3-19 Transients of output signals of upper plenum FDG above bundle 8 in Test S1-10

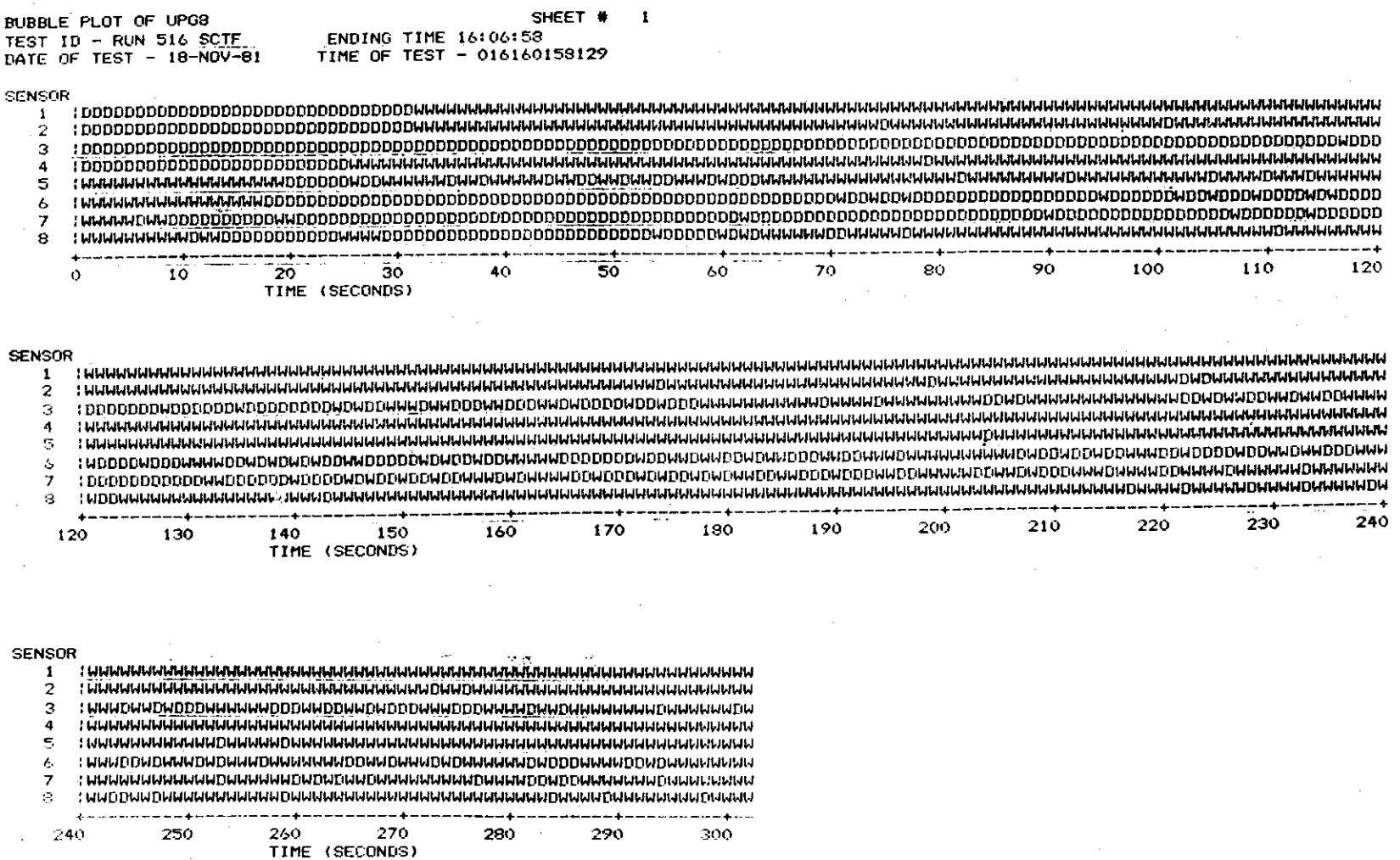

Fig. 3-20 Bubble plots for upper plenum FDG above bundle 8 in Test S1-10

JAERI-M 84-065

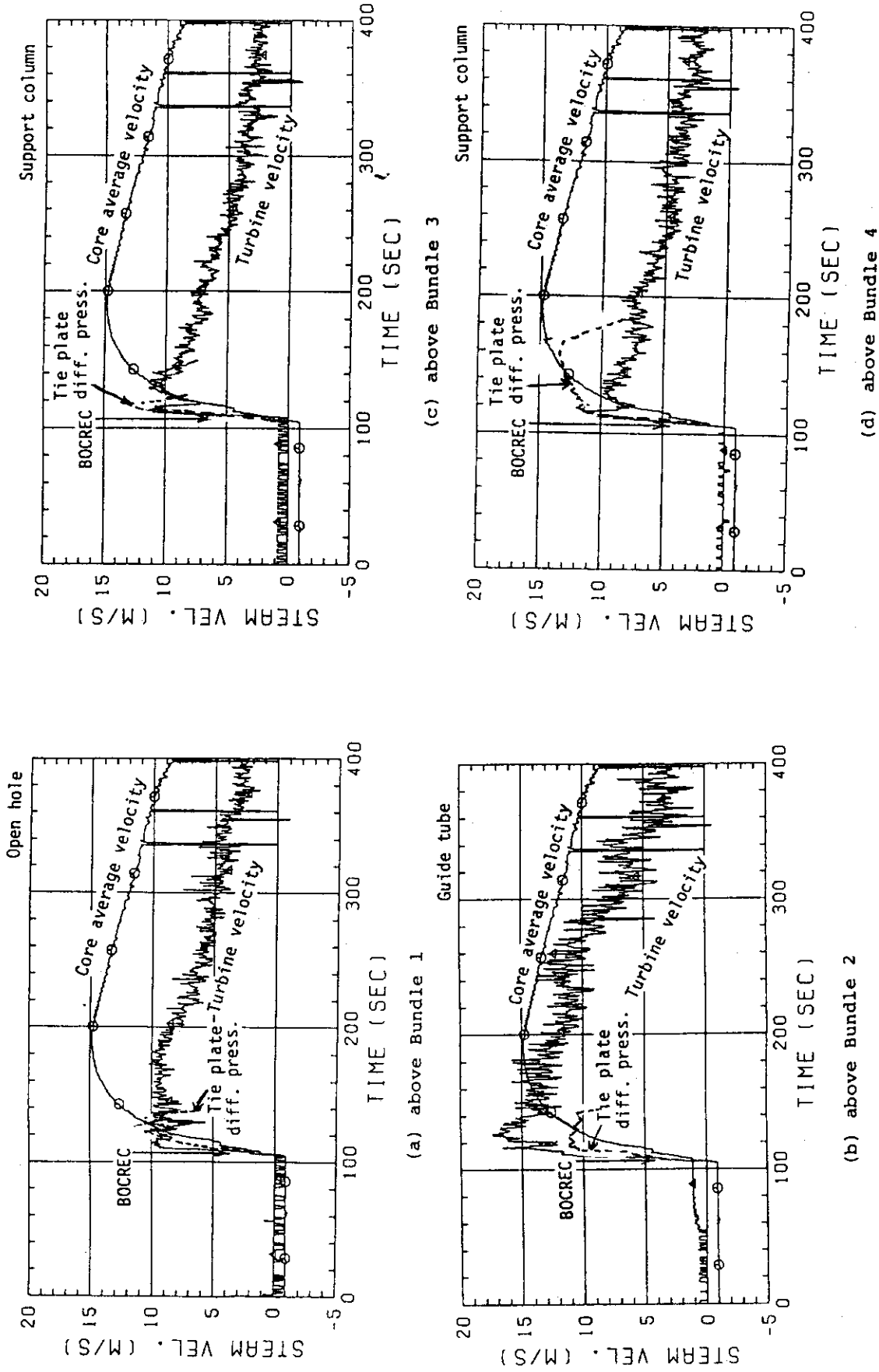

Fig. 3-21 Comparison between steam velocities measured with UCSP turbine meters, average steam velocity obtained with mass-balance calculation and steam velocity estimated with Bernoulli theorem

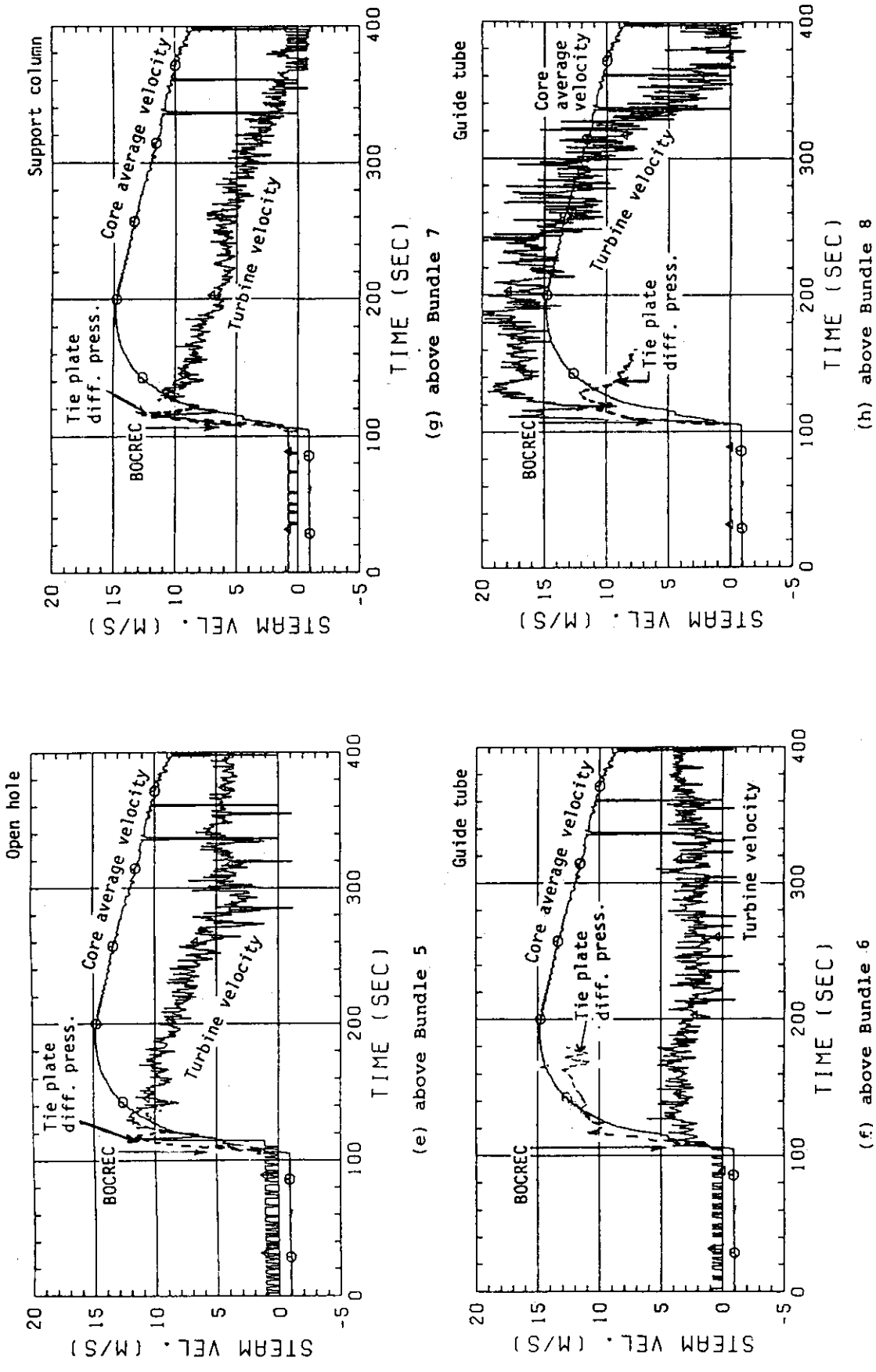

Fig. 3-21 (continue)

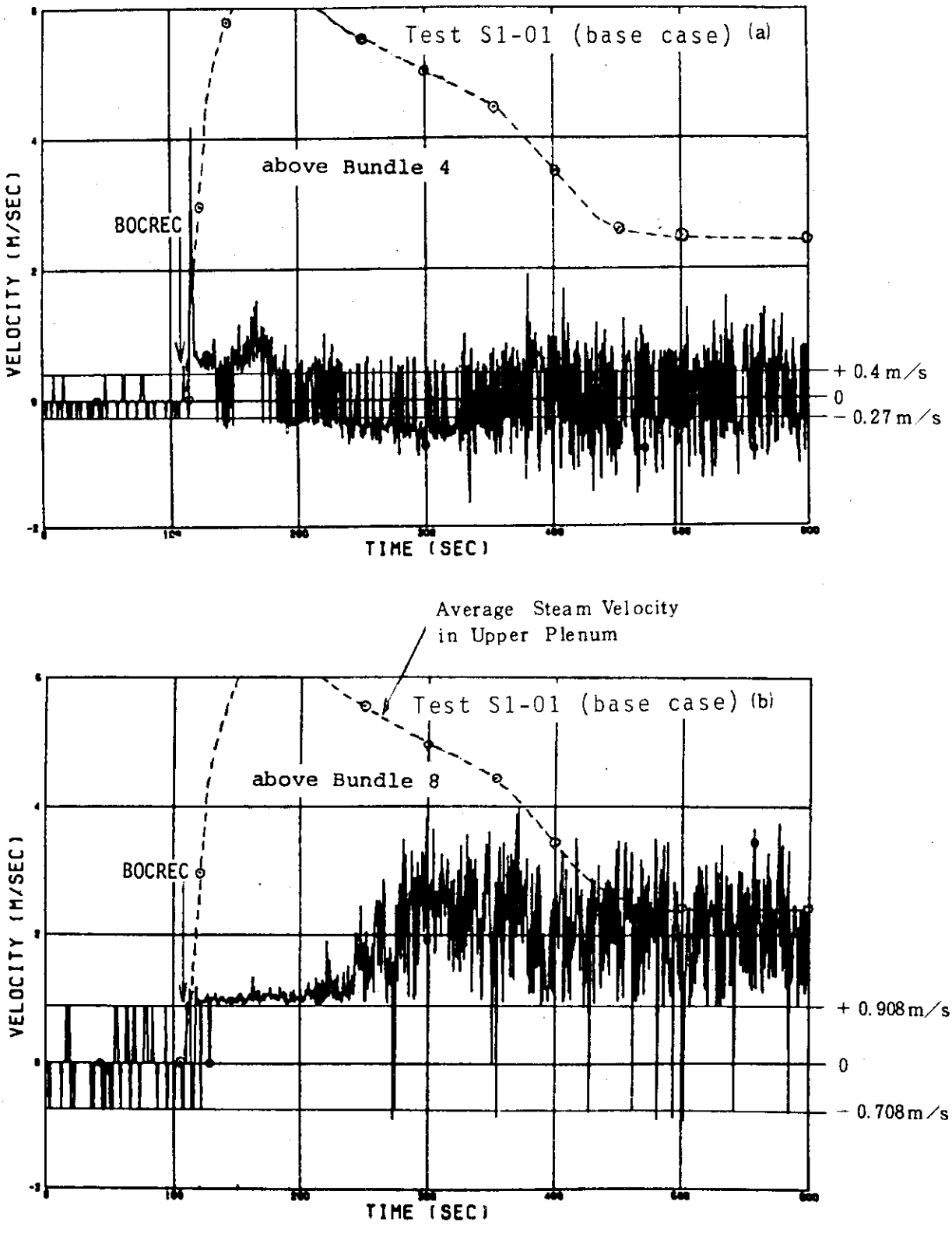

Fig. 3-22 Upward fluid velocities in upper plenum measured with turbine meters and average steam velocity in upper plenum

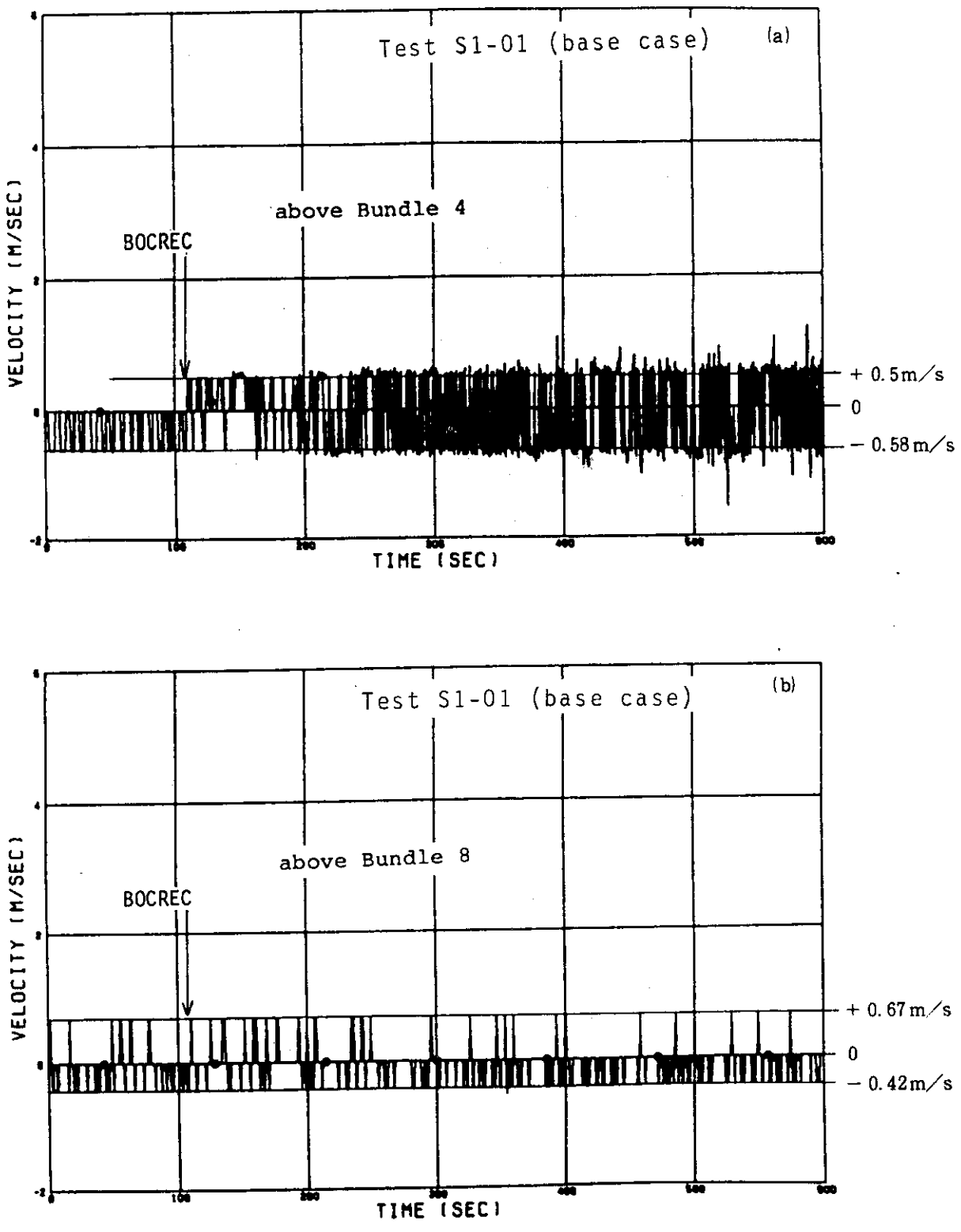

Fig. 3-23 Horizontal fluid velocities in upper plenum measured with turbine meters

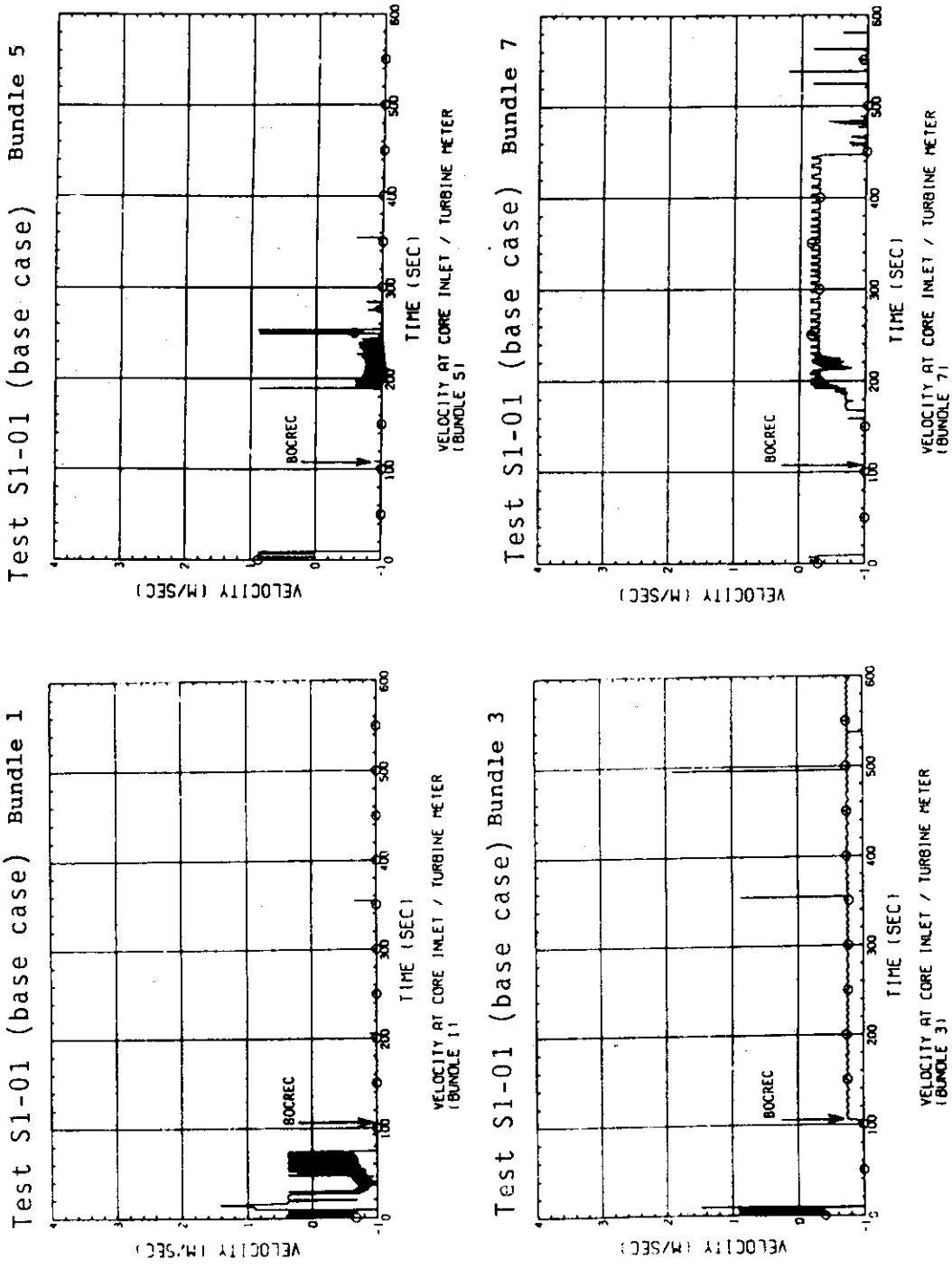

Fig. 3-24 Core inlet water velocities measured with turbine meters

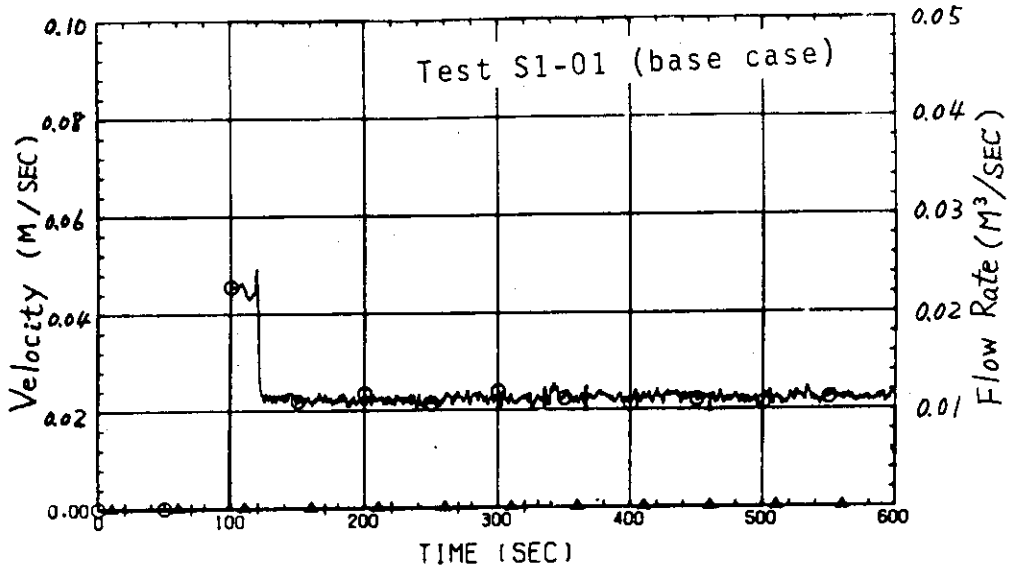

Fig. 3-25 Transient of ECC water flow rate into lower plenum

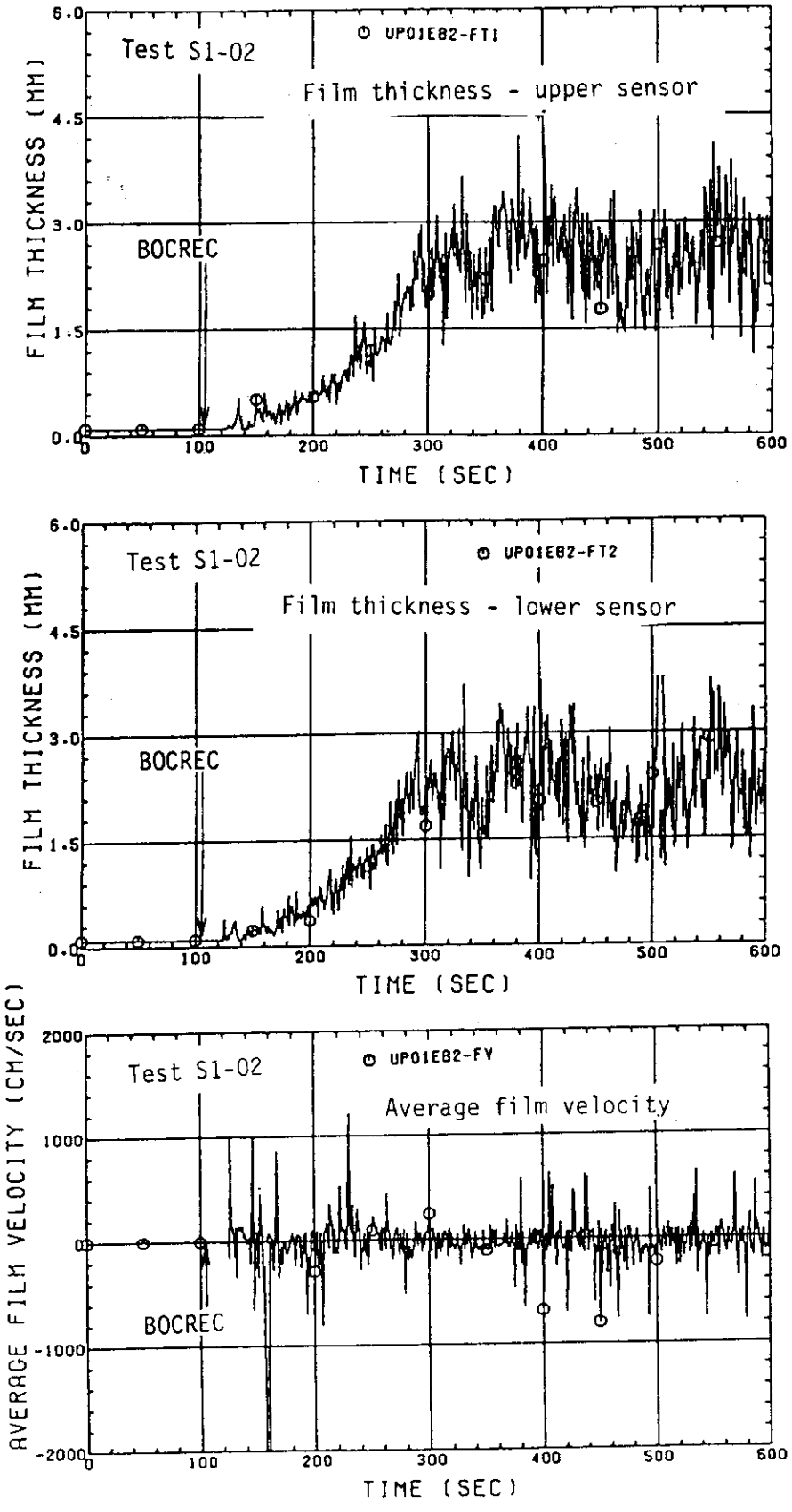

Fig. 3-26 Film thicknesses and average film velocity measured with core side wall film probe

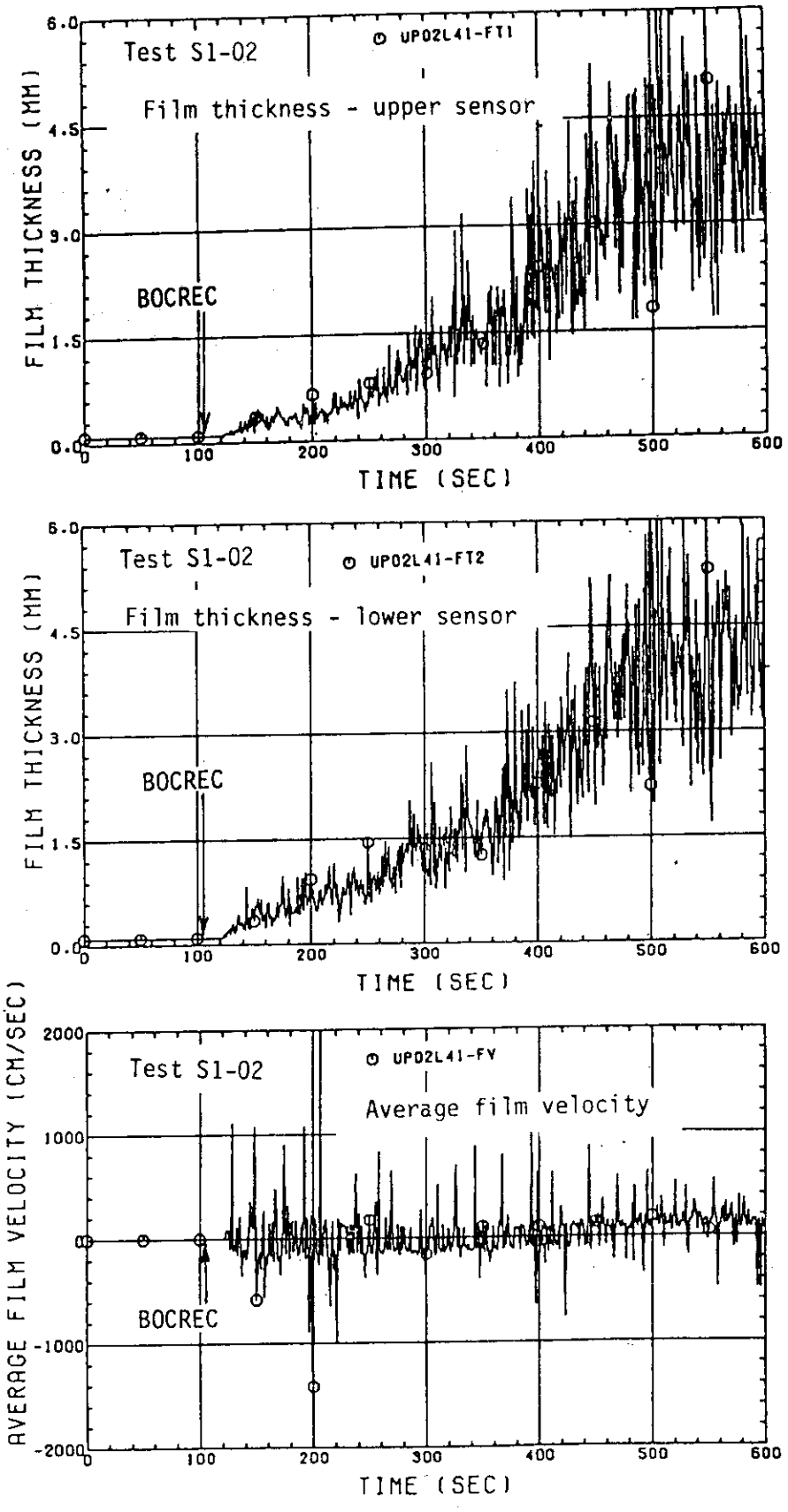

Fig. 3-27 Film thicknesses and average film velocity measured with upper plenum structure film probe

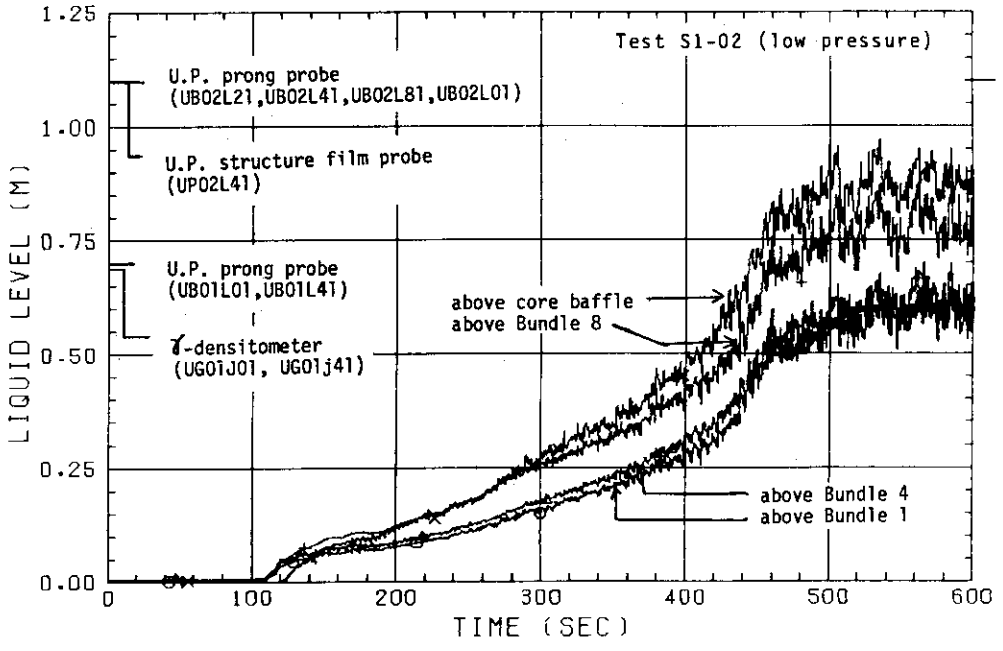

(a) Liquid level above UCSP

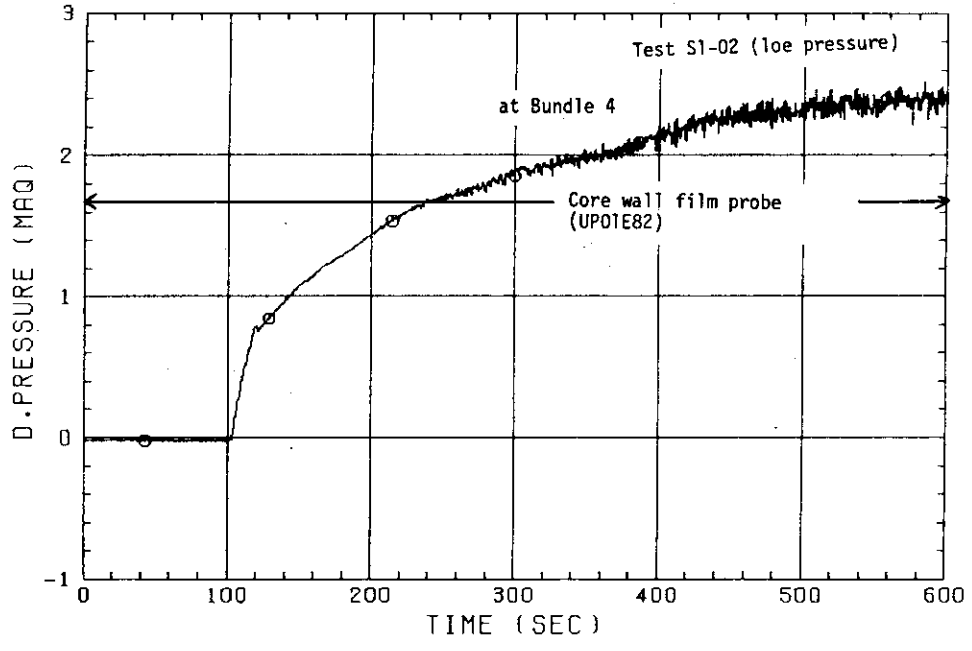

(b) Collapsed water level in core

Fig. 3-28 Collapsed liquid levels in upper plenum and core

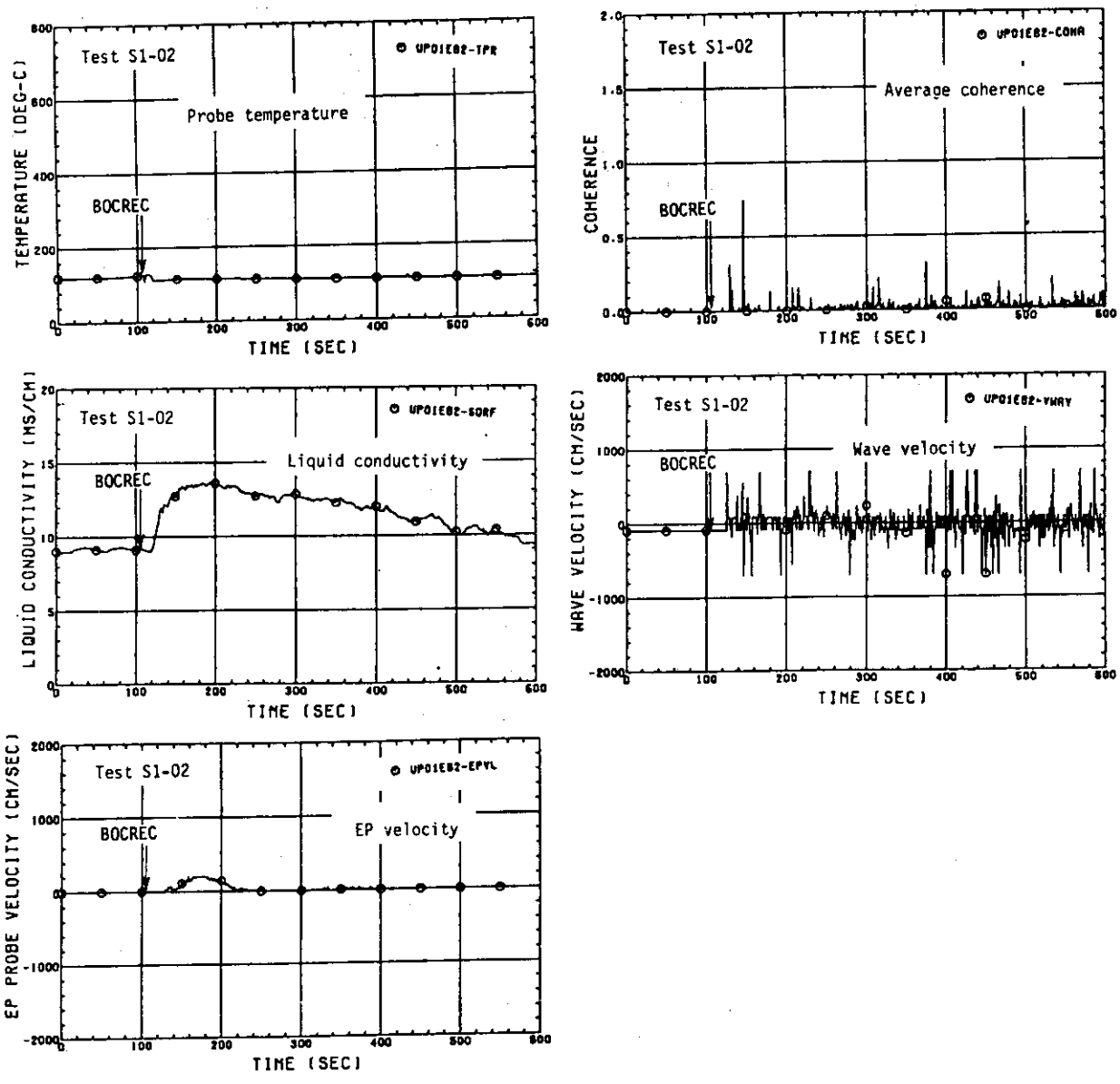

Fig. 3-29 Probe temperature, liquid conductivity, EP velocity, average coherence and wave velocity measured with core side wall film probe

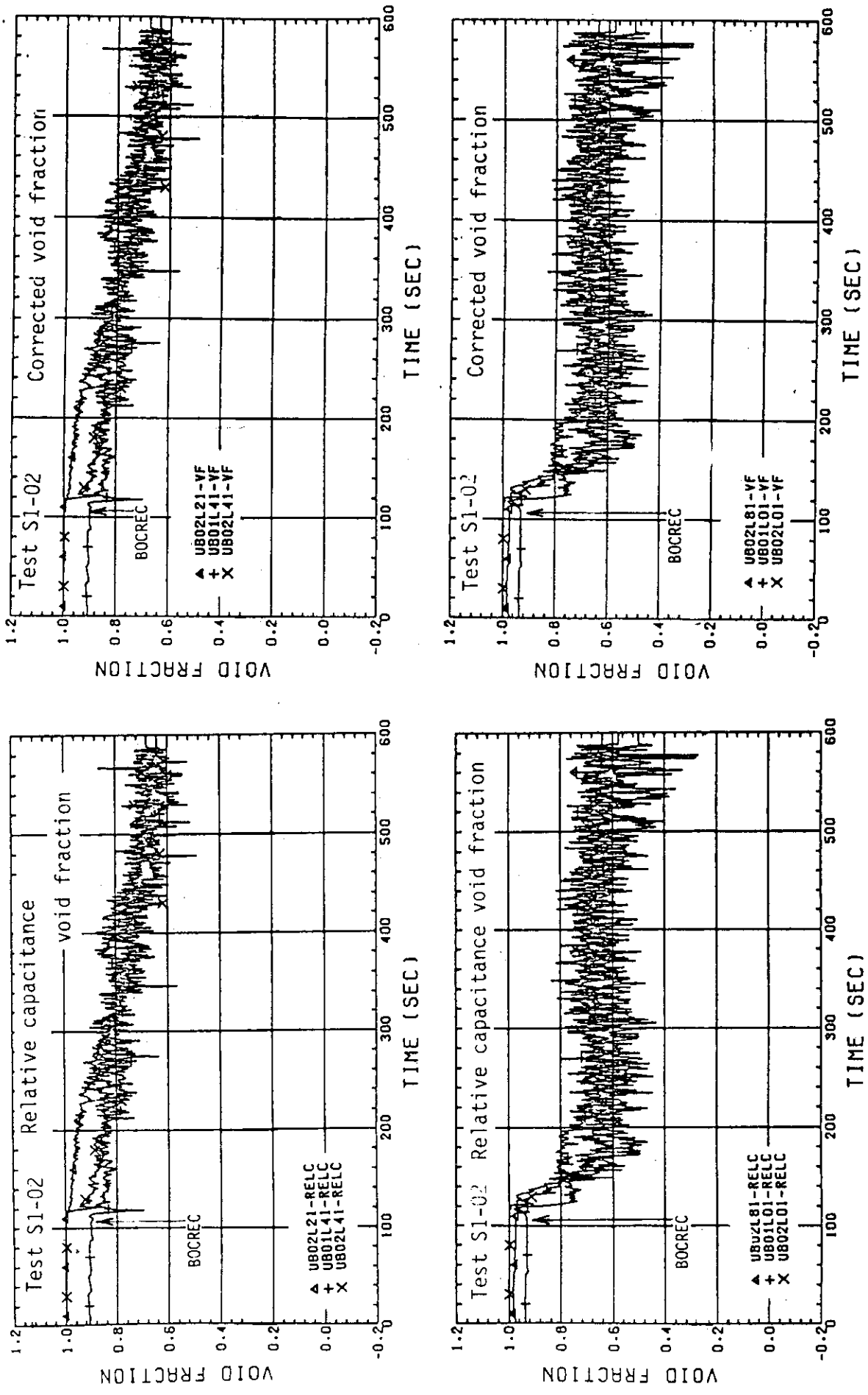

Fig. 3-30 Void fractions measured with upper plenum prong probes

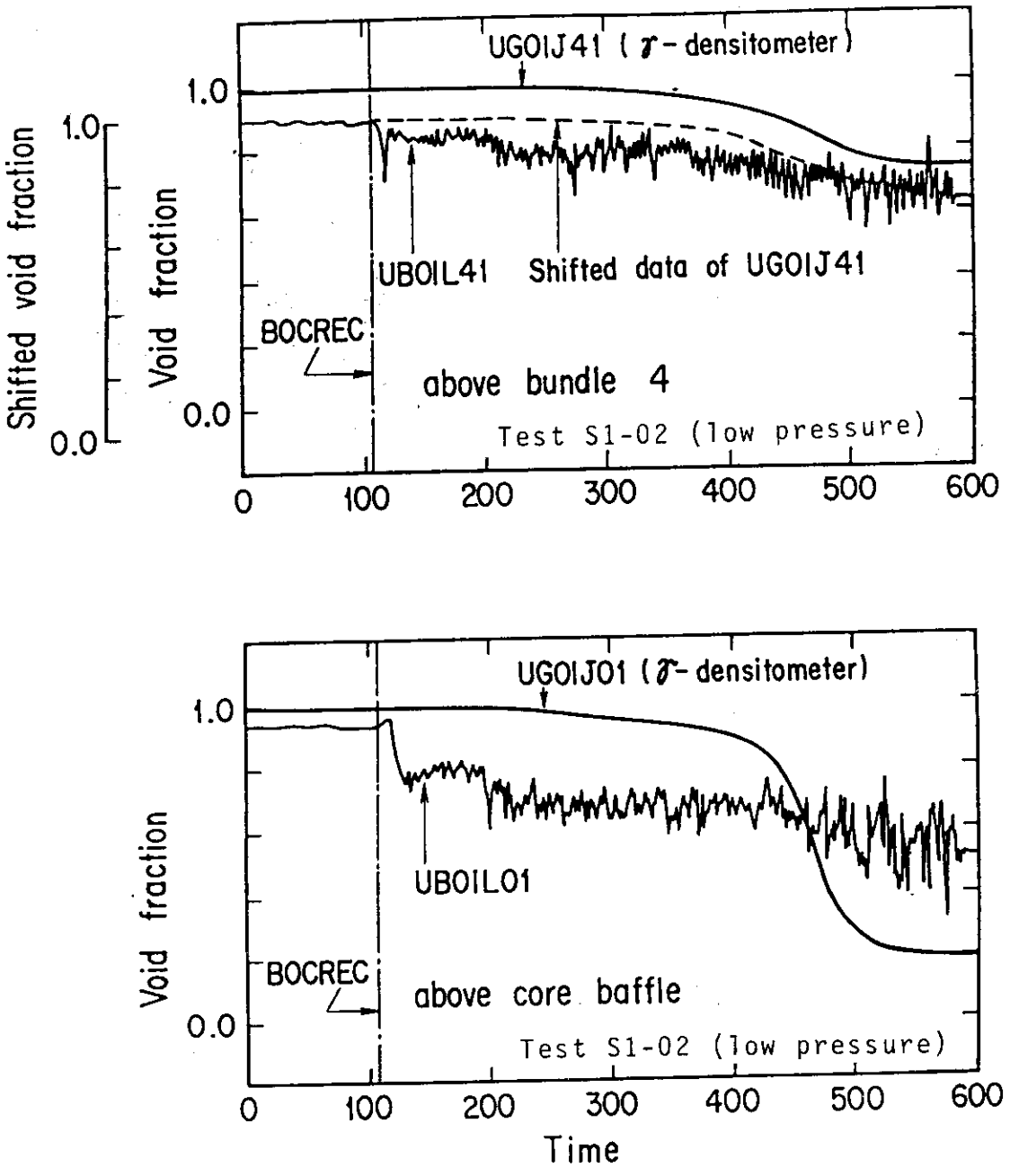

Fig. 3-31 Comparisons between void fractions measured with upper plenum prong probes and void fractions calculated from γ-densitometers

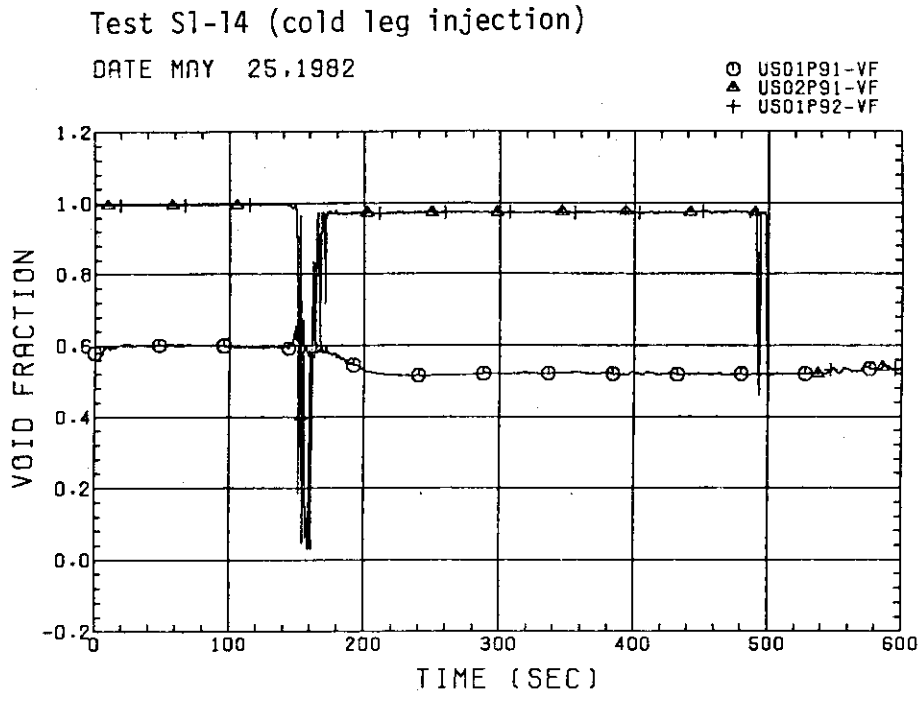

(a) Void fraction in downcomer
mesured with string probe

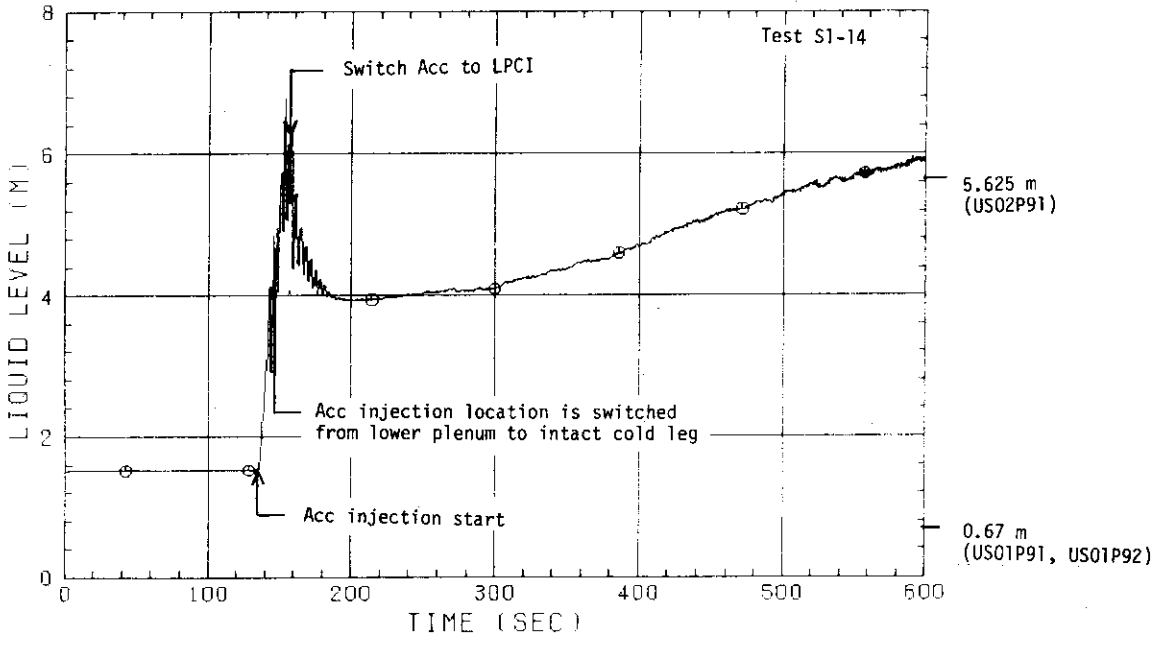

(b) Liquid level in downcomer
mesured with D/P cell

Fig. 3-32 Void fractions measured with downcomer string probes and liquid level in downcomer

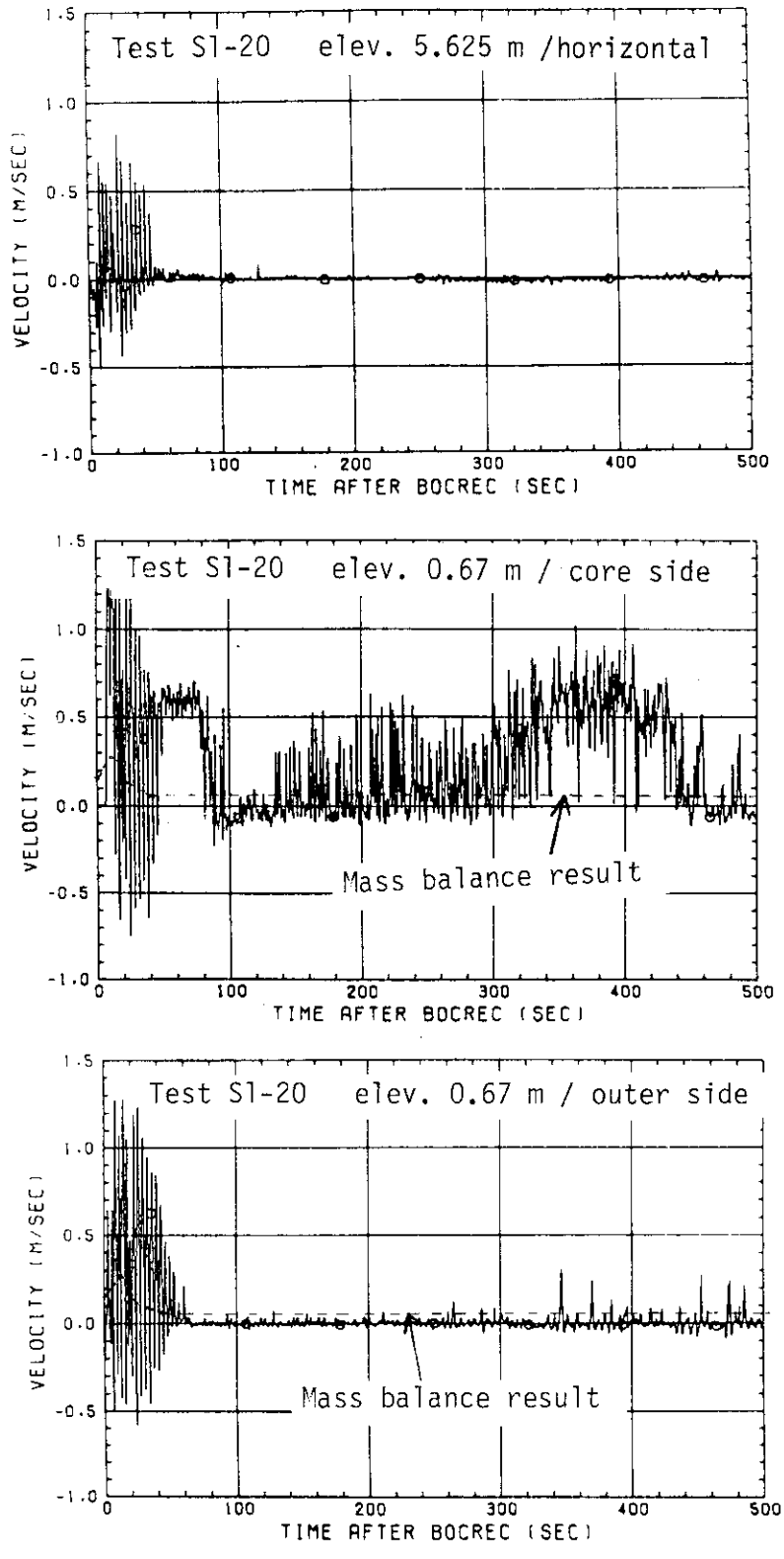

Fig. 3-33 Fluid velocities in downcomer measured with downcomer drag disks

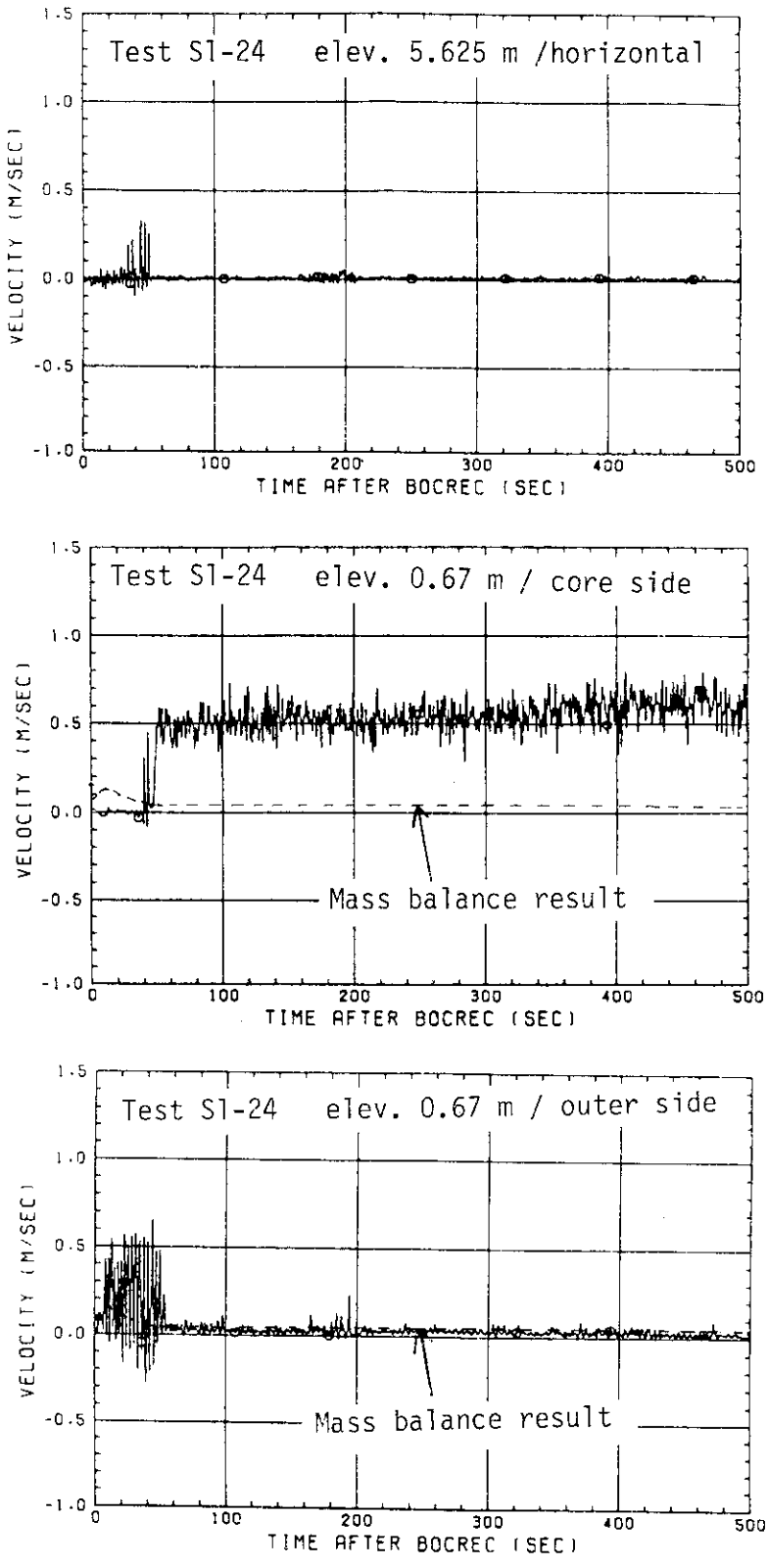

Fig. 3-33 (continue)

4. Problems

4.1 Turbine Meter

The bearings of turbine meter should be replaced several times during the SCTF Core-I test series. Test No's that used the same ball bearings of turbine shaft are as follows:

(1) Tests. S1-SH1, S1-SH2, S1-01 and S1-02,
(2) Tests. S1-03 through S1-06,
(3) Tests. S1-07 through S1-12,
(4) Tests. S1-13 through S1-15,
and (5) Tests. S1-16 through S1-19.

The ratio between the turbine velocity and the core average velocity calculated from the Venturi flow meter data are shown in Figs. 4-1 (a) and (b) for series (2) and series (3), respectively, at 140 seconds after core power on. In Fig. 4-1 (b), the repeatability tests, Tests S1-07 and S1-11, show almost the same value except above bundle 6. Therefore, the exchange of ball bearing did not remarkably affect the data of turbine meters.

4.2 Spool Piece

(1) Pressure, Differential Pressure and Temperature

There was no trouble in these detectors. However, there were some problems about air drawing system in the differential pressure measurement.

(2) γ-Densitometer (Cold leg)

The vacuum for the 3-beam γ-densitometer system was often not kept

(3) Drag Disk

Many failures occurred in the amplifier of drag disk. The failures of the circuit were brought about by the connection error at the connector because it was nessesary to draw out the amplifire module in order to adjust the data and zero point.

4.3 In-Core γ-Densitometer

The output signals of in-core γ-densitometers sometimes went down to zero during the test. This is caused by the moving of the rod bundles.

4.4 Conax Seal Problem

As presented in sections 3.3 and 3.5, most of the LLDs, FDGs, film probes and impedance probes did not work well from the beginning of SCTF Core-I test series. These failures are not due to the problems of each sensor itself but due to the stress corrosion of the conax seal of hard cable. Grafoil was used as the conax seal in the SCTF Core-I series. The material was changed to Teflon in the SCTF Core-II series in order to prevent from the stress corrosion. Therefore, good data are expected to be obtained from these instruments in the SCTF Core-II.

4.5 Downcomer Drag Disk and String Probe

Both of the drag disk and the string probe at the upper part of the downcomer were not installed vertically but installed horizontally by mistake. Therefore, the horizontal velocity from the intact cold leg side to the broken cold leg side could not be measured.

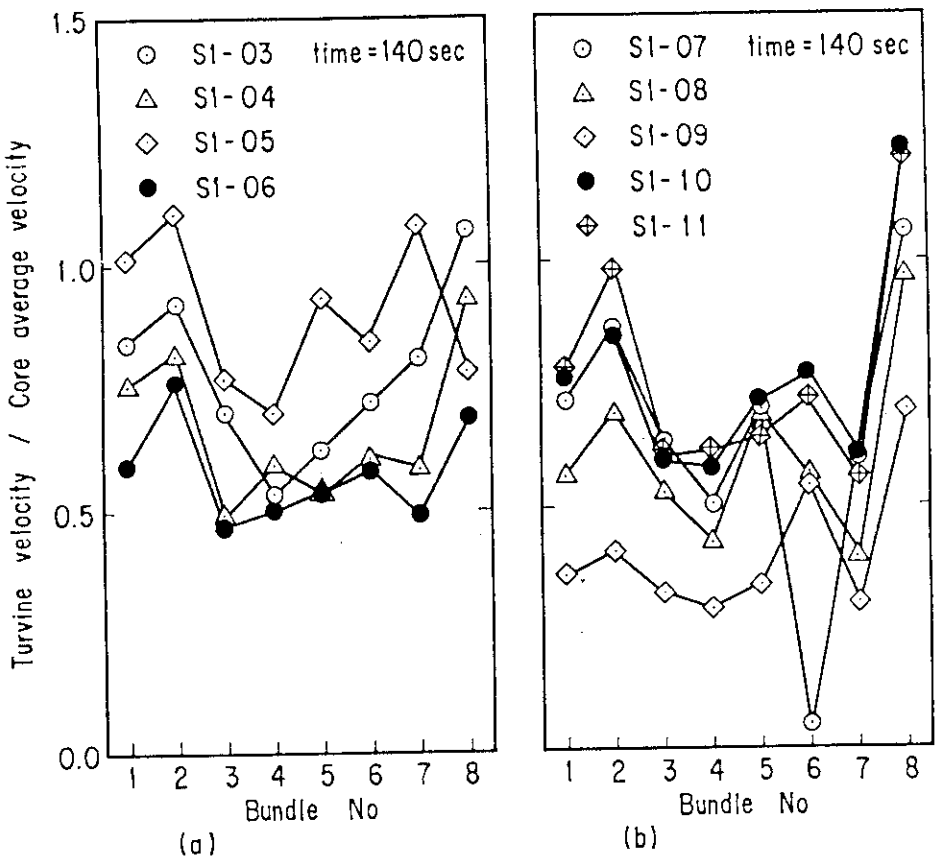

Fig. 4-1 Effects of bearing exchange on turbine meters

5. Conclusions

The data obtained from the USNRC-provided advanced two-phase flow instrumentation were evaluated from the view point of reliability and the following conclusions were obtained.

I. Spool Pieces

(1) The hot leg spool piece worked successfully, i.e., void fraction data and total mass flow rate data from the hot leg spool piece agreed well with those from the conventional instruments.
(2) Fluid velocity data from the hot leg spool piece at the region 1 (top region of the hot leg cross section) or the region 2 (second region from the top) agreed well with the steam velocity obtained from the conventional instruments.
(3) The hot leg flow reversal was clearly detected by the hot leg spool piece at the region 4 (bottom region).

II. γ-Densitometers

(1) The γ-densitometers attached to the pressure vessel wall worked relatively well, i.e., qualitative coincidence was confirmed with the void fractions calculated from differential pressures. However, the γ-denstitometer gave the higher void fraction than the differential pressure especially at the upper part of the core.
(2) The γ-densitometers are very useful for two-dimensional analysis of core thermo-hydrodynamic behavior, because they indicate chordal average void fraction compared with the vertical average void fraction obtained by the differential pressure method.
(3) Sometimes, the beam of the γ-densitometer at the middle of core was interferred by the movement of rod bundles just after the Acc injection initiation.

III. LLDs and FDGs

(1) Most of LLDs in the core and FDGs in the upper plenum and downcomer did not work because of the corrosion of hard cable penetration part through the pressure boundary.

Ⅳ. Turbine Flowmeters

(1) The UCSP turbine flowmeters provided reasonable steam velocity just after the beginning of reflood when the flow through the UCSP holes was steam dominant flow.

(2) With increasing the entrained water flow rate, the difference of the steam velocity measured with the UCSP turbine flowmeter from the average steam velocity obtained by mass balance calculation increased.

(3) The upper plenum turbine flowmeters for both vertical flow and horizontal flow did not work well.

(4) The core inlet turbine flowmeters did not work well because of unsuitable measurement range.

Ⅴ. Film Probes

(1) Film thickness data from some film probes on the core side wall and the upper plenum structure wall were qualitatively good but not reasonable quantitatively.

(2) Film velocity data were meaningless.

(3) Many film probes attached to the core side wall, upper plenum side wall, upper plenum structures and non-heated rods did not work well because of the hard cable stress corrosion.

Ⅵ. Impedance Probes

(1) Void fraction data from some upper plenum prong probes were qualitatively good but not reasonable quantitatively.

(2) The downcomer string probes did not give reasonable results.

(3) Many flag probes attached to the non-heated rods have the similar hard cable problem described above.

Ⅶ. Downcomer Drag Disks

(1) The water velocities masured with the downcomer drag disks were not in good agreement with those obtained by the mass balance calculation.

(2) The two-phase mass flow rate could not be obtained because both of the drag disks and the string probes did not work well.

Ⅷ. Video Optical Probes (VOPs)

(1) VOPs attached to the upper plenum and just below the end box tie plate worked well and provided useful information on the flow pattern.

Acknowledgement

The authors are much indebted to Dr. M. Nozawa, Dr. S. Katsuragi, Dr. M. Hirata, Dr. K. Hirano and Dr. Y. Murao of JAERI for their guidance and encouragement for this program.

They would like to express their thanks to Messers. T. Wakabayashi and Y. Niitsuma of JAERI and to the 2D/3D project members of the USA, especially Dr. L. H. Sullivan of USNRC and Mr. D. H. Miyasaki and Mr. C. Winsel of resident engineers from USNRC to JAERI for their devoted help for the advanced instrumentation in SCTF Core-I.

The authors also would like to express their appreciation to Mr. T. Iguchi, Mr. K. Okabe, Mr. J. Sugimoto, Dr. H. Akimoto and Mr. T. Okubo of the CCTF analysis group for their valuable discussions.

References

(1) H. Adachi et al.: Design of Slab Core Test Facility in Large Scale Reflood Test Program Part I: Core-I, JAERI-M 83-080 (1983).

(2) T. Iwamura and H. Adachi: Evaluation of cross Flow Velocity across Rod Bundles during Reflood Phase in SCTF Core-I Forced-Feed Flooding Tests, Private Communication.

(3) M. Osakabe et al.: Droplets Flow and Heat Transfer at Top Region of Core in Reflood Phase, JAERI-M 83-022 (1983).

(4) T. Iguchi: Definition of Void Fraction used in CCTF Data Analysis, Private Communication.

(5) C. A. Mancuso: SCTF Software Users Manual, Private Communication.

(6) Oak Ridge National Laboratory: Impedance and Film Probe Software for SCTF-1 User Information, Private Communication.

(7) H. Adachi, et al.: System Pressure Effects on Reflooding Phenomena observed in the SCTF Core-I Forced Flooding Test, JAERI-M 83-079, (1983).

(8) J. G. Collier,: Convective Boiling and Condensation, McGRAW-HILL, Fig. 1.5, (1983).

(9) J. B. Colson, Private Communication.

Acknowledgement

The authors are much indebted to Dr. M. Nozawa, Dr. S. Katsuragi, Dr. M. Hirata, Dr. K. Hirano and Dr. Y. Murao of JAERI for their guidance and encouragement for this program.

They would like to express their thanks to Messers. T. Wakabayashi and Y. Niitsuma of JAERI and to the 2D/3D project members of the USA, especially Dr. L. H. Sullivan of USNRC and Mr. D. H. Miyasaki and Mr. C. Winsel of resident engineers from USNRC to JAERI for their devoted help for the advanced instrumentation in SCTF Core-I.

The authors also would like to express their appreciation to Mr. T. Iguchi, Mr. K. Okabe, Mr. J. Sugimoto, Dr. H. Akimoto and Mr. T. Okubo of the CCTF analysis group for their valuable discussions.

References

(1) H. Adachi et al.: Design of Slab Core Test Facility in Large Scale Reflood Test Program Part I: Core-I, JAERI-M 83-080 (1983).

(2) T. Iwamura and H. Adachi: Evaluation of cross Flow Velocity across Rod Bundles during Reflood Phase in SCTF Core-I Forced-Feed Flooding Tests, Private Communication.

(3) M. Osakabe et al.: Droplets Flow and Heat Transfer at Top Region of Core in Reflood Phase, JAERI-M 83-022 (1983).

(4) T. Iguchi: Definition of Void Fraction used in CCTF Data Analysis, Private Communication.

(5) C. A. Mancuso: SCTF Software Users Manual, Private Communication.

(6) Oak Ridge National Laboratory: Impedance and Film Probe Software for SCTF-1 User Information, Private Communication.

(7) H. Adachi, et al.: System Pressure Effects on Reflooding Phenomena observed in the SCTF Core-I Forced Flooding Test, JAERI-M 83-079, (1983).

(8) J. G. Collier,: Convective Boiling and Condensation, McGRAW-HILL, Fig. 1.5, (1983).

(9) J. B. Colson, Private Communication.

Appendix A Detailed Locations for USNRC-Provided Advanced Instrumentation

The identification method of the instruments in the SCTF Core-I is described in Tables A-1 (in-core), A-2 (pressure vessel except core) and A-3 (outside of the pressure vessel), respectively.

The detailed measurement locations of the USNRC-provided instruments in the pressure vessel are shown in Figs. A-1 through A-10. Figures A-1 and A-2 show the vertical and horizontal locations, respectively, of the turbine flowmeters, drag disks, γ-densitometers, downcomer FDG, wall film probes, string probes and video optical probes. The locations of the turbine flowmeters in the upper plenum and just above the UCSP holes are shown in Fig. A-3. The measurement locations of the LLDs and FDGs are shown in Fig. A-4. Figures A-5 and A-6 show the measurement locations of the in-core film and flag probes, and the upper plenum film and prong probes, respectively. The installed locations of the hot leg, cold leg and vent pipe spool pieces are shown in Figs. A-7, A-8 and A-9. Figure A-10 shows the locations of the video optical probes as well as the view windows for JAERI-provided cameras and a cinecamera.

Table A-1 Description of Tag-ID number (in-core)

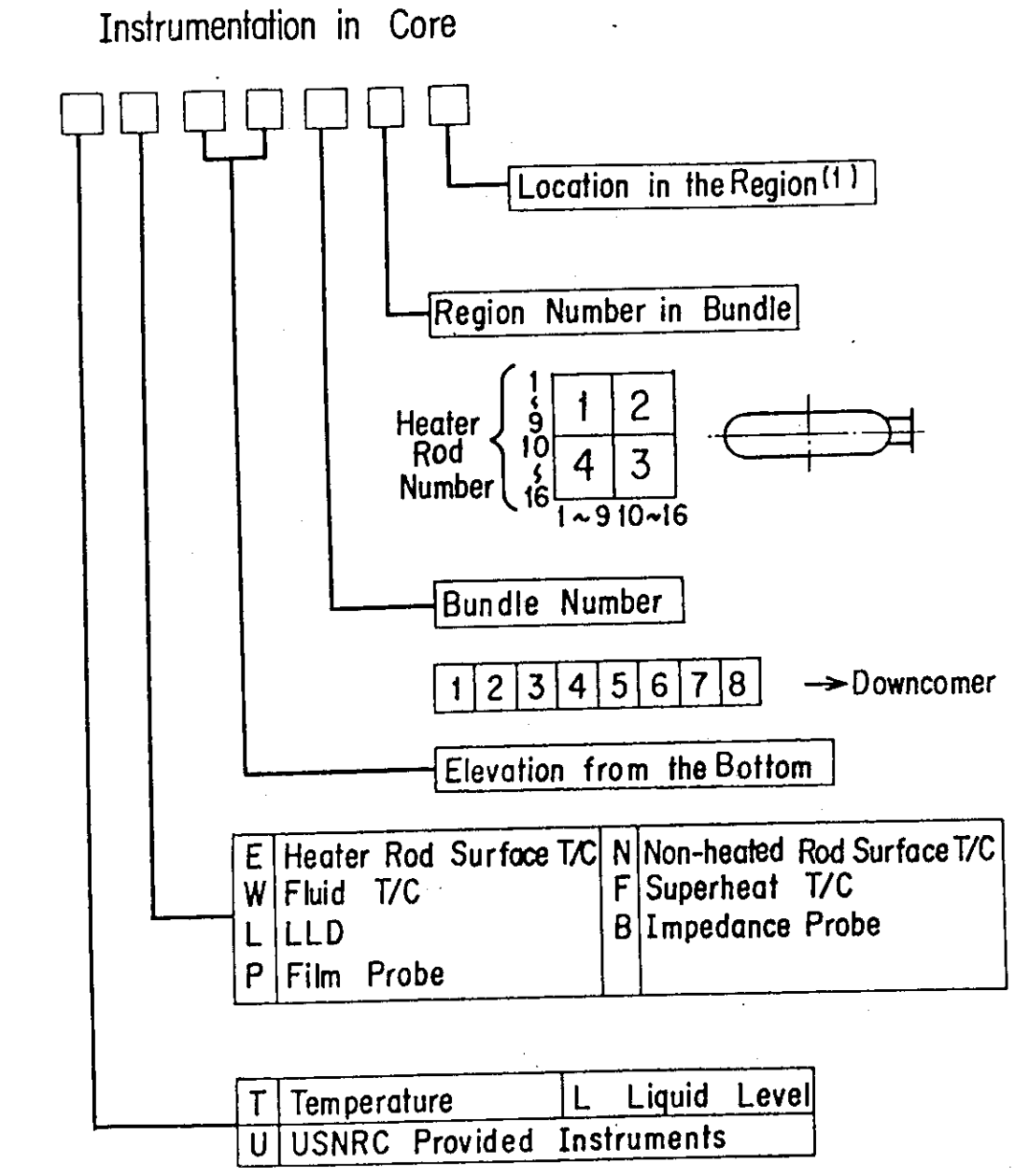

Note : (1) for Heater Rod T/C

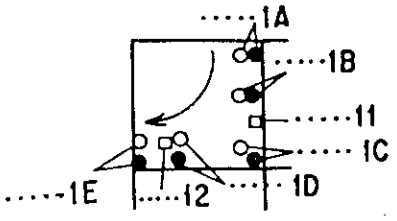

○ Upper half } Clockwise
● Lower half } A~E
□ Center } 1~2

Table A-2 Description of Tag-ID number (Pressure vessel except core)

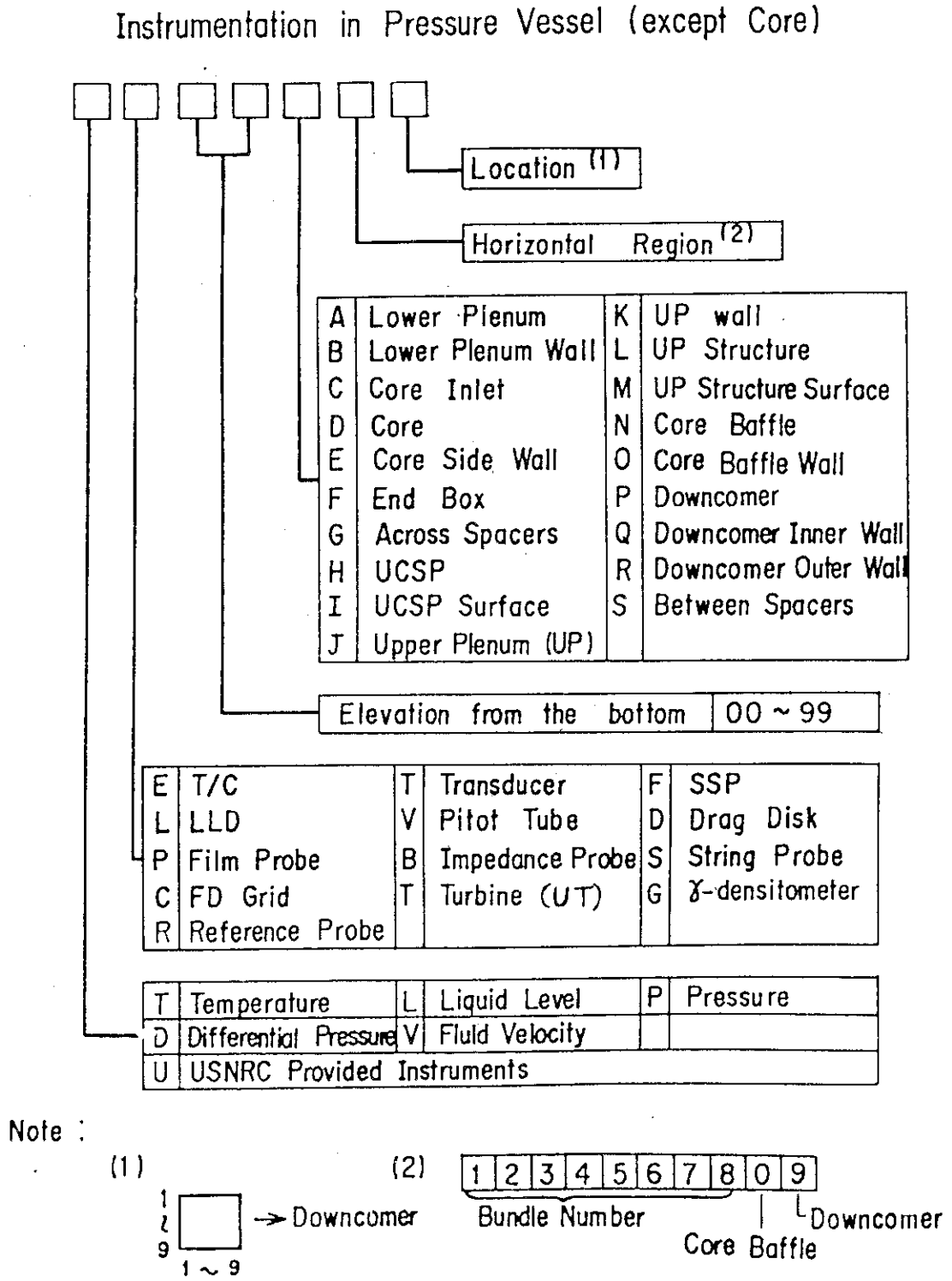

Note :

(1) 1 ~ 9 → Downcomer

(2) 1 2 3 4 5 6 7 8 0 9
Bundle Number
Core Baffle
Downcomer

Table A-3 Description of Tag-ID number (outside of pressure vessel)

Instrumentation in Loops

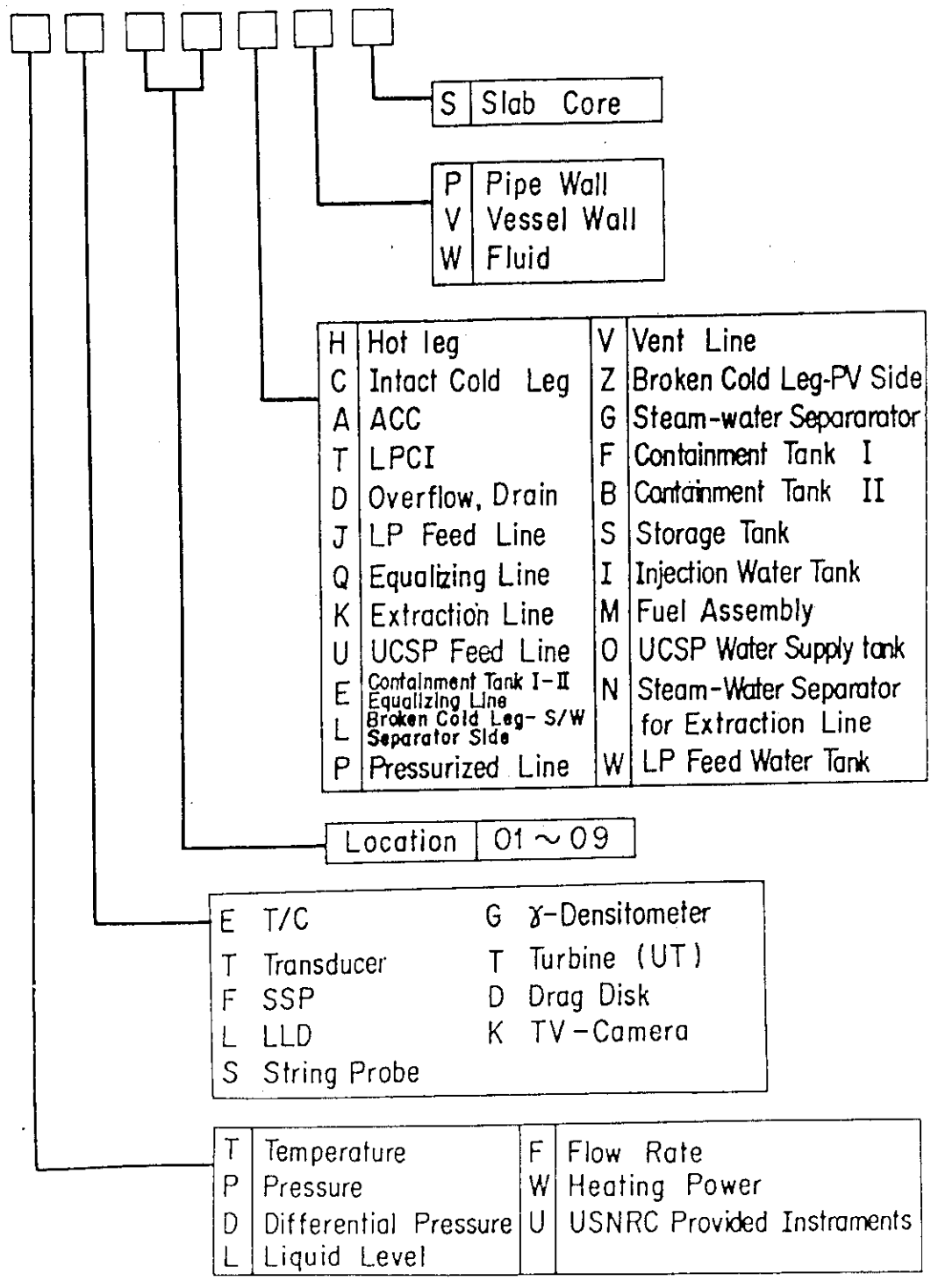

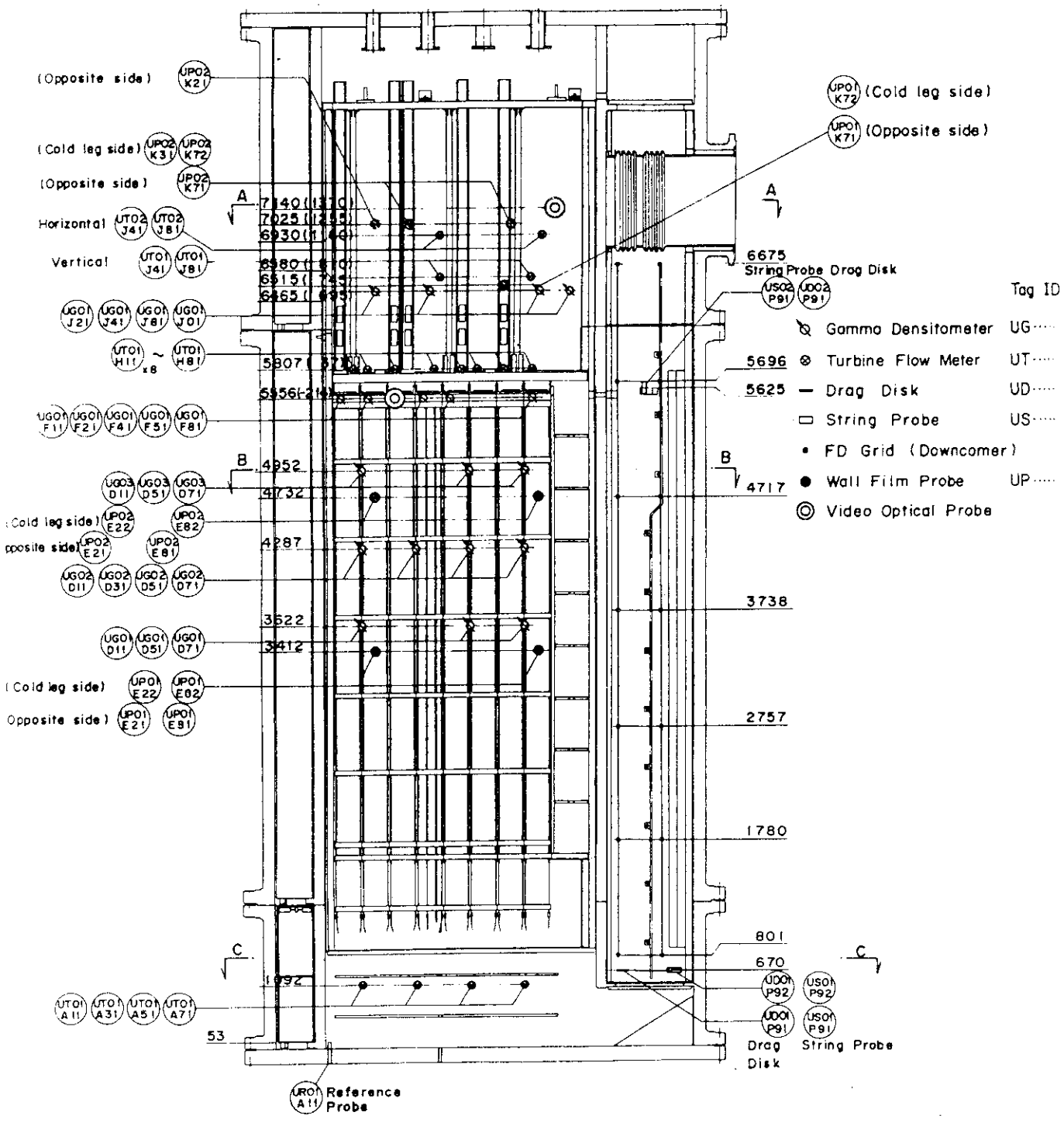

Fig. A-1 Vertical locations of USNRC-provided instruments in pressure vessel

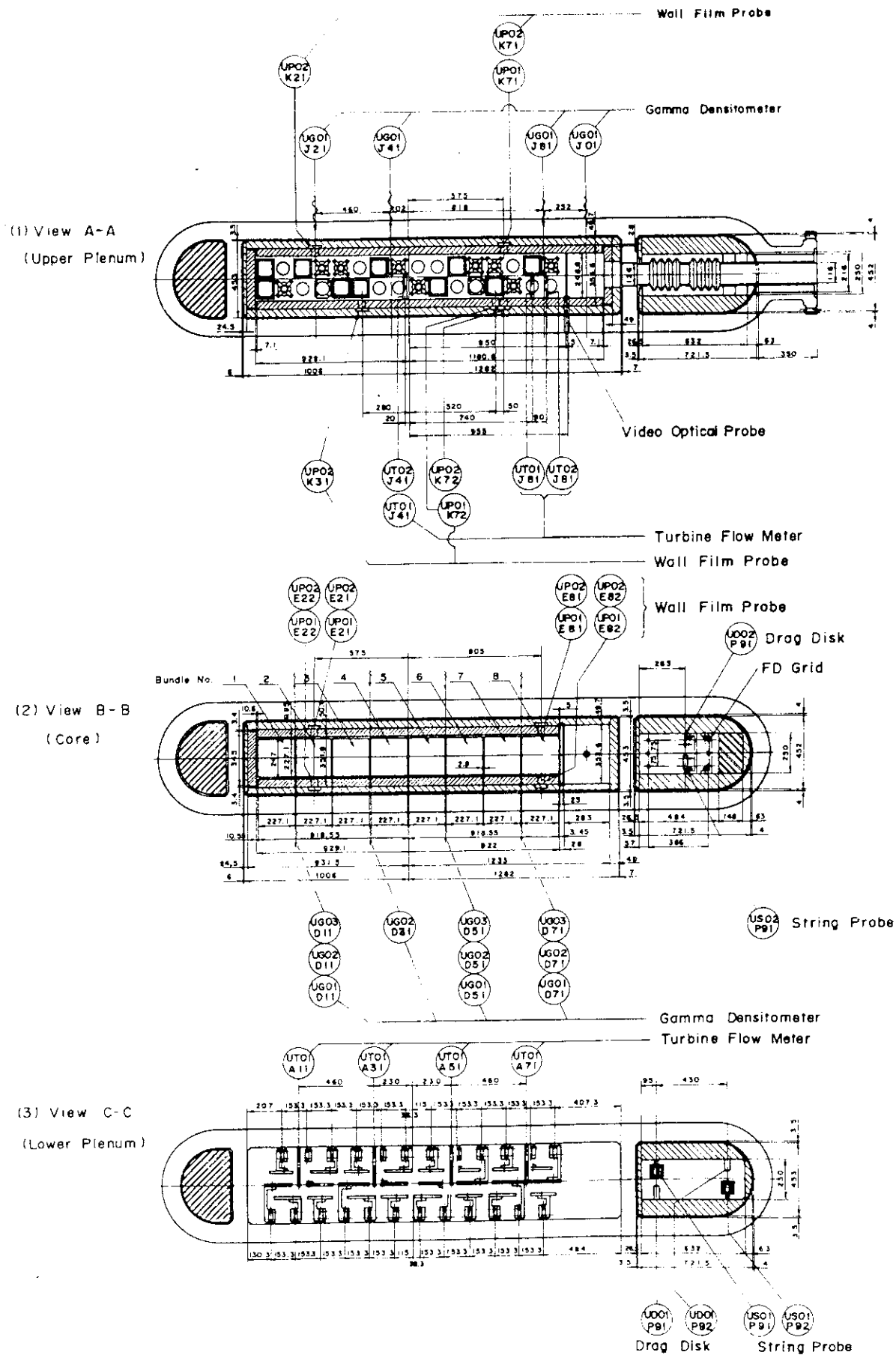

Fig. A-2 Horizontal locations of USNRC-provided instruments in pressure vessel

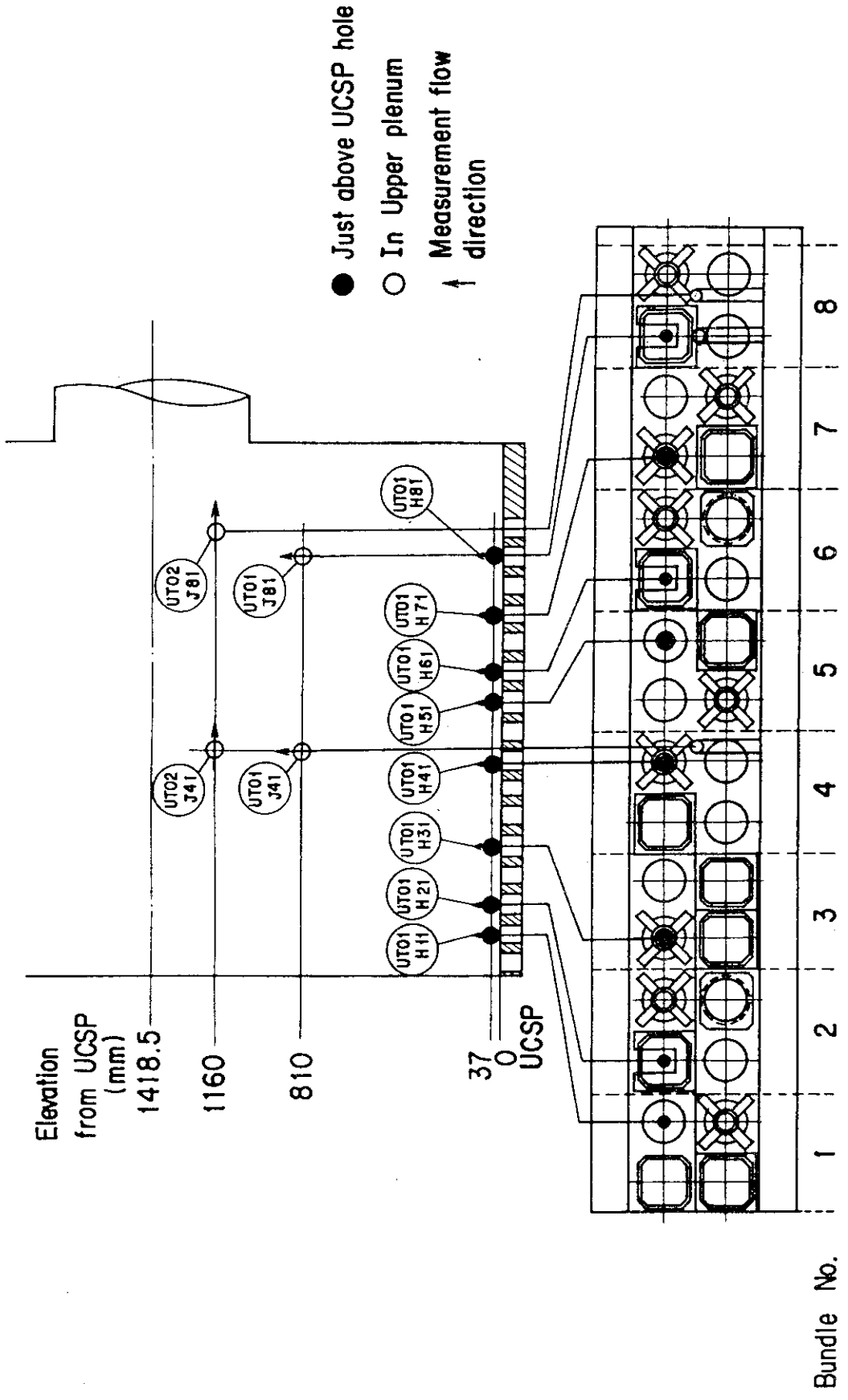

Fig. A-3 Measurement locations of turbine flowmeters in upper plenum

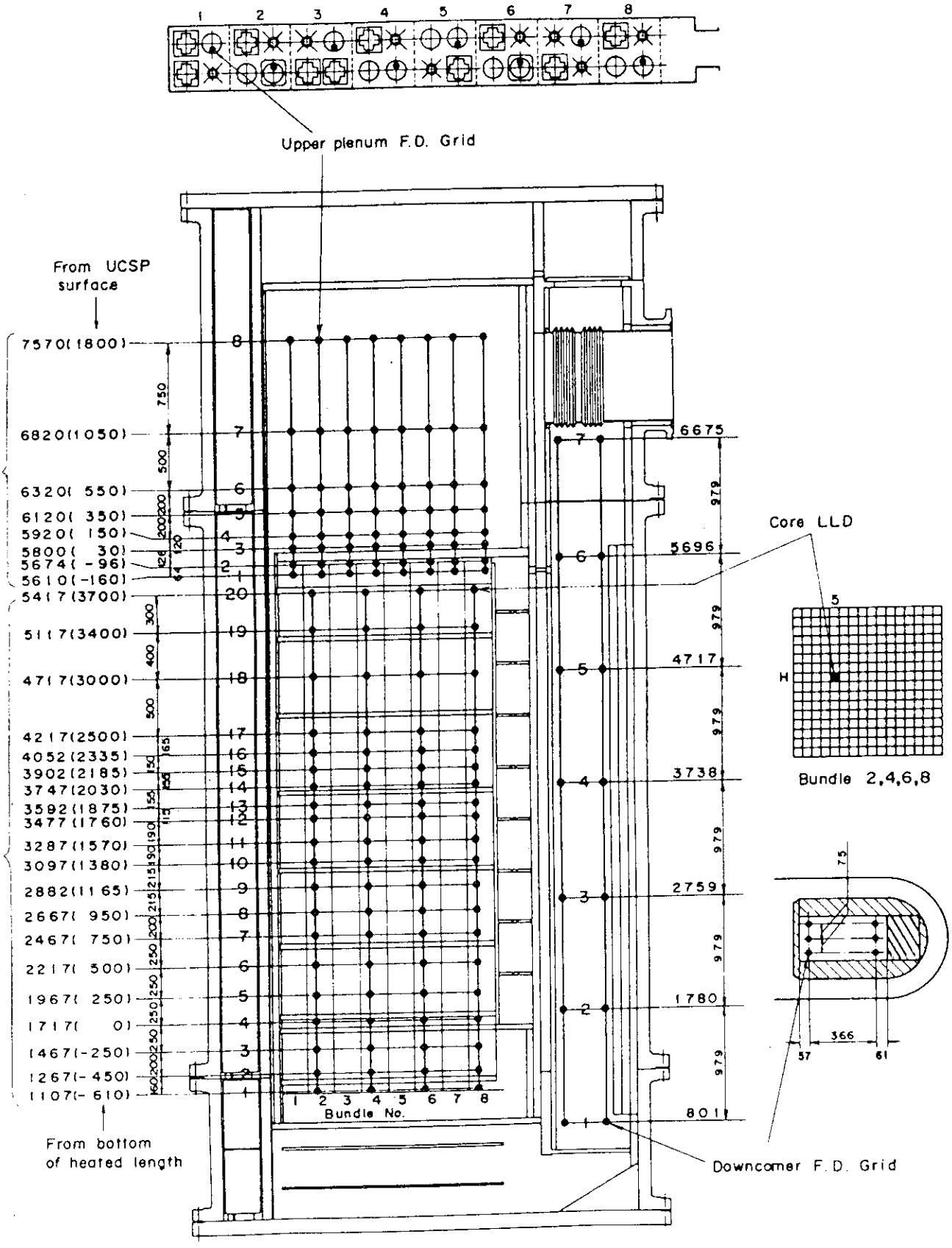

Fig. A-4 Measurement locations of LLDs and FDGs in pressure vessel

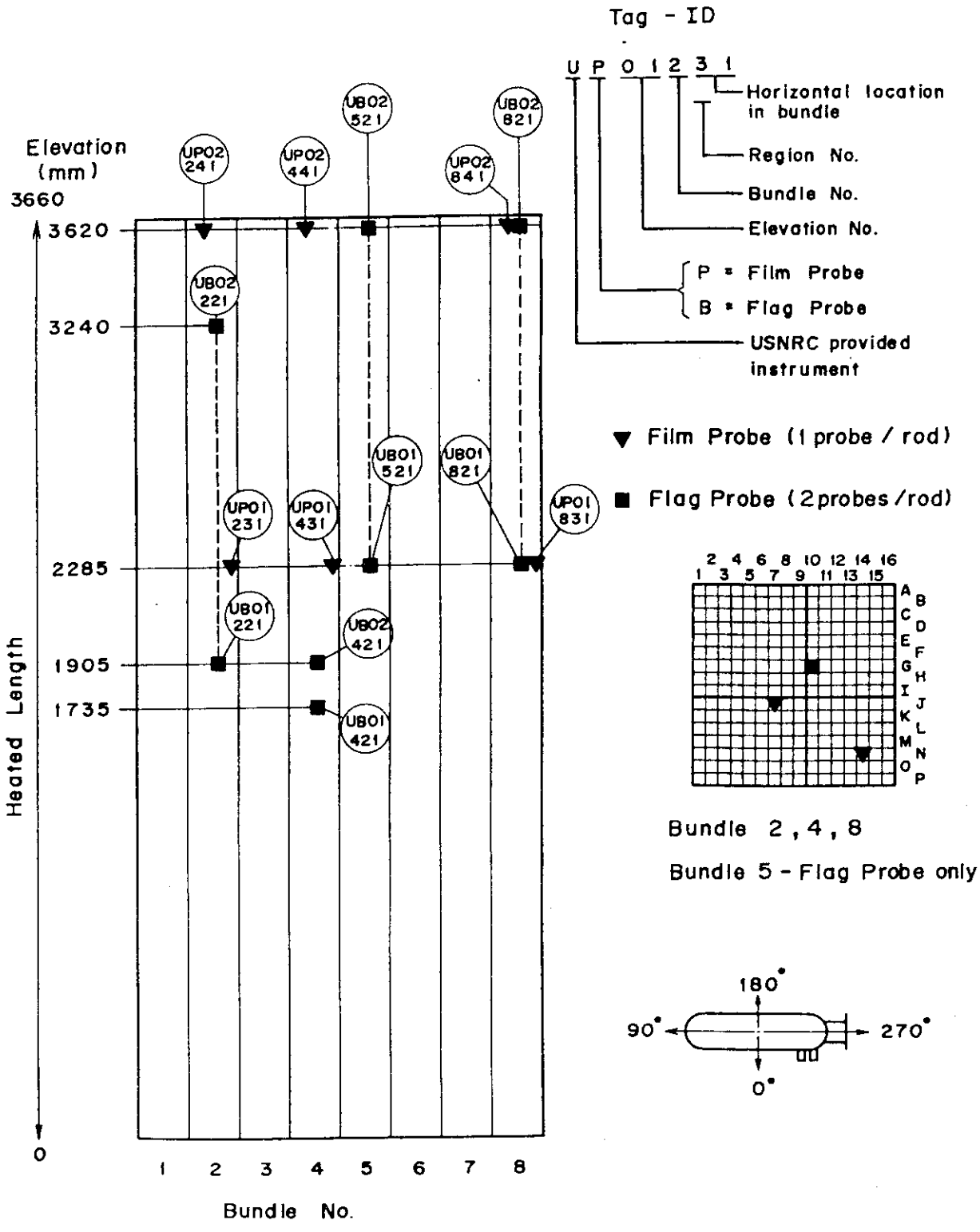

Fig. A-5 Measurement locations of film and flag probes in core

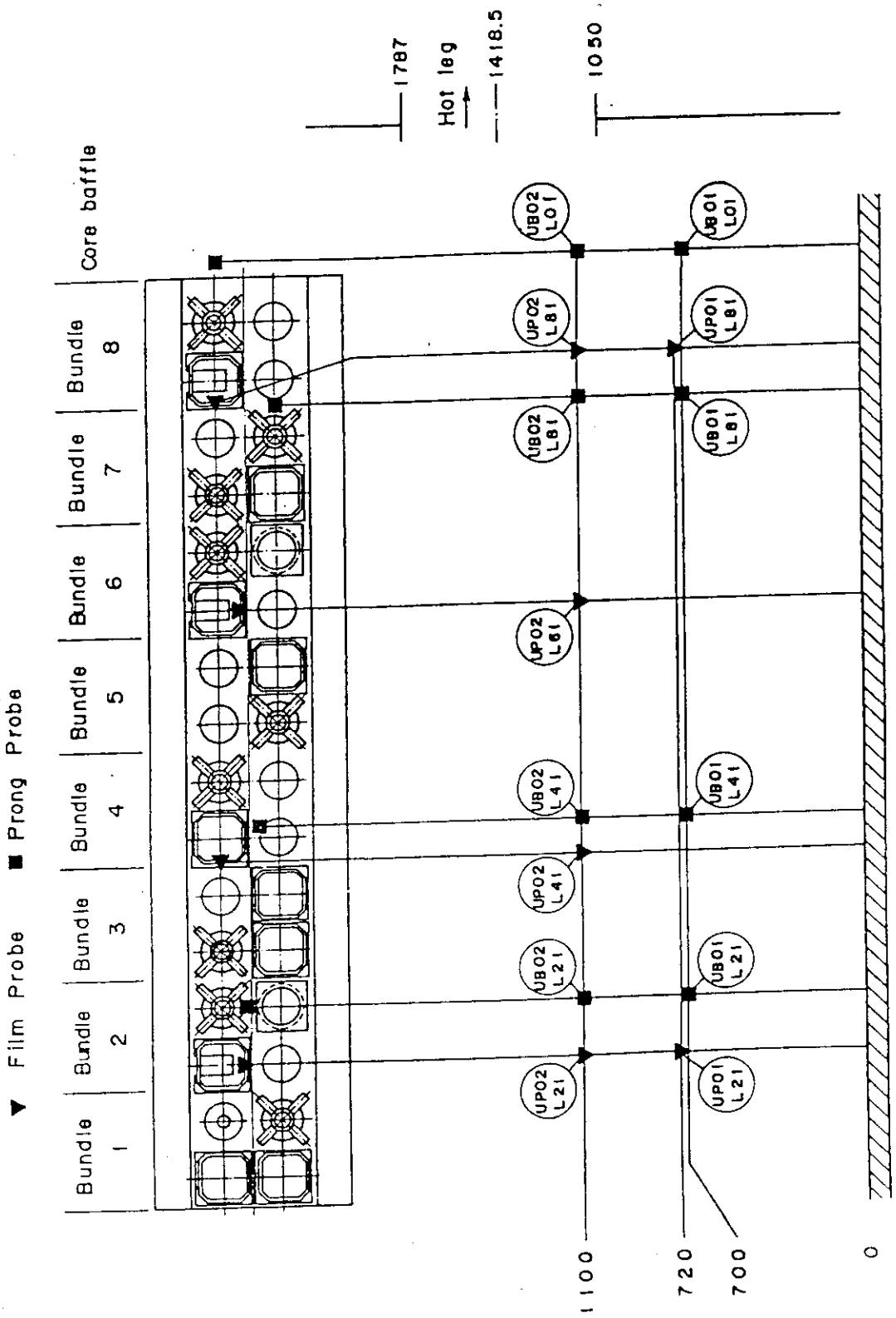

Fig. A-6 Measurement locations of film and prong probes in upper plenum

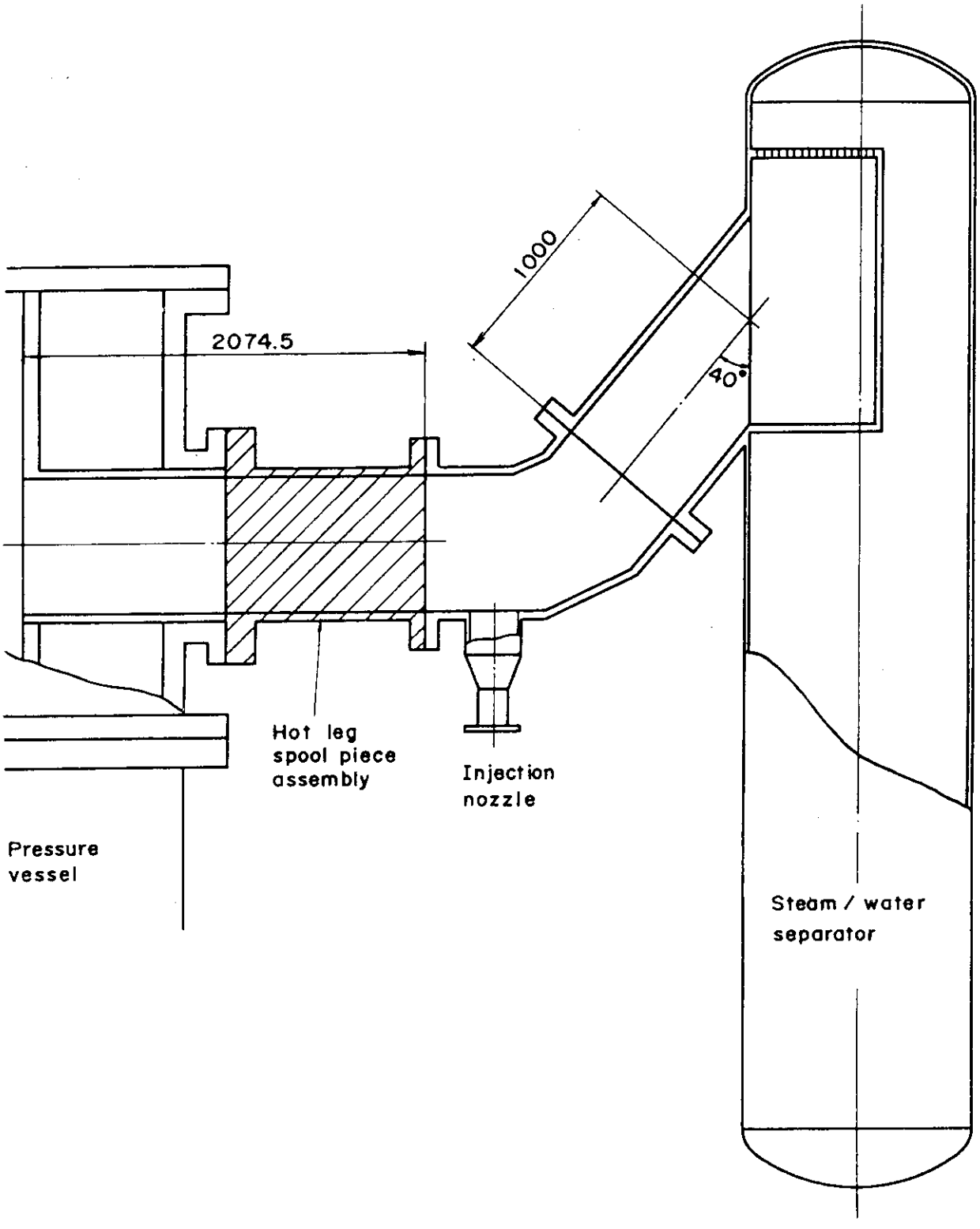

Fig. A-7 Installed location of hot leg spool piece

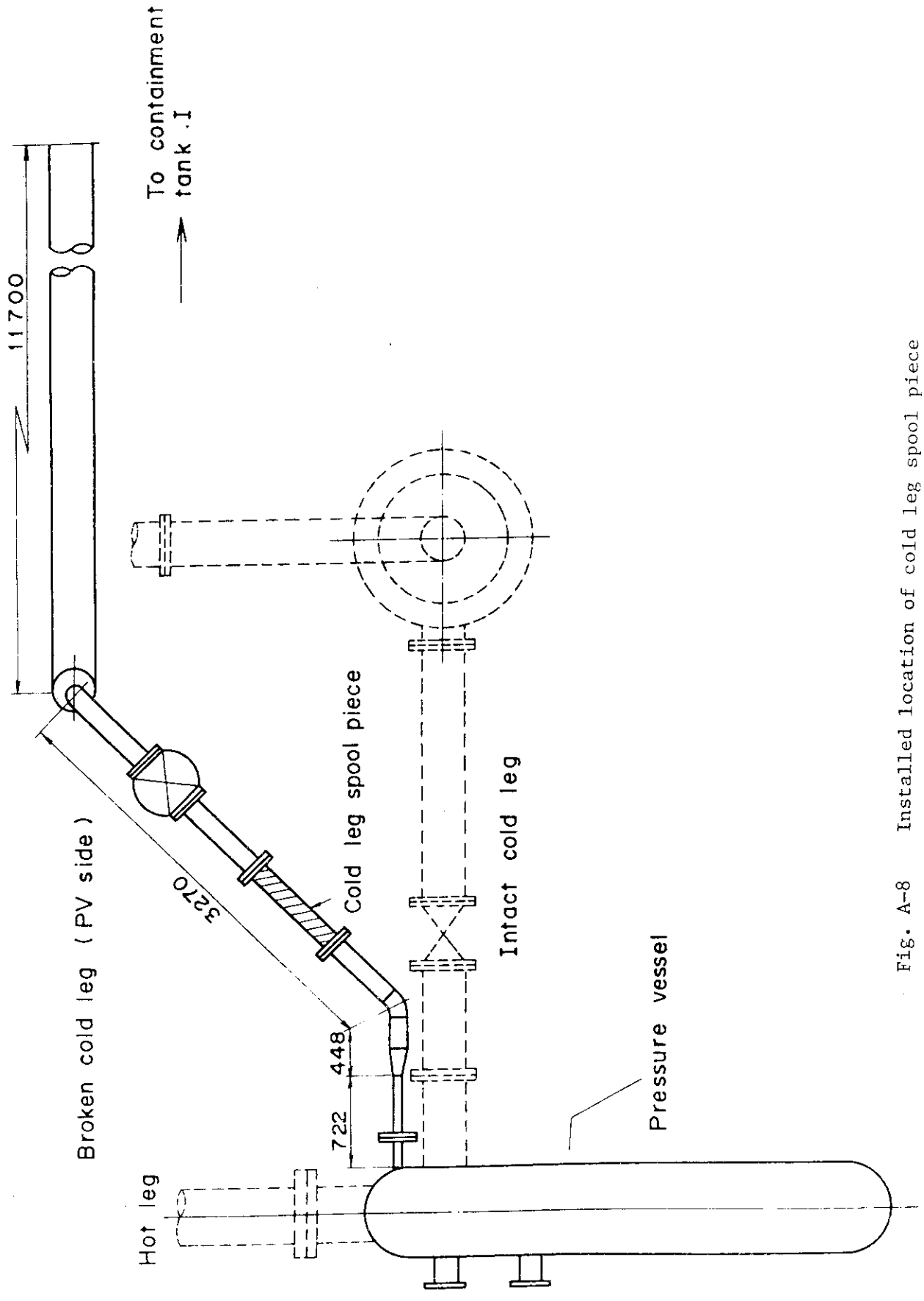

Fig. A-8 Installed location of cold leg spool piece

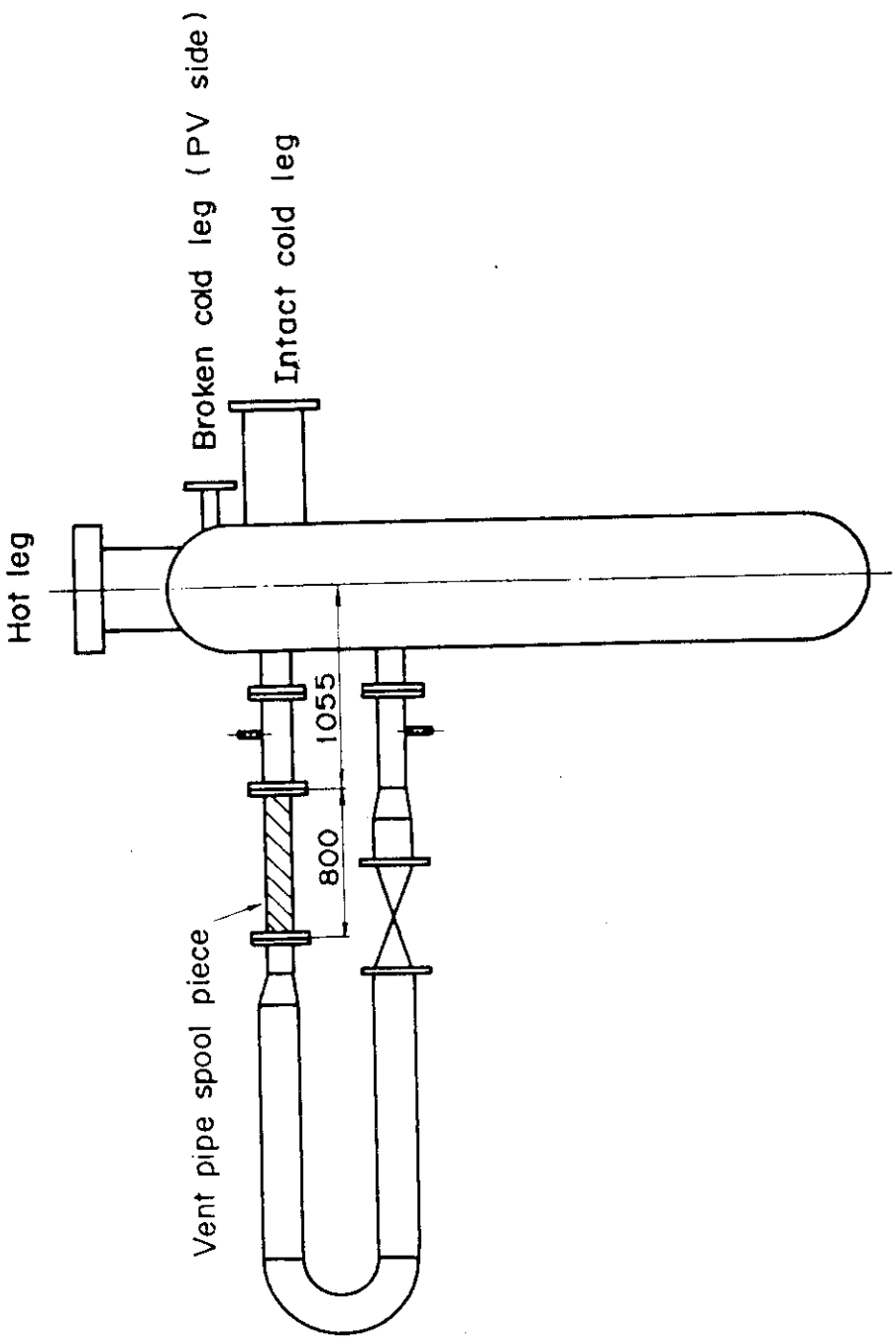

Fig. A-9 Installed location of vent pipe spool piece

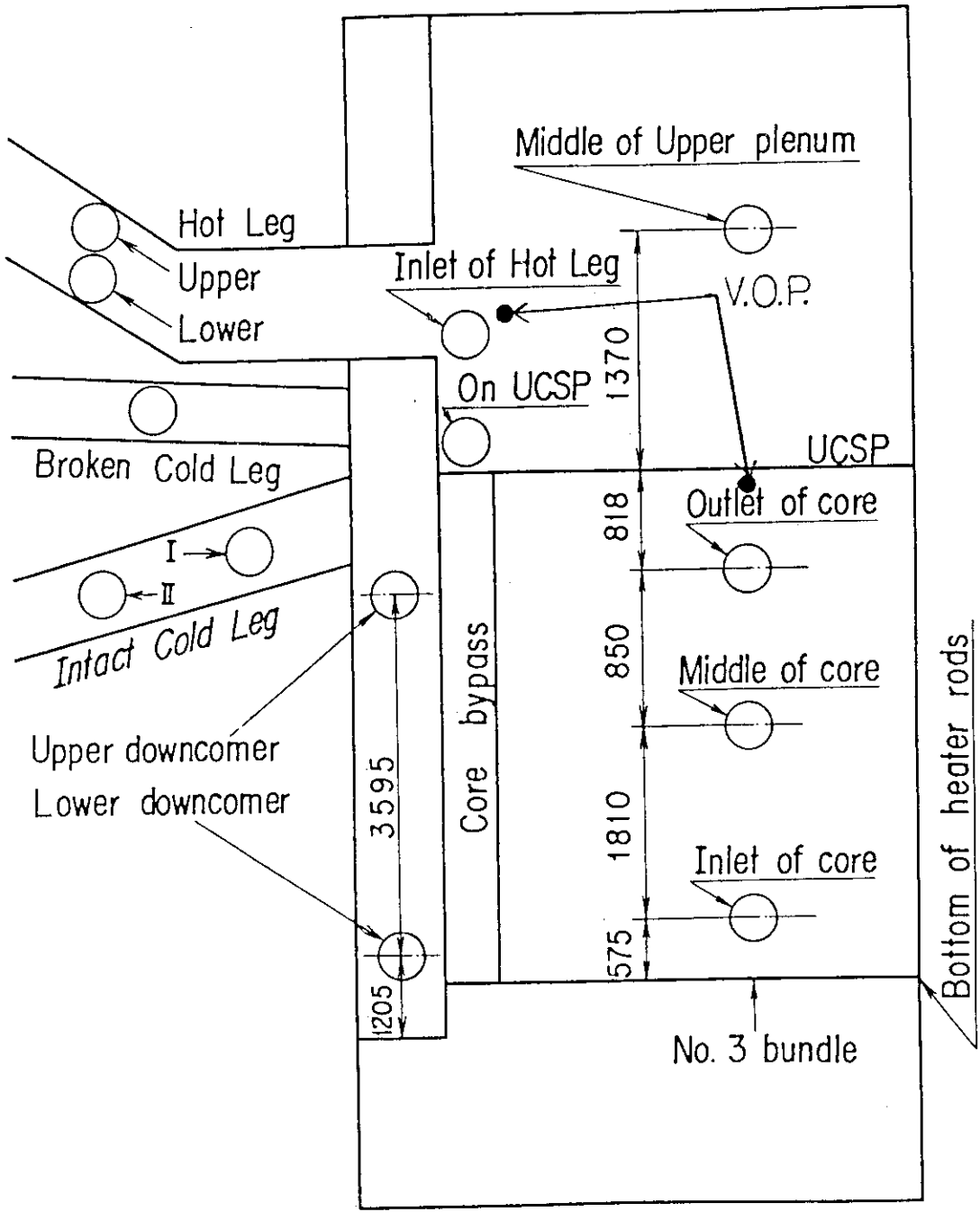

Fig. A-10 Locations of view windows and Video Optical Probes

Appendix B Computed Algorithm for INEL-Manufactured Instruments

The computed algorithm for the INEL instruments is explained in reference (5) in detail. The main part of the algorithm is presented here for the convenience of the data interpretation.

B.1 Single-Beam γ-Densitometer

The equations for converting measured count rate to average fluid density are:

$$I_i = C_i - C_{io}$$

where

I_i = Uncorrected count with background removed
C_i = Raw digital count
C_{io} = Raw digital count with source removed (calibration constant, may be zero or insignificant)
i = Beam number

$$I_i' = I_i (1 + \gamma_i I_i)$$

where

I_i' = Dead-time corrected count
I_i = Uncorrected count
γ_i = Dead-time constant (1.0×10^{-7}) (1/counts)
i = Beam number

$$\rho_i = A - B \ln I_i'$$

$$A = \rho_a + B \ln I_a' \quad \text{(Calibration constant) } (kg/m^3)$$

$$B = \frac{(\rho_w - \rho_a)}{\ln \frac{I_a'}{I_w'}} \quad \text{(Calibration constant) } (kg/m^3)$$

where

ρ_i = Average chrodal fluid density (kg/m^3)
I_i' = Dead time corrected count of fluid
I_w' = Dead-time corrected count in water (calibration constant)

I'_a = Dead-time corrected count in air (calibration constant)

ρ_w = Density of water at time of calibration (calibration constant) (kg/m^3)

ρ_a = Density of steam at time of calibration (kg/m^3)

i = Beam number

B is hand-calculated only at installation time, and A is calculated prior to each test.

B.2 Hot Leg Spool Piece

A flow chart for the hot leg spool piece calculations is shown in Fig. B-1. The general procedure is to calculate the required outputs for the four regions separately, using the instrument data corresponding to each region. Absolute pressure is assumed uniform over the pipe cross section. The calculated parameters from the four regions are then combined to produce an additional set of average parameters for the total cross section of the spool piece.

For each region, the general procedure is first to determine steam and water densities from temperature and pressure measurements, or from estimates if temperature and/or pressure readings are unreasonable. Two-phase fluid density is then determined from densitometer readings. Then void fraction, average fluid velocity, and average fluid mass flow rate are calculated.

For all of the foregoing calculations, unity-slip condition is assumed within each region, and unity-slip versions of two-phase flow equations are used, since the hot leg spool piece does not contain turbine flow meters.

Flow chart boxes in Fig. B-1 are described as follows:

Box 1: The subroutine obtains engineering unit values.

Box 2: The absolute pressure value is checked. If it does not fall between 70 and 1500 kPa, then it is an unreasonable value and is rejected.

Box 3: The temperature value is checked. If it does not fall between 5 and 300°C, then it is an unreasonable value and is rejected.

Box 4: If both pressure and temperature readings are out of range then water density is set to 1000 kg/m^3 and steam density is set to 1.0 kg/m^3.

Box 5: If the temperature reading is reasonable but the pressure reading is out of range, then the fluid is assumed saturated, and water density is calculated from temperature. The saturated pressure is determined, and steam density is calculated from the temperature reading and saturated pressure.

Box 6: If the pressure reading is reasonable but the temperature reading is out of range, then the fluid is assumed saturated. Saturated temperature is determined from the pressure reading, and steam and water densities are calculated from the measured pressure and saturated temperature.

Box 7: If both temperature and pressure readings are within limits, a determination is made of whether the fluid in the region is subcooled water, superheated steam, or saturated fluid. This is accomplished by obtaining the maximum and minimum saturation temperatures based on absolute pressure increased and decreased by the expected error of the pressure probe. The maximum and minimum saturation temperatures are then compared to the measured fluid temperature. If the maximum temperature is greater than the fluid temperature by an amount equal to a specified percent or reading error of the fluid temperature probe, then the calculations proceed to Box 8 and the flow is considered subcooled water. Conversely, if the minimum temperature is less than the fluid temperature minus the expected fluid temperature probe error, then the fluid is deemed superheated steam and calculations proceed to Box 10. If the fluid pressure and temperature are close to saturation values, such that the fluid is not deemed superheated steam or subcooled water, it is assumed to be saturated two-phase fluid and calculations proceed to Box 9.

Box 8: Water density is calculated from measured temperature. Even though the fluid is assumed subcooled, there may be steam present. In this case, it is assumed saturated. Saturated temperature is determined from measured pressure, and steam density is calculated from measured pressure and saturated temperature.

Box 9: Water density is calculated from measured temperature. Steam density is calculated from measured temperature and measured pressure.

Box 10: Steam density is calculated from measured temperature and measured pressure. Even though the fluid is assumed superheated,

there may be water present. In this case, it is assumed saturated. Saturated temperature is determined from measured pressure, and water density is calculated from saturated temperature.

Box 11: The density obtained by the γ-densitometer is compared with steam and water densities obtained in the preceding boxes.

Box 12: If the densitometer value is higher than the calculated water density, then the reading is assumed unreasonable and fluid density is set equal to water density.

Box 13: If the densitometer value falls between water and steam densities, then fluid density is set equal to the densitometer reading value.

Box 14: If the densitometer value is lower than the steam density, then the densitometer reading is assumed unreasonable and fluid density is set equal to steam density.

Box 15: Void Fraction, fluid velocity, and mass flow rate are calculated. The equation for calculating void fraction is:

$$\alpha = \frac{\rho_w - \rho_f}{\rho_w - \rho_s}$$

where

α = Void fraction

ρ_s = Steam density (kg/m^3)

ρ_f = Fluid density (kg/m^3)

ρ_w = Water density (kg/m^3)

The equation for calculating average fluid velocity is:

$$v_f = \left(\frac{I}{\rho_f} \right)^{1/2}$$

where

v_f = Average fluid velocity (m/s)

ρ_f = Fluid density (kg/m^3)

I = KF (kg/ms^2), the drag transducer engineering unit value, multiplied by the calibration constant, K. This constant has differnet values for forward and reverse flow.

The above equation for calculating fluid velocity assumes unity slip.

The equation for calculating mass flow is:

$$M_f = A_i \rho_f v_f$$

where

M_f = Fluid mass flow (kg/s)
A_i = Cross-sectional areas of spool piece regions (constants) (m^2)
ρ_f = Fluid density (kg/m^3)
v_f = Fluid velocity (m/s)

Box 16: This box implements execution of the loop once for each of the four regions of the spool piece.

Box 17: In this box, the parameters calculated for each of the four regions of the spool piece are combined to give corresponding averages for the whole cross section of spool piece. All equations (except for velocity and mass flow) can be represented generically as:

$$P_T^* = 0.31\ P_1^* + 0.27\ P_2^* + 0.26\ P_3^* + 0.16\ P_4^*$$

where

P_T^* = Total spool piece averaged parameter
P_1^* = Region 1 parameter
P_2^* = Region 2 parameter
P_3^* = Region 3 parameter
P_4^* = Region 4 parameter

For the total mass flow parameter, the four regional mass flows are added. For the total velocity, the following equation is used:

$$v_f = \frac{M_f}{A\rho_f}$$

where

v_f = Average total fluid velocity (m/s)
M_f = Average total mass flow rate (kg/s)
A = Cross section area of spool piece (constant, 0.082604 m^2)
ρ_f = Average total fluid density (kg/m^3)

B.3 Cold Leg Spool Piece

(1) Three-beam γ-densitometer

The equations for converting measured count rates to average fluid density for each beam are:

$$I_i = C_i - C_{io}$$

where

I_i = Uncorrected count background removed
C_i = Raw digital count
C_{io} = Raw digital count with sources removed (calibration constant, may be zero or insignificant)
i = Beam identification (A, G, or C)

$$I_i' = I_i \left[1 + \gamma \left(I_A + I_C + 1.5\, I_G\right)\right]$$

where

I_i' = Dead-time corrected count
I_i = Uncorrected count
γ = Dead-time constant (1.666666×10^{-6}/count)
i = Beam identification (A, G, or C)

$$I_G^0 = I_G' - a\, I_A' + b\, (I_A')^2$$

$$I_A^0 = I_A' - e\, I_G^0 + f\, (I_G^0)^2$$

$$I_G'' = I_G' - a\, I_A^0 + b\, (I_A^0)^2$$

$$I_A'' = I_A' - e\, I_G'' + f\, (I_G'')^2$$

$$I_C'' = I_C' - c\, I_A'' - d\, (I_G'')$$

where

I_G^0 = Count estimate for Gd^{153} beam
I_A^0 = Count estimate for Am^{241} beam
I_A' = Dead-time corrected count for Am^{241} beam

I'_G = Dead-time corrected count for Gd^{153} beam

I'_C = Dead-time corrected count for Cd^{109} beam

I''_G = Cross-talk and dead-time corrected count for Gd^{153} beam

I''_A = Cross-talk and dead-time corrected count for Am^{241} beam

I''_C = Cross-talk and dead-time corrected count for Cd^{109} beam

a, b, c, d, e, f = Cross-talk coefficients (calibration constants)

These coefficients are determined only at installation time.

Densities are determined with the following equation:

$$\rho_i = A - B \ln I''_i$$

$$A = \rho_a + B \ln I''_a \quad \text{(calibration constant)}$$

$$B = \frac{(\rho_w - \rho_a)}{\ln \frac{I''_a}{I''_w}} \quad \text{(calibration constant)}$$

where

ρ_i = Average chordal fluid density (kg/m^3)

I''_i = Corrected count

I''_w = Corrected count in water (calibration constant)

I''_a = Corrected count in air (calibration constant)

ρ_w = Density of water at time of calibration (calibration constant) (kg/m^3)

ρ_a = Density of steam at time of calibration (kg/m^3). In the SCTF, the dry calibration is carried out in pre-heating period just before the test. Therefore, the system is filled with steam.

i = Beam identification (A, G, or C)

B is calculated only at installation time, and A is calculated prior to each test.

(2) Two-Phase Flow Calculation

A flow chart for the cold leg spool piece calculations is given in Fig. B-2. The general procedure is first to determine steam and water

densities from temperature and pressure measurements, or from estimates if temperature and/or pressure readings are unreasonable. Two-phase fluid density is determined from densitometer readings. Then steam velocity and mass flow rate, water velocity and mass flow rate, void fraction, fluid velocity, and fluid mass flow rate are calculated. Flow chart box descriptions in Fig. B-2 are as follows:

Boxes 1~10: Operations in these boxes are identical with those already described for boxes 1 through 10 of the hot leg spool piece.

Box 11: The average fluid density for two-phase flow is calculated from densitometer readings and individual phase densities.

Box 12: A test is made to see that average fluid density measured by the densitometer is between steam and water densities.

Box 13: If fluid density is below steam density in box 12, then fluid density is set equal to steam density. If fluid density is above water density, then fluid density is set equal to water density. Fluid velocity is set equal to turbine velocity.

Box 14: Average fluid density is calculated using turbine meter and drag-screen engineering unit values. The equation is:

$$\rho_{ft} = \frac{I}{v_t^2}$$

where

ρ_{ft} = Average fluid density from turbine and drag screen (kg/m^3)

I = Momentum flux = $K\ (F_1 + F_2 + F_3)$ (kg/ms^2), sum of the three drag transducer engineering unit values, multiplied by the calibration constant K. This constant has different values for forward and reversed flow.

v_t = Turbine meter velocity (m/s)

A test is then made to see that the calculated value of ρ_{ft} is greater than steam density.

Box 15: Fluid velocity is set equal to turbine velocity. A flag is set to indicate a unity-slip condition and rejection of drag screen data.

Box 16: A test is made to see that the calculated value of ρ_{ft} is less than fluid density.

Box 17: Unity-slip velocity calculations are made using drag screen and densitometer engineering unit values. A flag is set to indicate the unity slip assumption, and rejection of turbinemeter data. Steam and water velocities are calculated from:

$$v_{us} = \left(\frac{I}{\rho_f} \right)^{1/2}$$

where

v_{us} = Unity slip velocity (m/s)
I = Value of momentum flux calculated in box 14 (kg/ms^2)
ρ_f = Fluid density from densitometer (kg/m^3)

Box 18: Void fraction is calculated from the equation given in box 19. Steam and water mass flows are calculated from:

$$M_s = \alpha A \rho_s v_{us}$$

$$M_w = (1 - \alpha) A \rho_w v_{us}$$

where

M_s = Mass flow rate of steam (kg/s)
M_w = Mass flow rate of water (kg/s)
A = Cross-sectional area of spool piece (constant) (m^2)
ρ_s = Steam density (kg/m^3)
ρ_w = Water density (kg/m^3)
v_{us} = Unity-slip fluid velocity (m/s)
α = Void fraction (as calculated in box 19)

Fluid mass flow rate is calculated by summing steam and water mass flow rates.

Box 19: General two-phase calculations are made using drag screen, turbine meter, and densitometer engineering unit values. The equation for calculating void fraction is:

$$\alpha = \frac{\rho_w - \rho_f}{\rho_w - \rho_s}$$

where

α = Void fraction
ρ_w = Water density (kg/m^3)

ρ_s = Steam density (kg/m^3)
ρ_f = Fluid density (kg/m^3)

The equations for calculating steam and water velocities are derived from the following assumptions.

i) The momentum flux measured by the drag screen is equal to the sum of the momentum fluxes of each phase weighted proportionately by void fraction, or

$$I = \alpha\rho_s v_s + (1 - \alpha)\ \rho_w v_w \quad .$$

ii) Equating measured turbine velocity to the Rouhani model for turbine meter velocity gives

$$V_t = \frac{\alpha\rho_s v_s^2 + (1 - \alpha)\ \rho_w v_w^2}{\alpha\rho_s v_s + (1 - \alpha)\ \rho_w v_w} \quad .$$

Equations (i) and (ii) are now solved simultaneously for v_s and v_w. The method of the derivation is detailed in Appendix A of reference (5).

The derived equations are:

$$v_s = v_f + \eta^{-1/2}\ \Delta v$$

$$v_w = v_f - \eta^{1/2}\ \Delta v$$

where

$$v_f = \frac{I}{\rho_f v_t}$$

$$\eta = \frac{\alpha\rho_s}{(1 - \alpha)\ \rho_w}$$

$$\Delta v = (v_f v_t - v_f^2)^{1/2}$$

v_s = Steam velocity (m/s)
v_w = Water velocity (m/s)
v_f = Average fluid velocity (m/s)

I = Drag screen momentum flux (kg/ms^2) (as calculated in box 14)
v_t = Turbine meter velocity (m/s)
ρ_f = Fluid density (kg/m^3)
ρ_s = Steam density (kg/m^3)
ρ_w = Water density (kg/m^3).

The equations for calculating steam and water mass flow rates are:

$$M_s = A \alpha \rho_s v_s$$

$$M_w = A (1 - \alpha) \rho_w v_w$$

where

M_s and M_w = Mass flow rates (kg/s) for steam and water
A = Spool-piece cross-sectional area (constant) (m^2)
α = Void fraction
ρ_s and ρ_w = Densities (kg/m^3) for steam and water
v_s and v_w = Velocities (m/s) for steam and water.

Fluid velocity is calculated using the above equation for v_f, and fluid mass flow rate is obtained by summing steam and water mass flow rates.

Box 20: If water mass flow rate exceeds a specified upper limit (supplied constant), calculations in box 19 are rejected and redone in box 17 and 18.

B.4 Downcomer Drag Disk

B.4.1 Single-Phase Water Velocity

Local single-phase water velocity can be calculated from downcomer drag disk force and temperature readings.

The equation for determining water velocity is:

$$v_w = \left[\frac{I}{\rho_w} \right]^{1/2}$$

where

v_w = Local water velocity

$I = K(F-F_b)$, where K is a conversion constant and F is the drag disk force

$F_b = K_b \rho_w$, where K_b is a buoyance-correction constant.

ρ_w = Water density obtained by the temperature reading supplied by the thermocouple.

B.4.2 Mass Flux

The mass flux at each of the three measurement locations in the downcomer can be calculated by combining the velocities from the drag disks and the void fractions from the corresponding string probes. This algorithm has been developed by ORNL.

(1) Upper Location (between Intact and Broken Cold Legs)

(a) If $\alpha > 0.995$, Steam single-phase flow

$$G = C_g \rho_g \left(\frac{\rho_w}{\rho_g}\right)^{0.528} V_w^{1.056}$$

(b) If $0.92 < \alpha < 0.995$, Mist flow

$$G = C_m \rho_f^{0.567} \rho_m^{0.567} V_w^{1.134}$$

The mist to froth transition point, MF, is calculated by

$$MF = [\rho_m \rho_f V_w^2]^{0.5}$$

(c) If $\alpha > 0.85$ and $MF < 100.0$, Mist flow

The same equation as (b)

(d) IF $\alpha > 0.2$ and $MF > 300.0$, Froth flow

$$G = C_{fr} \rho_f^{1.645} \rho_m^{1.645} V_w^{3.29}$$

(e) IF none of the above, Liquid single-phase flow

$$G = C_f \rho_f V_w^{1.02}$$

(2) Lower Locations (near the Bottom of Downcomer)

(a) If $\alpha < 0.3$, Liquid single-phase flow

$$G = C_f \rho_f V_w^{1.02}$$

(b) If $\alpha > 0.3$ and $V_w < 0.9$ of full scale

$$G = 0.0$$

(c) If $\alpha > 0.3$ and $V_w > 0.9$ of full scale

The drag disk is probably sensing falling water and no flow determination is possible.

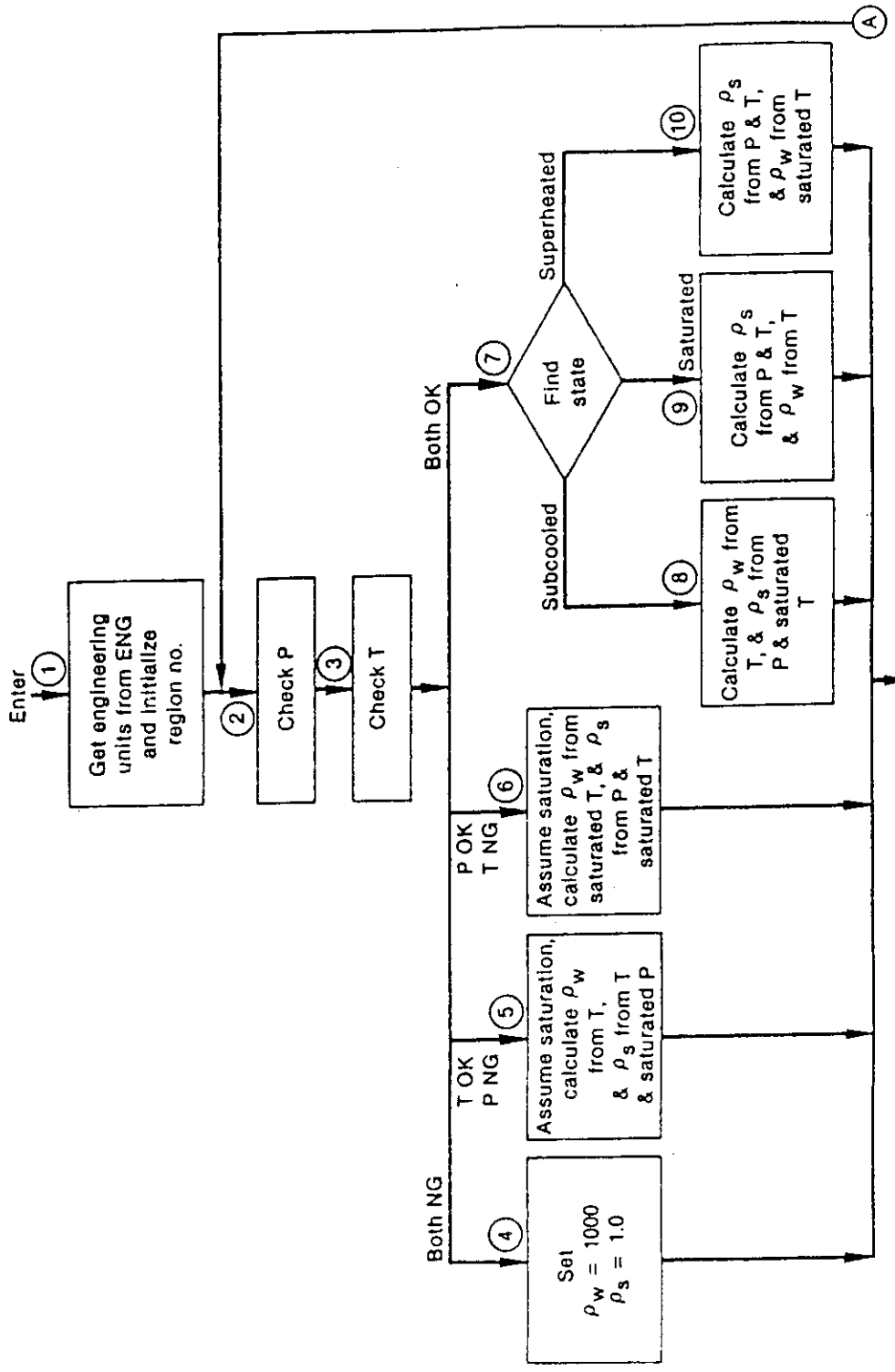

Fig. B-1 Calculation flow chart for hot leg spool piece

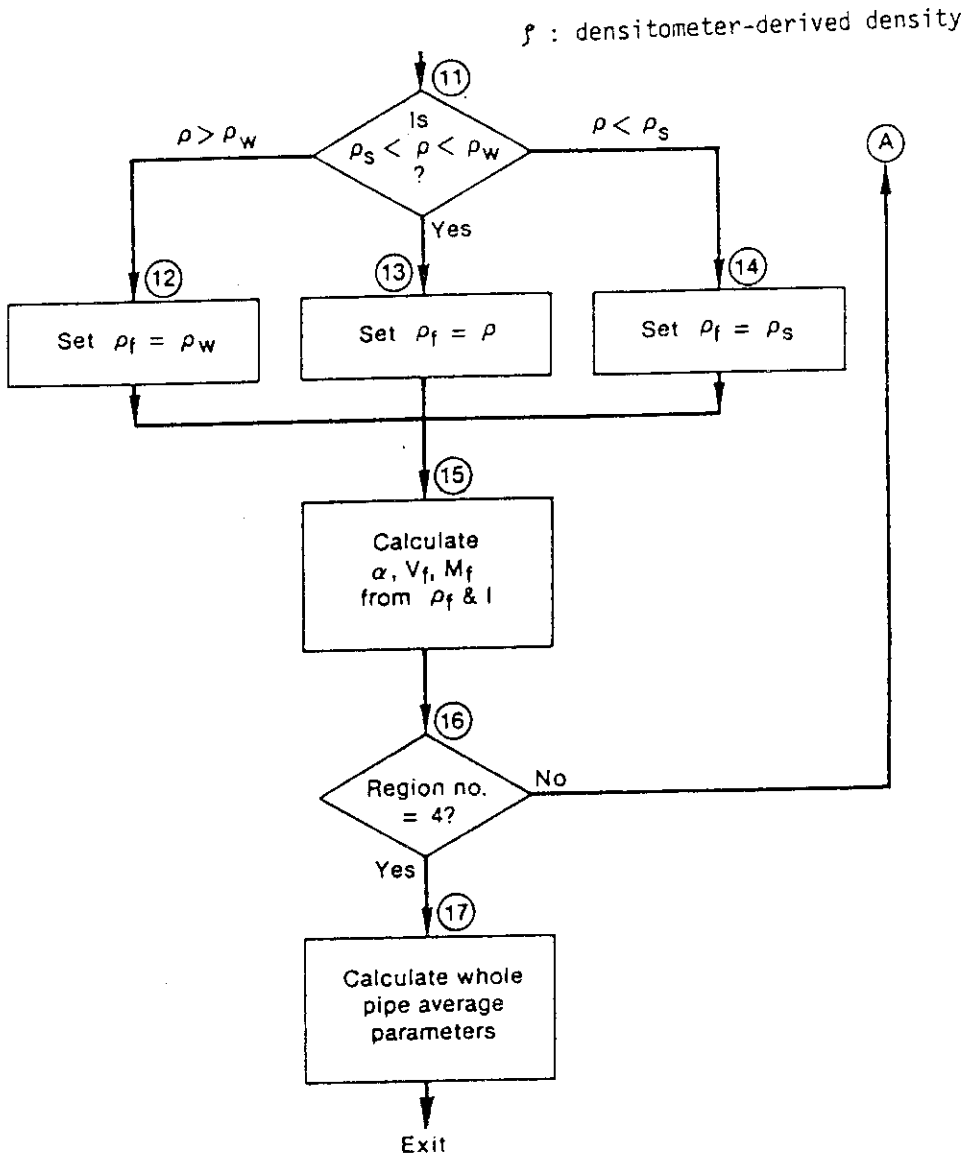

Fig. B-1 (continue)

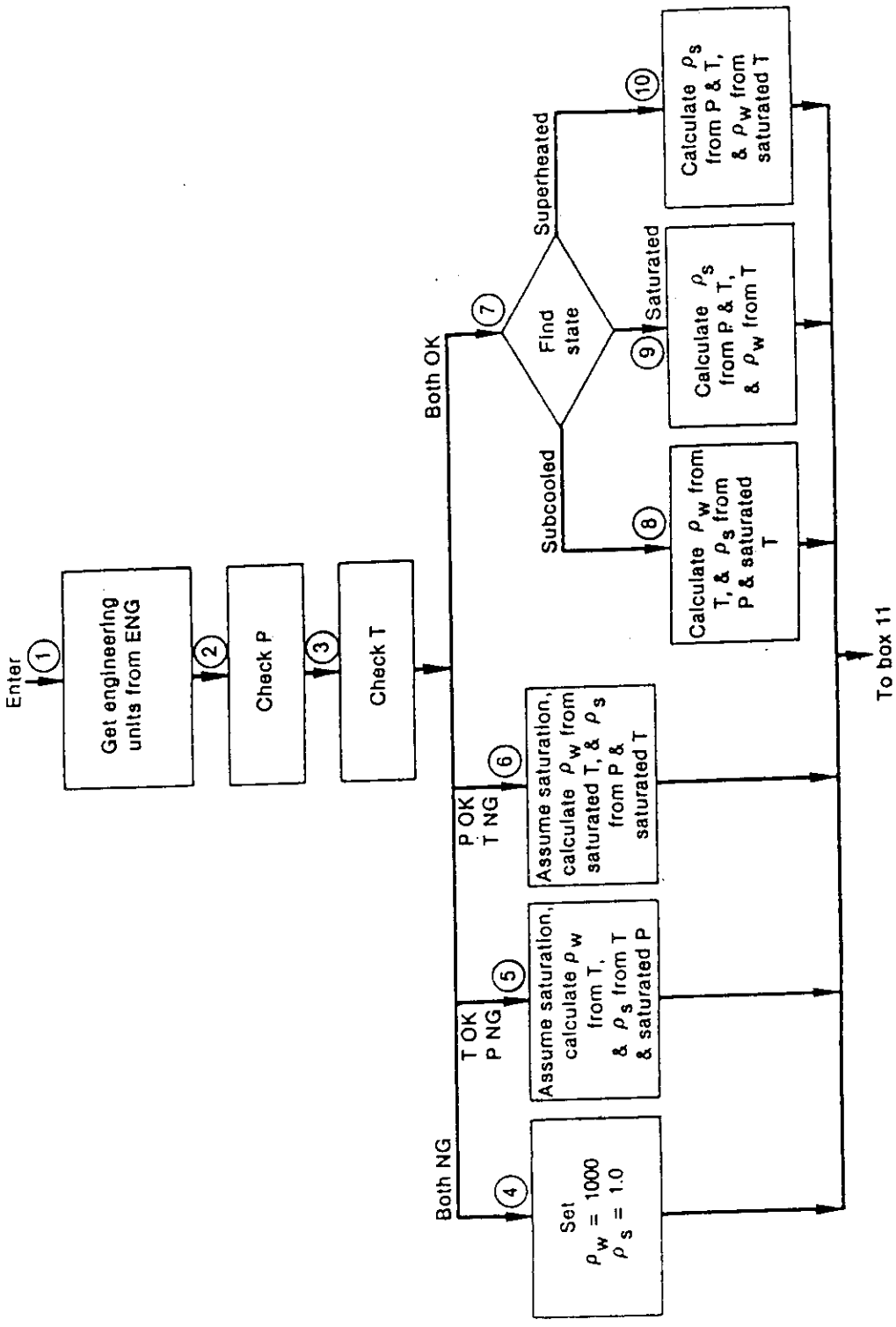

Fig. B-2 Calculation flow chart for cold leg spool piece

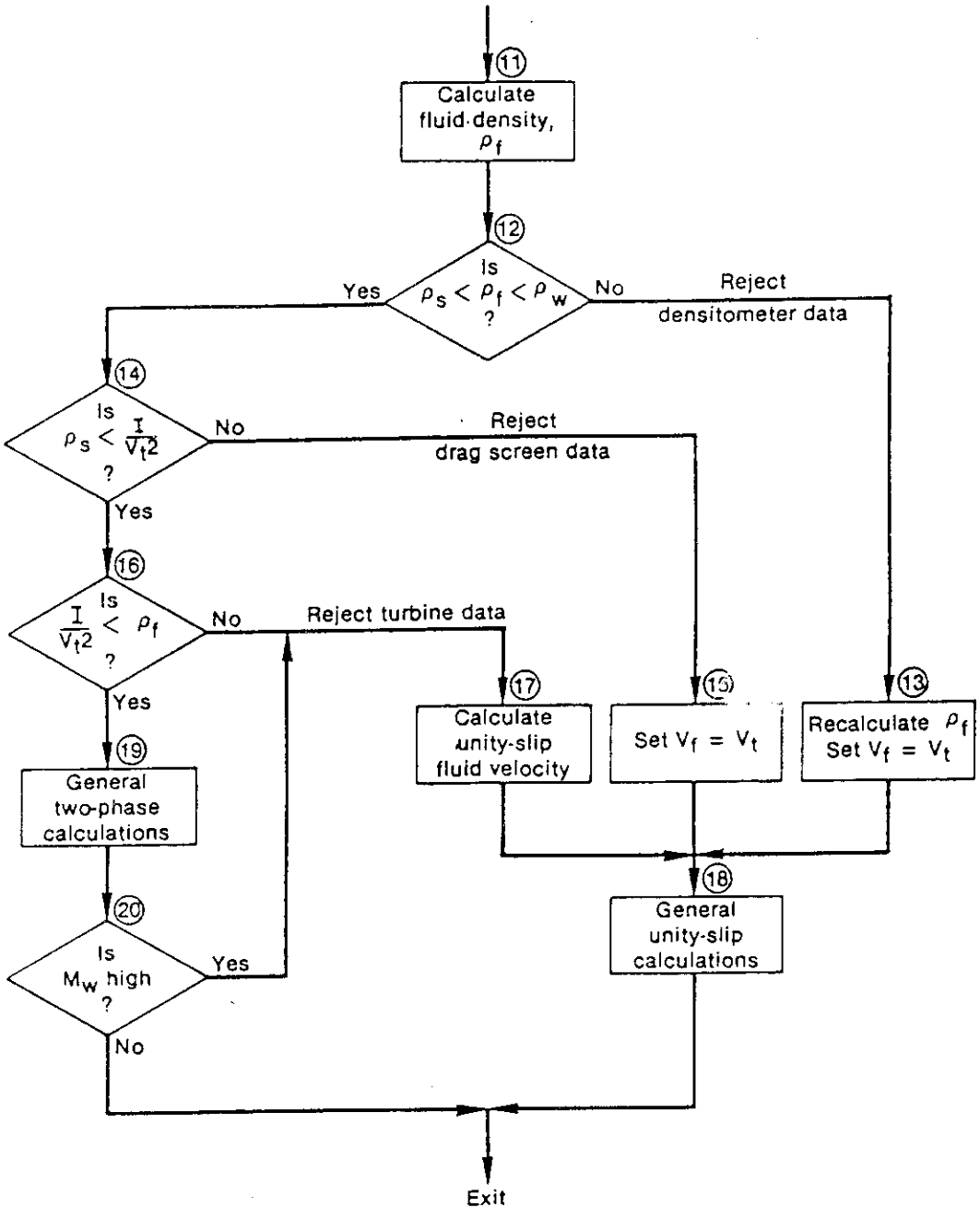

Fig. B－2 (continue)

Appendix C Computed Algorithm for ORNL-Manufactured Instruments

The computed algorithm for the ORNL instruments is explained in reference (6) in detail. The outline of the algorithm is preseted here for the convenience of the data interpretation.

C.1 Impedance Probes (Flag, Prong and String Probes)

The principle of operation of the impedance probe is based on measurement of the electrical impedance of the fluid mixture in the vicinity of an electrode pair, as shown in Fig. C-1.

(1) Void Fraction

The void fraction at the impedance probe is related to the-average impedance of the two-phase mixture.

The capacitance between parallel plates is written as

$$C = k\varepsilon \frac{A}{\ell} \quad ,$$

where A = Area of one of the plates

ℓ = Spacing between the plates

ε = Permittivity

k = Dielectric constant.

Since the two-phase mixture flowing between the two electrodes serves as the dielectric constant, the capacitance will vary with changes in the composition of this mixture, having a maximum value with water as the dielectric and a minimum with steam alone.

The liquid dielectric constant (ε_w) is a function of only liquid temperature. The vapor dielectric constant (ε_s) is approximated to be unity. The dielectric constant of two-phase mixture (ε_m) can be calculated from the measured impedance magnitude and impedance phase angle.

Then, a relative capacitance void fraction (α_c) is obtained as

$$\alpha_c = \frac{\varepsilon_w - \varepsilon_m}{\varepsilon_w - \varepsilon_s}$$

However, the capacitance variation with void fraction is different for different flow patterns as shown in Fig. C-2. If the two-phase mixture is in the dispersed flow pattern, the true void fraction is far below

the relative capacitance void fraction. Therefore, it is needed to identify and compensate for the dispersed flow regime effects on the void fraction.

The final equation of the corrected void fraction (α) is written as

$$\alpha = 1 - (1 - \alpha_c) \left[\frac{\varepsilon_w + m\varepsilon_s}{\varepsilon_w(1 - \alpha_c) + \varepsilon_s(m + \alpha_c)} \right]$$

where m is a fluid distribution factor and defined as

$$m = \frac{A(1 - \alpha_c)^{0.3}}{s} + 1$$

where A = Probe calibration constant

S = $100\ [1 - \tan\gamma/\tan\gamma_{max}]$

γ = Measured fluid loss angle

γ_{max} = Calculated maximum loss angle with no dispersed droplet

(2) Velocity

The velocities of the two-phase fluid are determined from the average transport time of the two signals detected by the two adjacent sensors of a flag probe. Fig. C-3 illustrates the concept of this method.

The calculation of average transport time, $\bar{\tau}$, is based on the assumption that the process can be approximated by a simple transport delay model. According to this model, the phase shift of the transfer function of signals from two adjacent sensors is characterized as a linear function of frequency in which the slope of the phase function can be shown to be equivalent to the transport delay of the model. The average transport time is calculated by first estimating a one-second, average phase-shift between the two sampled probe signals and then fitting this phase shift to a linear first-order approximation model using a linear-least-squared-error fitting technique. Fig. C-4 shows the example of average phase shift between two magnitude signals. Average transport time, $\bar{\tau}$, is estimated from the slope of the fitted line as

$$\bar{\tau} = -\frac{d\theta}{df}$$

where θ = Phase of cross power spectral density function of two signals

f = Frequency

The above method is called the cross-power-spectral density (CPSD) method.

The average velocity of the two-phase fluid during a certain time interval is calculated by

$$\bar{v} = \frac{S}{\bar{\tau}}$$

where S is the axial spacing between the sensors.

C.2 Film Probe

(1) Liquid film thickness

The principle of operation of the film probe is based on the measurement of the electrical admittance of the fluid in the vicinity of a set of electrodes. The equation for admittance is:

$$Y = \frac{1}{R} + i\ \omega\ C$$

where Y = Admittance
R = Resistance
ω = Anglar frequency
C = Capacitance

In the expression for the admittance of the liquid film, R and C is expressed by:

$$R = \frac{1}{f(\delta)\sigma} \quad \text{and} \quad C = f(\delta)\varepsilon_0\varepsilon \quad ,$$

where δ = Film thickness
σ = Liquid conductivity
ε = Dielectric constant
ε_0 = permittivity of empty space

If the conductance of wall (G_0) and the capacitance contribution from the wall and wires (C_0) are considered, the admittance can be written as;

$$Y = f(\delta)\ (\sigma + i\ \omega\ \varepsilon_0\ \varepsilon) + G_0 + i\ \omega\ C_0 \qquad (C\text{-}1)$$

where: ε_0 is a physical constant (= 8.854×10^{-12} Farad/meter)

ω is determined by the design of the instrument

G_0 and C_0 are determined by calibrating the instrument before each test. This calibration is done by measuring the impedance of the film probe when it is dry and when it is under water. G_0 and C_0 are calculated with the measured magnitudes and phase angles of the impedance.

σ is obtained with a reference conductivity probe in the lower plenum.

ε for water is calculated with an empirical formula by using the temperature measured near the film probe.

$f(\delta)$ is determined by calibrating the instrument before it is installed in the test facility. This is done by covering the film probe with a liquid film the thickness of which is measured with a different method.

Y is measured by the electronic components of the film probe.

Since all of the ε_0, ω, G_0, C_0, σ, ε, $f(\delta)$ and Y are known, the film thickness, δ, can be obtained by using equation (C-1).

(2) Film velocity

An average film velocity is calculated from two velocities; E.P. probe velocity and wave velocity.

(a) E.P. probe velocity

When electrodes are submerged in electrolytes, as water with dissolved salts, and an electric current flows through them, ions of different kinds become arranged in layers on and near the electrode surfaces. It is speculated that these layers are distorted by the shear stress, τ, in the flowing water. This distortion changes the impedance of the layers and also the electric current.

An empirical relation between the current, I_e, and the film velocity, v, is developed as

$$\frac{I_e}{\sigma} = A(\delta)e^{-B(\delta)v} \quad .$$

$A(\delta)$ and $B(\delta)$ are function of δ which have to be determined experimentally. If σ and δ are known, and the functions $A(\delta)$ and $B(\delta)$ have been determined, the velocity of the film, v, can be calculated as

$$v = \frac{\ln[\sigma A(\delta)/I_e]}{B(\delta)} \quad .$$

These probes are called Electrolysis Potential Probes, or E.P. probe. They are installed near Film Probes with which the needed film thickness, δ, is determined. The needed conductivity, σ, is obtained from the reference conductivity probe for the in-core and upper plenum structure film probes or from the attached conductivity probes for the wall film probes.

(b) Wave velocity

Since the E.P. Probe measures only the velocity of the liquid near the wall, it is necessary to measure also shape and velocity of the interfacial waves. The wave shape is measured with the film probes. The velocity of the waves can be determined with two film probes placed near each other, one vertically above the other on the vertical wall. By the use of the CPSD method, the wave velocity is computed from the time interval between the two signals and the distance between the probes. This is the same method of the measurement of droplet velocity explained in C.1.

(c) Average film velocity

The average film velocity is expressed as the combination of the E.P. probe velocity and wave velocity.

$$v_{film} = \left[\frac{\delta_1 - A_1}{\delta_1} \right] * v_{EP} + \frac{A_1 * v_{wave}}{\delta_1}$$

where v_{film} = Average film velocity (cm/sec)
δ_1 = Mean value of sensor 1 film thickness (cm)
v_{EP} = E.P. probe velocity (cm/sec)
v_{wave} = Wave velocity (cm/sec)
A_1 = Wave amplitude (cm)

C.3 Reference Conductivity Probe

The reference conductivity probe is one pair of electrodes like the wall film probe conductivity electrodes. Here the amount of water over

the probe is always so much that its effect is as if it were an infinitely thick film. As a consequence, the coefficient $f(\delta)$ has a known constant value

$$f_c = \text{constant} = f(\infty)$$

For the reference conductivity probe, equation (C-1) becomes

$$Y_c = [f(\infty)\sigma + G_0] + i\,\omega\,[f(\infty)\varepsilon_0\,\varepsilon + C_0]$$

The real part is written as

$$Y_{Rc} = |Y_c|\cos\theta = f(\infty)\sigma + G_0$$

From this equation, the liquid conductivity σ can be calculated as

$$\sigma = \frac{1}{f(\infty)}\,(|Y_c|\cos\theta - G_0)$$

All terms on the right hand side are know either from the measurements during the tests ($|Y_c|$ and θ), or from previous calibrations (G_0 and $f(\infty)$).

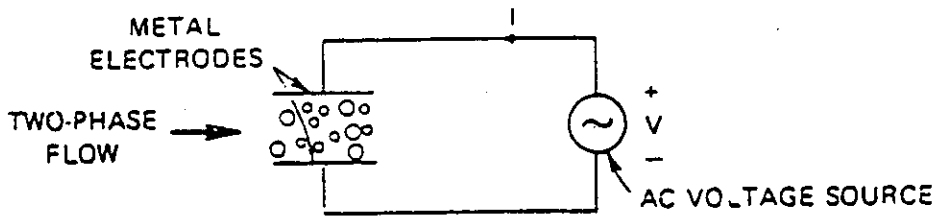

$$\text{IMPEDANCE, } Z = \frac{V}{I}$$

$$Z = R + \frac{1}{jwC}$$

$$R = f(\text{CONDUCTIVITY, GEOMETRY})$$

$$C = f(\text{PERMITTIVITY, GEOMETRY})$$

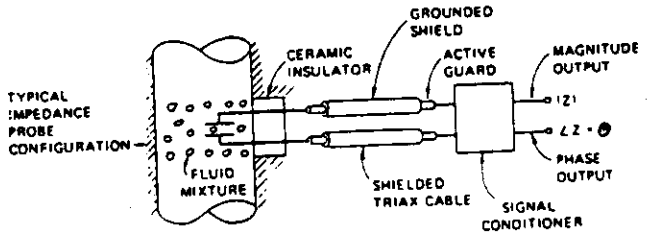

Fig. C-1 Diagram of impedance probe

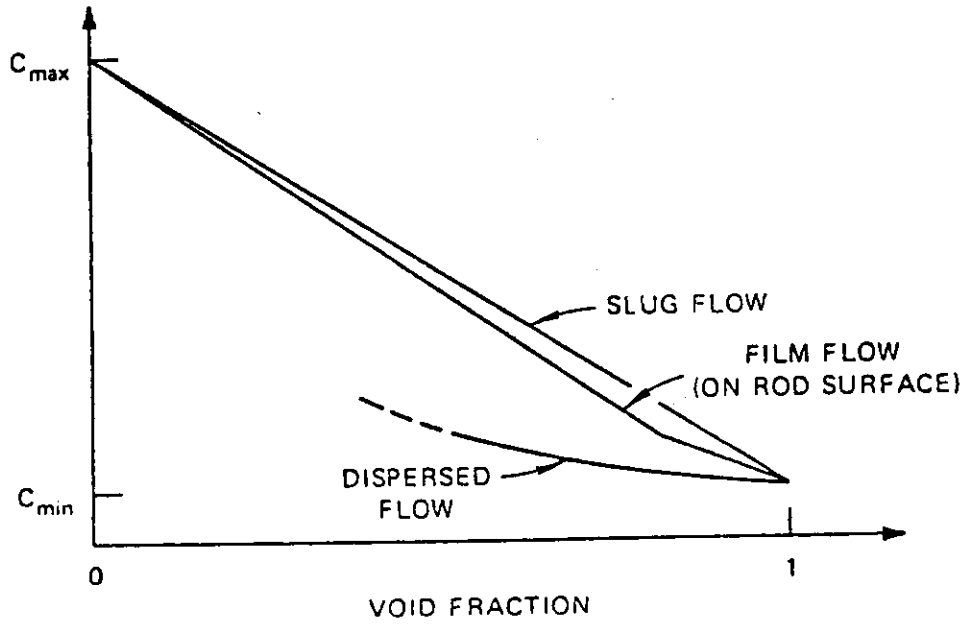

Fig. C-2 Relationship of impedance probe capacitance to void fraction for different flow patterns

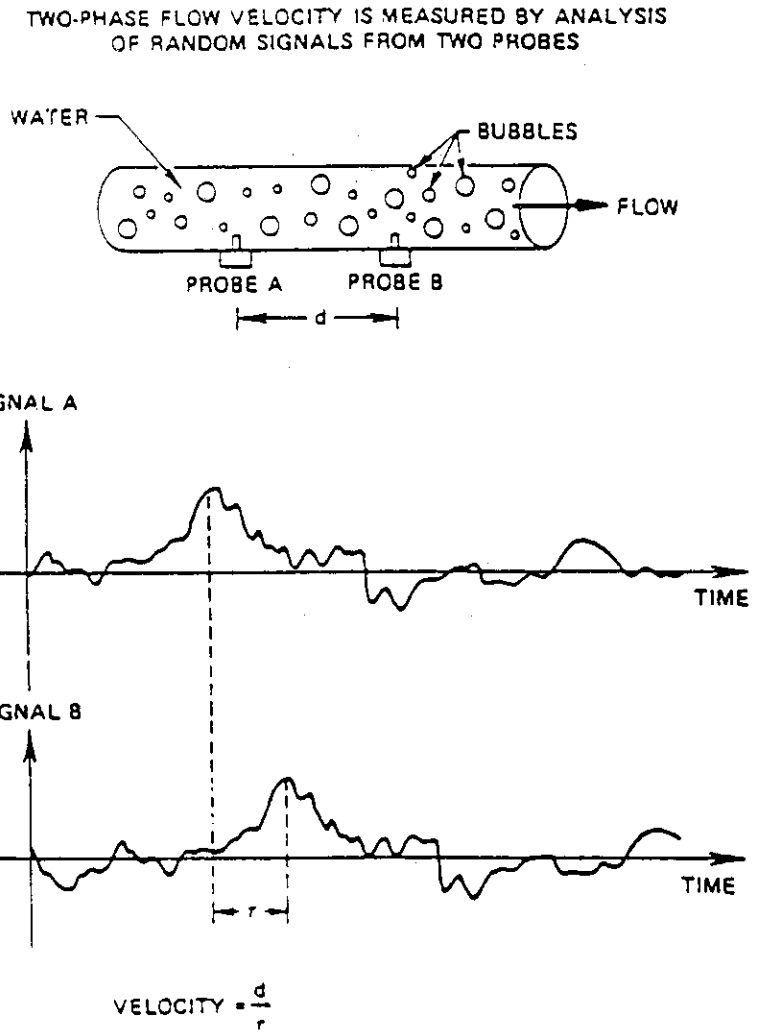

Fig. C-3 Concept of velocity measurement by flag probe

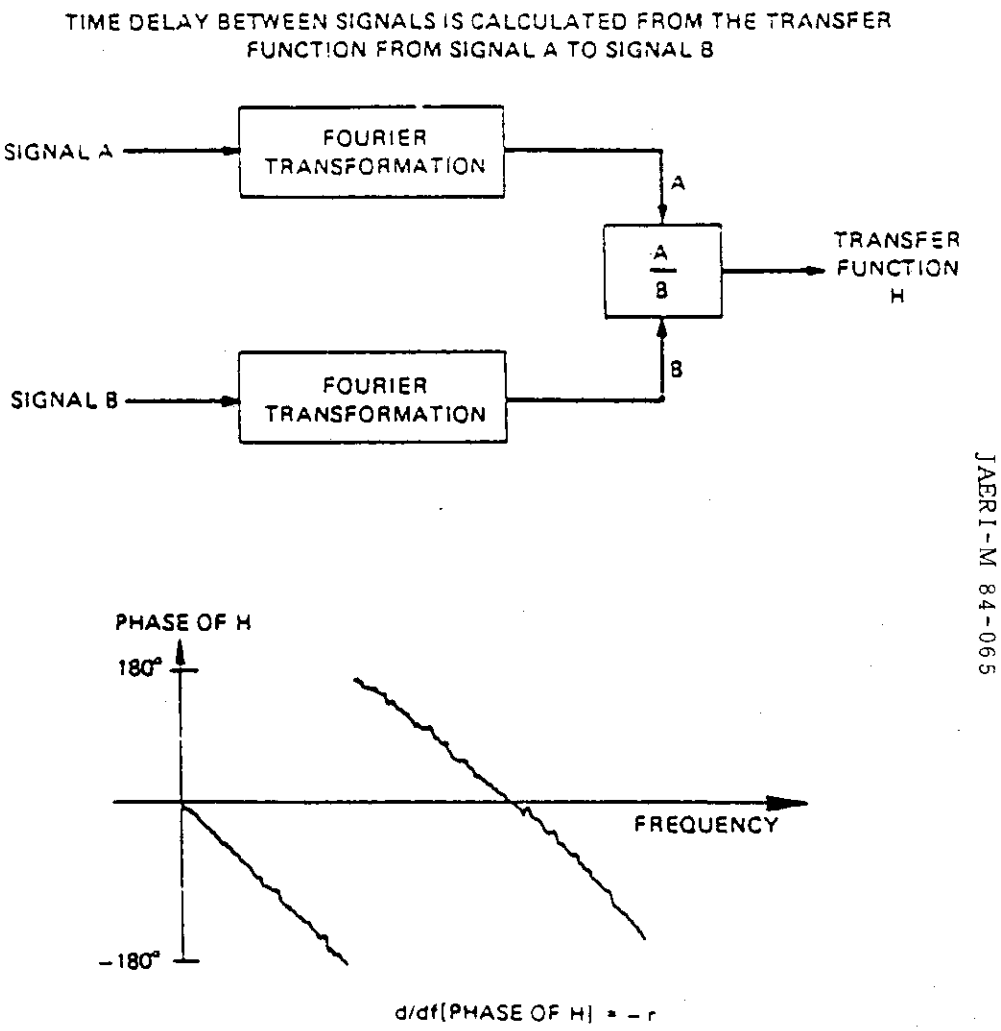

Fig. C-4 Phase shift of transfer function from two signals